THE EFFECTS OF ATMOSPHERIC REFRACTIVITY IN NEAR-EARTH UHF CHANNELS

A Dissertation
Presented to
The Academic Faculty

By

Rajib Bhattacharjea

In Partial Fulfillment
of the Requirements for the Degree
Doctor of Philosophy
in
Electrical and Computer Engineering

School of Electrical and Computer Engineering
Georgia Institute of Technology
December 2014

THE EFFECTS OF ATMOSPHERIC REFRACTIVITY IN NEAR-EARTH UHF CHANNELS

Approved by:

Professor Andrew F. Peterson
Professor, School of ECE
Georgia Institute of Technology

Professor Glenn S. Smith
Regents' Professor Emeritus, School of ECE
Georgia Institute of Technology

Professor Gregory D. Durgin, Advisor
Assoc. Professor, School of ECE
Georgia Institute of Technology

Professor Paul G. Steffes
Professor, School of ECE
Georgia Institute of Technology

Professor Christopher R. Anderson
Asst. Professor, Department of Electrical Engineering
United States Naval Academy

Date Approved: September 2014

For Amber, Forever Ago

ACKNOWLEDGMENTS

This research that this dissertation describes has been conducted with support from the Sciences Addressing Asymmetric Explosive Threats program of the United States Office of Naval Research. I must thank the program managers first and foremost for funding major portions of this work.

My advisor, Prof. Gregory D. Durgin, was instrumental in providing key feedback in the preparation of this document. One can easily become lost in minute details when performing research; Prof. Durgin was always there to remind me to place the research in a broader practical context. Prof. Chris R. Anderson also served as my supervisor for all of the field work conducted as part of this effort, and none of the present work would have been possible without his efforts and guidance.

Ever since I took advanced courses in electromagnetics under Prof. Andrew F. Peterson and Prof. Glenn S. Smith, I have greatly admired them as experts in the field of electromagnetics. On several occasions I have had textbooks they have respectively written recommended to me by others; each time, I have been proud to tell the person making the recommendation that I have studied under each of them. I am prouder still that they both have served on my defense committee. When in doubt about some particular detail of a computational EM technique or the theory of Maxwell's equations, they are the first people I have consulted, and both have generously answered my queries.

Prof. Paul Steffes has provided valuable comments and suggestions in the preparation of this document, and I cannot thank him enough. His wisdom about putting my work in the context of a future research program was very much appreciated.

The measurements presented in this document would not have been possible without the efforts of Robert Wert and Evan Worthington of the United States Naval Research Laboratory. I thank them for their diligent pursuit of accurate measurements, and for allowing me to analyze the data they collected.

I would like to thank the motley crew of people whom I have consulted to "bounce ideas off of". My progress was often slowed by thinking of problems in the same way, like being stuck in a rut. The informal discussions I have had with Blake Marshall, Dr. Ahzar Hassan, Dr. Matt Trotter, Bashir Akbar, Prof. Charles Nelson, Dr. Christopher Valenta, and especially Marcin Morys, have been invaluable to getting me "unstuck".

I would like to thank my parents, Sudhamoy and Anuradha Bhattacharjea for supporting me, and my sister, Lopa Bhattacharjea, for literally being her brother's keeper during the final stages of the doctoral process.

Finally, I have to thank Amber Robinson, for being my source of emotional support through the entire process. I would have lost my mind and given up the pursuit of a PhD years ago if not for her. I cannot thank her enough.

TABLE OF CONTENTS

ACKNOWLEDGMENTS iv

LIST OF TABLES viii

LIST OF FIGURES ix

LIST OF SYMBOLS xiii

SUMMARY xvii

CHAPTER 1 INTRODUCTION 1
1.1 Motivation 1
1.2 History of Radio Propagation Modeling 3
1.3 Unique Challenges of the Near-Earth Propagation Environment 10
1.3.1 Large-scale path loss 11
1.3.2 Small-scale fading 11
1.4 Previously Unconsidered Near-Earth Propagation Phenomena 12
1.5 Modeling the Near-Earth Refractive Channel 18
1.5.1 Limitations of PE Models for Near-Earth Applications 18
1.5.2 Limitations of Ray-Based Models for Near-Earth Applications . . 21
1.5.3 Revisiting an Old Approach: Sommerfeld Integrals 23
1.6 Dissertation Outline 26

CHAPTER 2 SPECTRAL DOMAIN AND SOMMERFELD INTEGRAL METHODS 28
2.1 Problem Geometry and Mathematical Model 32
2.2 Spectral Domain Formulation 35
2.3 Boundary Conditions at the Interfaces 36
2.4 The Spectral Domain Solution 37
2.4.1 Spectral Domain Solution Example in Five Layers 38
2.5 Integration of the Spectral Domain Solution: The Sommerfeld Integral . . 41
2.5.1 Poles and Guided Modes 42
2.5.2 Guided Mode Extraction 43
2.5.3 Oscillations and Asymptotic Quadrature 44
2.6 The Full Quadrature Algorithm 46
2.6.1 Integration Interval Finite Truncation and Subintervals 47
2.7 Calculating all Fields and Received Power 51
2.8 Numerical Experiments and Verification 57
2.8.1 Comparison with Image-Theory Solutions 64
2.8.2 Performance Under Coordinate Transformation 67
2.8.3 Conclusion 71

CHAPTER 3 COMPARISONS OF SOMMERFELD INTEGRAL MODEL AND MEASURED DATA 72
3.1 Description of the Measurements 72
3.2 Radiofrequency Data Collection Results 73
3.3 Atmospheric Data Collection Results 74
3.4 Stochastic Treatment of the Atmospheric Profiles 75
3.4.1 Time-Averaging the Atmospheric Data 77
3.5 Estimating Continuous Atmospheric Profiles from Measurements 79
3.5.1 Temperature and Humidity Profiles in the Surface Layer 80
3.5.2 Examining the Fitted Profiles 85
3.6 RF Simulation Results 89
3.7 Interpretation of Results and Discussion 91

CHAPTER 4 REFRACTIVE CONDITIONS AND EFFECTS ON LONG RANGE PROPAGATION 94
4.1 Introduction 94
4.2 Refractive-Gain in Measured Conditions 95
4.3 Shape-preserving Atmospheric Gradient Amplification 97
4.4 From Gradient Amplification to Physical Conditions 101
4.5 Propagation in Extremal Refractivity 104
4.6 Effect of Ground Conductivity 105
4.7 Effect of Frequency Scaling 116

CHAPTER 5 CONCLUSIONS AND FUTURE DIRECTIONS 126
5.1 Supporting Publications 130

APPENDIX A MAXWELL'S EQUATIONS AND MATHEMATICAL CONVENTIONS 131

APPENDIX B FOURIER TRANSFORM OF CYLINDRICALLY SYMMETRIC FUNCTIONS: HANKEL TRANSFORM 133

APPENDIX C ATMOSPHERIC BOUNDARY LAYER DEFINITIONS 135
C.1 The Reynolds Decomposition and Expectations 136
C.2 Variances and Covariances 137
C.3 The Obukhov Length and Monin-Obukhov Parameters 139

APPENDIX D TROPOSPHERIC PRESSURE PROFILE 140

REFERENCES 141

LIST OF TABLES

Table 1 **Refractive Gradients and Conditions. Adapted from [1].** 15

LIST OF FIGURES

Figure 1 The classical Sommerfeld problem. 5

Figure 2 Geometry motivating the Friis model. 9

Figure 3 Model refractivity in the troposphere 15

Figure 4 Measured near-Earth refractivity 16

Figure 5 Spurious Reflections in TEMPER 20

Figure 6 Three examples of human intuition about light propagation. 22

Figure 7 Geometry of multilayered PCBs and air/ground models 26

Figure 8 Several 2D Fourier Basis Functions 29

Figure 9 Example of Quadrature 30

Figure 10 The model used for the physical environment. 34

Figure 11 Illustration of the Spectral Domain Solution. 40

Figure 12 Pole Extraction Illustrated. 45

Figure 13 The integration algorithm on a subinterval. 48

Figure 14 Branch-Cuts in the k_ρ-plane 50

Figure 15 SDGF at a Branch-Point 50

Figure 16 Nine-Point Grid for Finite Differences 54

Figure 17 Radial Derivative Finite Difference Grid 55

Figure 18 Height Derivative Finite Difference Grid 55

Figure 19 Mixed Derivative Finite Difference Grid. 55

Figure 20 Comparison of SI Method with Free-space Solution 59

Figure 21 Comparison of SI Method with Branch-Point Subtraction and Free-space Solution 63

Figure 22 Image theory for PEC planes 65

Figure 23 Comparison of SI Method with Image Theory 66

Figure 24 Coordinate Transformations of Fields 68

Figure 25 SI Calculations above Curved Earth 70
Figure 26 Received Power, 8/23/2009, Panama City, FL 74
Figure 27 Temperature, 8/23/2009, Panama City, FL 75
Figure 28 Relative Humidity, 8/23/2009, Panama City, FL 76
Figure 29 Temperature time derivative autocorrelation 78
Figure 30 Averaged temperature time derivative autocorrelation 79
Figure 31 Illustration of how the eddy size is limited by proximity to the surface . . 83
Figure 32 Measured relative humidity vs. height along with fitted profiles 87
Figure 33 Humidity profile fit errors for 8/23/2009 87
Figure 34 Measured temperature vs. height along with fitted profiles 88
Figure 35 Temperature profile fit errors for 8/23/2009 88
Figure 36 Error between humidity measurments and fit values over time 90
Figure 37 Contour plot of simulated RF power on 8/23/2009 92
Figure 38 Simulated RF power at 70 m on 8/23/2009 92
Figure 39 Simulated Refractive Gain, Measured Profile 95
Figure 40 A Refractive Profile 97
Figure 41 Simulated Refractive Gain, 5x Gradient 98
Figure 42 Simulated Refractive Gain, 10x Gradient 98
Figure 43 Simulated Refractive Gain, 50x Gradient 98
Figure 44 Simulated Refractive Gain, 100x Gradient 99
Figure 45 Simulated Refractive Gain, 500x Gradient 99
Figure 46 Simulated Refractive Gain, 1000x 99
Figure 47 Refractive Gain Along Ground Level 100
Figure 48 Maximal Refractive Gain Along Ground Level vs. Gradient Strength . . 100
Figure 49 Physically realizable best-fit to 100x gradient amplification. 103
Figure 50 Received Power in Extreme but Physically Realizable Conditions 105
Figure 51 Refractive Gain in Extreme but Physically Realizable Conditions 106

Figure 52 Conductivity Sweep 1, Received Power 108
Figure 53 Conductivity Sweep 2, Received Power 108
Figure 54 Conductivity Sweep 3, Received Power 108
Figure 55 Conductivity Sweep 4, Received Power 109
Figure 56 Conductivity Sweep 5, Received Power 109
Figure 57 Conductivity Sweep 6, Received Power 109
Figure 58 Conductivity Sweep 7, Received Power 110
Figure 59 Conductivity Sweep 8, Received Power 110
Figure 60 Conductivity Sweep 9, Received Power 110
Figure 61 Conductivity Sweep 10, Received Power 111
Figure 62 Conductivity Sweep 11, Received Power 111
Figure 63 Conductivity Sweep 1, Refractive Gain 112
Figure 64 Conductivity Sweep 2, Refractive Gain 112
Figure 65 Conductivity Sweep 3, Refractive Gain 113
Figure 66 Conductivity Sweep 4, Refractive Gain 113
Figure 67 Conductivity Sweep 5, Refractive Gain 113
Figure 68 Conductivity Sweep 6, Refractive Gain 114
Figure 69 Conductivity Sweep 7, Refractive Gain 114
Figure 70 Conductivity Sweep 8, Refractive Gain 114
Figure 71 Conductivity Sweep 9, Refractive Gain 115
Figure 72 Conductivity Sweep 10, Refractive Gain 115
Figure 73 Conductivity Sweep 11, Refractive Gain 115
Figure 74 Refractive Gain at a Point Across ε_r'' 116
Figure 75 Total Fields in a Waveguide 117
Figure 76 Long-Range Power at 3.00000 GHz 119
Figure 77 Long-Range Power at 5.24259 GHz 120
Figure 78 Long-Range Power at 9.37715 GHz 120

Figure 79 Long-Range Power at 16.77243 GHz 120
Figure 80 Long-Range Power at 30.00000 GHz 121
Figure 81 Long-Range Refractive Gain at 3.00000 GHz 122
Figure 82 Long-Range Refractive Gain at 5.24259 GHz 122
Figure 83 Long-Range Refractive Gain at 9.37715 GHz 123
Figure 84 Long-Range Refractive Gain at 16.77243 GHz 123
Figure 85 Long-Range Refractive Gain at 30.00000 GHz 123
Figure 86 Refractive Gain at Ground Level Across Frequencies 125

LIST OF SYMBOLS

ε_0	Vacuum permittivity constant
ε_r	Relative permittivity; further subscripts denote a layer in a multilayered medium
j	The imaginary unit, $\sqrt{-1}$
λ_0	Free-space wavelength
μ_0	Vacuum permeability constant
ω	Radian frequency
$H_0^{(1)}$	Hankel function of the first kind and order zero
J_0	Bessel function of the first kind and order zero
$\cdot^*$	The complex conjugate operator
$\times$	The vector cross-product
$\mathbb{E}[\cdot]$	Expectation operator
$\Re[\cdot]$	The real part operator
$\nabla\times$	Vector curl operator
$\nabla\cdot$	Divergence operator
∇	Gradient operator
$\mathbf{A}$	Time-harmonic magnetic vector potential
$\mathbf{E}$	Time-harmonic electric field
E	Time-harmonic electric field; subscripts denote components in cylindrical coordinates

$\mathbf{H}$ Time-harmonic magnetic field

H Time-harmonic magnetic field; subscripts denote components in cylindrical coordinates

φ Scalar electric potential

$\mathbf{S}$ The time-averaged Poynting vector of a time-harmonic electromagnetic field

S_ϕ The ϕ-component of $\mathbf{S}$

S_ρ The ρ-component of $\mathbf{S}$

S_z The z-component of $\mathbf{S}$

$\tilde{A}_z$ z-component of the spectral domain magnetic vector potential

A_z z-component of the spatial domain magnetic vector potential

$\tilde{A}_{z\ell}$ z-component of the spectral domain magnetic vector potential in layer ℓ

G_{refract} Refractive gain

$\tilde{I}_{z0}$ z-directed linear current density flowing through source dipoles

k_ℓ Wavenumber in layer ℓ

k_{p} A wavenumber in the spectral domain functions at which a pole occurs

k_ρ Radial wavenumber measured outward from the source in cylindrical coordinates

k_x x-wavenumber

k_y y-wavenumber

$k_{z\ell}$ z-wavenumber in layer ℓ

ℓ An index for the layers in a multilayered medium

L Total number of layer interfaces in a multilayered medium

n_ℓ Complex index of refraction in layer ℓ

ϕ Azimuth angle in a cylindrical coordinate system

P_{RX} Received power

ρ Radial range measured outward along the ground from the origin

$R_\ell^\pm$ Upward and downward generalized reflection coefficient in layer ℓ

z Height measured along the z-axis

z' Source height, measured along the z-axis

z_ℓ Height of the ℓ^{th} interface in a multilayered medium

α Gradient amplification

e Partial pressure of water vapor in a mass of air, or Euler's number $e \approx 2.71828\ldots$

k The von Karman constant

L Obukhov length

N Scaled refractivity

n Index of refraction

P Pressure

Φ_H Monin-Obukhov universal function for temperature

Φ_W Monin-Obukhov universal function for water vapor

q Specific humidity

q_* Surface friction humidity

T Absolute temperature

θ Potential temperature

θ_* Surface friction potential temperature

T_* Surface friction temperature

u_z Upward wind-speed

SUMMARY

The design of emergent wireless sensor networks operating near the ground requires channel models that account for previously unconsidered propagation phenomena. Most models used for link planning and radio design of the last century were designed for use in situations where the transmitters were at least tens of meters above the earth surface. However, near the earth surface, the specifics of the ground composition and atmospheric effects have been postulated to play a significant role. This dissertation describes the first set of investigations in this emergent environment. A novel computational electromagnetics model is presented that can calculate electromagnetic fields of a dipole embedded in planar-stratified propagation medium that represents the ground and near-surface atmosphere. It is the first available electromagnetic model to efficiently combine a spectral-domain solution in arbitrary multilayers of lossy-dielectric media with high-order quadrature routines to synthesize the fields of an impressed dipole. For the first time, high-order asymptotic quadrature is used to efficiently obtain solutions at arbitrary ranges from the dipole source. A measurements-based model of the near-ground atmosphere is derived, and results of modeling the atmosphere are used to predict the performance of an ultra-high-frequency radio system operating near the ground surface. Finally, a study is conducted to determine the effects of varying key parameters in the near ground channel, including atmospheric conditions, ground conditions, and frequency. Specific contributions of this dissertation are:

- The first Sommerfeld-integral-based mathematical and computational model of long-range EM propagation in multilayered media excited by time-harmonic vertical dipole sources.

- A simple measurements-based modeling and curve-fitting methodology for determining continuous atmospheric profiles for temperature, humidity, and refractivity near the surface of the earth.

- A measurements-based case-study of UHF propagation in a near-ground refractive environment.

- A study of the parameters that affect general RF propagation in near-ground atmospheric refractivity.

This work in this dissertation allows for the determination of the conditions under which atmospheric effects significantly affect the near-ground propagation environment when the transmitter is a vertical dipole. In flat ground conditions outdoors, the model also allows for the direct, accurate prediction of propagation effects in a narrowband wireless channel.

This dissertation also leads to several new directions for future research in outdoor channel modeling from an electromagnetics perspective. The model can be extended to represent general wideband waveforms specified in the time-domain, made possible using Fourier synthesis techniques. The method of coupling a spectral-domain solution in a multilayer environment with advanced quadratures on Sommerfeld integrals can directly be applied to related extensions of the problem geometry, including the effects of arbitrary antennas of arbitrary orientation. Once the fields of all types of antennas and sources can be calculated using the methodology, it will then be possible to model the effects of terrain and scatterers in the wireless channel.

CHAPTER 1

INTRODUCTION

Chapter Summary: This chapter is an introduction to the ideas underlying this dissertation. A historical overview of developments in long-range radio propagation is given, followed by examples of studies in the emerging near-earth wireless environment that motivate continued study of radio propagation. The most common methods for modeling long-range radio propagation found in the scientific literature are presented. Limitations of these methods in the near-earth environment are highlighted. Because of these limitations, spectral-domain methods are explored. They are postulated to lead to more accurate radio propagation models that do not suffer from the limitations of other methods highlighted in this chapter.

1.1 Motivation

In recent years, there has been increased research into wireless systems operating very near the Earth or ground surface. Applications have included agricultural sensing [2, 3, 4], intrusion detection [5, 6], and jamming near-Earth radios in a military context [7, 8]. Near ground RF communications systems operate within wavelengths of the surface, a domain that is generally not of interest in the study of radio propagation for radar, cellular, and communications applications that motivated the study of RF problems of the last century.

Some researchers in this new area have focused on identifying requirements for such next-generation sensor systems as in [2], while the authors of [3, 4] have experimentally deployed sensor networks operating at UHF frequencies for environmental sensing in support of agriculture. Global agricultural industries increasingly are the earliest adopters of near-Earth wireless systems. These industries have much to gain from adopting wireless technology; they can 1) increase crop yields, 2) prevent food spoilage, and 3) streamline the supply chain [9]. For the United States (US) military community, jamming near-Earth

remote controlled weapons (e.g., roadside bombs) efficiently and effectively can give the US military a tactical advantage against adversaries and lead to fewer successful attacks against US military personnel.

Both sensing and jamming applications can require radio transmitters to be placed near the Earth surface. In an agricultural context, sensors buried in the ground can measure soil moisture and temperature, and wirelessly transmit these data back to a base station. Similarly, a jamming device might be mounted a few feet above the ground on the side of a vehicle. Both of these systems could conceivably be power-constrained because they operate on battery power. Unfortunately, the propagation characteristics of the near-ground environment exacerbate these power limitations. As wireless nodes are moved closer toward the ground, they must generally consume more power to maintain a constant level of coverage or bit error rate. This demand for power by near-Earth nodes is because large-scale path loss and fading severity both increase with decreasing channel height. Section 1.3 discusses these effects in more detail and provides supporting references to the literature.

The other major proposed feature of near-Earth propagation is the presence of atmospheric effects. Several researchers associated with the US Navy have postulated that near-earth refractive structures can set up radio propagation ducts that guide waves along the surface of the earth [10, 11, 12]. The aforementioned emergent applications, along with postulated, previously unconsidered propagation effects, has motivated the development of a new physics-based computational model of radio propagation in the near-ground environment. The definitive conclusion of this work is that near-earth atmospheric structures play a significant role in radio propagation in the super high frequency (SHF) regime and above. In the ultra high frequency (UHF) regime typical of radio communication at the time of writing, the effects of atmospheric structures on received power in a narrowband channel are negligible.

1.2 History of Radio Propagation Modeling

The study of the propagation of radio waves has been of practical interest since the late nineteenth century, when James Clerk Maxwell presented his famous equations. Although in a mathematical form that would hardly be recognizable today, his theory of electricity and magnetism predicted the now well-known electromagnetic waves that propagate at the speed of light. The experimentalist David Edward Hughes was the first person to postulate that some observations of his were due to radio waves. In 1879, he observed that electrical sparks generated by switching a current source off could be detected all through his home by a telephone receiver connected to what we would recognize today as a crude Schottky diode. He was able to send and receive Morse code over hundreds of meters using these "invisible electric waves" [13]. More meticulous work conducted by Heinrich Hertz in 1886 and reported in 1893 [14] led to the general scientific acceptance of the reality of these electromagnetic waves. The commercial sector was soon to follow, leading to the wireless telegraphy and telecommunications era of the early twentieth century.

One of the first questions asked by early designers of radio communication systems was: "How far away can the receiver be and still receive the radio signal?" For systems employing simple amplitude modulation of a carrier frequency, they soon discovered that the answer to this question depends on a variety of factors:

- Transmitter power
- Carrier frequency
- Receiver sensitivity
- Antenna structure and orientation
- Antenna height above earth
- Transmission center frequency
- Obstructions between transmit and receive antennas

A given transmitter and receiver pair typically have a fixed transmitter power, carrier frequency, receiver sensitivity, and antenna structure; furthermore users of radio signaling generally have little control over the obstructions or conditions between the transmitter and receiver. The remaining parameters to vary are the heights, and radio pioneer Guglielmo Marconi found that raising the height of both transmit and receive antennas *increased* the maximum range of radio wave propagation proportional to the square of the height. This observation has been codified and named as Marconi's law, and represents the world's first practical radio propagation model. The model contains a constant of proportionality that must be determined in an optimal sense for a given radio configuration; this was done by Marconi and others by choosing the parameter that best fit the measured results, an approach that is still taken today in empirical radio propagation modeling.

Others quickly realized that these new radio systems were capable of sending and receiving signals around the Earth's curvature, well beyond the geometrical line-of-sight. In the search for a physical explanation for these observations, Zenneck [15] derived solutions to Maxwell's equations that had the form of a *surface-wave*. This is an electromagnetic disturbance that decays exponentially perpendicular to the interface between a conductive and non-conductive medium, and propagates parallel to the interface. Since these waves are coupled to the surface, surface waves were posited to follow the Earth's curvature and be the mechanism by which radio propagation occurred beyond the horizon. Arnold Sommerfeld continued these investigations in 1909 [16], and today his simplified model problem of long-range radio propagation above the Earth surface has come to be known as the *Sommerfeld problem*. A diagrammatic representation of the classical Sommerfeld scenario appears in Figure 1. The Helmholtz equations presented must hold in the volume of the media, a consequence of Maxwell's equations; additionally, continuity conditions must hold on the interface between the two media and the Sommerfeld radiation condition must be obeyed by the fields.

This problem was studied extensively throughout the twentieth century as a model for

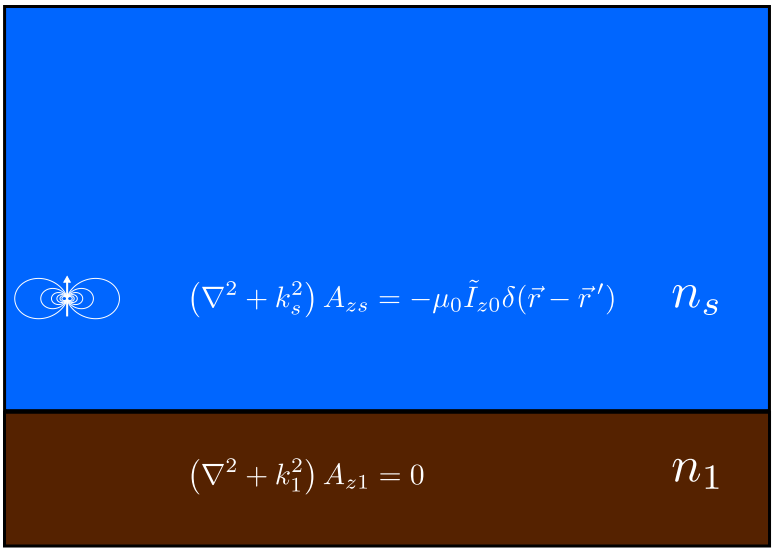

Figure 1: A small dipole carrying a spatial impulse of current radiates in the presence of an air/ground interface. Each medium is assumed to be homogeneous and of semi-infinite extent in this model. The governing equations for the z-component of the magnetic vector potential, A_z, in this geometry are indicated as well. See Chapter 2 for the precise definition of all symbols.

radio propagation over the earth or ocean surface [17, 18, 19, 20, 21, 22, 23]. The major differences between the Sommerfeld scenario and free-space propagation include two additional propagation mechanisms: a reflected wave, and the aforementioned surface waves that Zenneck thought explained radio propagation beyond the geometrical horizon. Most of the work done in this era was attempting to understand the nature of surface waves and their contribution to long-range propagation. While surface-waves can play a significant role in radio propagation, the effect is highly dependent on the frequency, range from the source, and source current distribution, as shown in [24]. Instead of surface waves, it is likely that the earliest investigators were seeing the now well-known effect of ionospheric propagation. In fact, the existence of the ionosphere was not experimentally confirmed until 1927; the ionospheric reflection of shortwave radio signals over long ranges back down to earth was not considered as a radio propagation mechanism until much later.

Methods for solving the long-range radio propagation problem in the presence of more general refractive conditions were studied throughout the twentieth century. The earliest

methods for these kinds of problems were closely related to Sommerfeld's approach, which might be characterized as a "spectral method" today. Spectral methods assume that the solution to the pertinent partial differential equation can be written as a superposition of basis functions that satisfy the equation inside a domain. The Fourier basis is often chosen when it is an eigenbasis of the underlying differential operators, meaning that differential operators are transformed into multiplications by the eigenvalues. In simple terms, the entire problem is Fourier-transformed in time and several, if not all, of the spatial variables. The resulting problem in the spectral domain becomes algebraic in character, because the partial derivatives reduce to multiplication by constants. In the spectral domain, the algebraic problem can be solved using standard linear algebra techniques. Then the original superposition representation could be calculated, giving the solution. Superposition integrals of this spectral type in planar multilayer media have come to be known as Sommerfeld integrals (SIs). In practice, SIs do not yield closed form integrals in the general case. The earliest investigators looked to extract some dominant terms in a closed form, for some simplified geometries. For example, in [25], propagation over realistic ground was investigated using spectral methods in the Sommerfeld model problem. Solutions to these problems were found in which the various spectral integrals are approximated by asymptotic series that capture the limiting behavior of the solution very near or very far away from the localized sources. These approximations were quite useful in that they represent the solution as a sum of terms, each of which corresponds to a wave that is understood in physical terms, such as a direct wave, ground reflected wave, surface wave, and guided waves. After the asymptotic terms are extracted, there is of course still a residual integral term that represents corrections to the asymptotic solution. The earliest approaches neglect this residual integral contribution as an approximation.

Another kind of asymptotic solution that was explored early on was *ray-tracing* or the geometrical optics (GO) approximation. GO results from deriving wave mechanics in the asymptotic limit of infinite frequency. In this limit, electromagnetic wave phase fronts

propagate in the direction of rays, which are paths along which electromagnetic energy is transferred. The most simplified approach in this school of thought is the two-ray model, in which the fields are calculated as the sum of the contribution of two rays, a direct one and a reflected one from the ground. More complicated approaches that trace rays through atmospheric inhomogeneities saw some limited use in propagation modeling throughout the 1960s and 1970s, particularly in the military radar community [26]. This technique gained much more traction for long range propagation predictions in the acoustic wave propagation community for underwater sonar applications, and today several ray-tracing codes can be found for ocean acoustics problems, including [27, 28]. Ray approaches are also popular today in commercial modeling products targeted towards cellular network operators, who must model the effects of buildings and terrain in order to calculate cellular tower coverage; an outline of some available products for this purpose, many of which include ray-tracing engines, is included in [29].

Throughout the 1970s and early 1980s, the *parabolic equation* (PE) method was rediscovered for EM propagation. Although Leontovich and Fock [30, 31] were the first to apply the parabolic approximation to long range radio propagation problems in the 1940s, Hardin and Tappert popularized the technique in the 1970s for general wave propagation [32] and for applications in non-linear fiber optics [33]. This method approximates the hyperbolic partial differential equation (PDE) that governs wave mechanics by a parabolic PDE. Parabolic PDEs have the property that they are amenable to "marching methods" in which given boundary conditions can be propagated in a simple way into the problem domain to calculate the solution away from the boundary. This interior solution does not in any way couple to the solution back towards the boundary, and so this approximation represents a *one-way wave equation*. For long range propagation, backscatter from the environment to the transmitter is typically not of interest and this effect is not dominant except in the case of steep terrain; therefore, one-way wave-mechanics are considered an acceptable approximation. While ray-based approaches dominate the commercial cellular sector,

PE-based models are most popular in the radar community; a selection of implementation details of PE methods from the last decade appear in [34, 35, 36, 37, 38, 39, 40, 41].

Although the GO and PE methods are the current standard techniques used in long-range electromagnetic propagation modeling in the cellular and radar communities, respectively, other techniques have been developed and applied to the long-range RF propagation problem. Notably absent from the previous discussion are the methods that directly discretize the original Maxwell's equations or their time-harmonic equivalent, such as the finite difference family and finite element methods. While the PE does directly discretize and solve a differential equation, it is not an exact wave equation, but an approximate equation using the paraxial assumption. Direct discretization of wave equations are typically infeasible for use in long range problems because the number of unknown parameters or field values to be solved for increases in proportion to the volume of the domain to be simulated, which becomes intractable for large problems. One method in this family, however, *has* been modified to overcome this limitation: the finite difference time domain (FDTD) method has been adapted to simulate only the spatial region around an EM pulse as it propagates, so that the volumetric domain of simulation is of a fixed size around the propagating pulse irrespective of the overall domain size and shape. This is known as the moving window finite difference time domain (MWFDTD) method, and has seen limited use in simulations of long range RF propagation over terrain [42, 43, 44, 45].

Finally, the historical development of the class of phenomenological, empirical, and stochastic propagation models bears mention. The earliest of these methods that is still in use today is the "Simple Transmission Formula" presented by Friis in 1946 [46], which is, at the time of writing, taught in classrooms around the world as a basic free-space propagation model. This falls in the class of phenomenological models because, although it is consistent with and can be reconciled with the physics of Maxwell's equations in its domain of validity, it was not derived directly from the fundamental theory. Friis, and many others before him, used geometrical reasoning about how electromagnetic power must spread

out geometrically over the surface of a sphere centered on a transmitter. The surface area of such a sphere increases in proportion to the square of its radius, r. Combined with the physical principle of conservation of energy, it can be concluded that electromagnetic power available at a receiver decreases as the square of the distance from the transmitter, or as $1/r^2$. The Friis formula also incorporates antenna gain effects in geometrical terms of an effective aperture that captures the incident EM energy in proportion to its area. The geometrical reasoning is depicted in Figure 2.

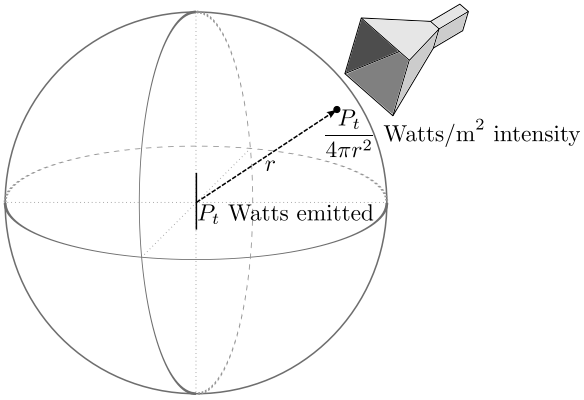

Figure 2: A short source radiates a finite amount of power that spreads out uniformly over the surface of a sphere. At a distance r, the sphere has area $4\pi r^2$ and so Friis reasoned that the input power P_t must all be conserved and spread out over the surface of the sphere. The local power intensity of the transmitted wave at the receiving antenna (power per unit area) must therefore be proportional to the ratio of the total radiated power and the surface area of the sphere. This leads to a received power that is proportional to $\frac{P_t}{4\pi r^2}$. Accounting for the antenna effective apertures (e.g., of the horn receiver in the picture) results directly in Friis' original formulation.

The Friis formula can be derived rigorously from Maxwell's equations in the far-field of radiators or from the precepts of GO theory. The aforementioned two-ray model is another GO-based simple model that predicts that a reflected wave from the ground interferes with the wave that travels directly between the transmitter and receiver. In the two-ray model, the far-field power falls off as the inverse *fourth* power of distance, or as $1/r^4$ [47]. The work of [48] provides an extensive study of these phenomenological ideas from a rigorous electromagnetics perspective. Both the Friis formula and the two-ray formulas have a power vs. distance characteristic that obeys an inverse power law, $1/r^n$, for $n = 2, 4$.

An empirical extension then is to allow n to take on other values, and perhaps choose a "best-fit" value of n from measured empirical data. When this is done, n is called the path loss exponent and such models are generally called log-distance path loss models [47]. The results of experimental RF propagation campaigns are often reported in terms of path-loss exponents over certain paths. There is a large body of measurement literature that presents log-distance path loss results for outdoor channels, with reported path loss exponents n between 3 and 6; a selection of recently reported results of this type include [49, 50, 51, 52]. Other empirical models have been presented with a piecewise approach, where the path loss exponent can take on one of several values depending on the range from the transmitter. Finally, yet other empirical models that fit into the log-distance family have been presented, with fine-tuned constants chosen to fit measurement campaigns in specific areas, or accounting for additional propagation effects such as diffraction. These are treated in detail in [47].

1.3 Unique Challenges of the Near-Earth Propagation Environment

Terrestrial wireless systems operating in the VHF and UHF bands deployed to date have typically had transmitters tens to hundreds of meters above the ground. Tall radio towers hosting transmitting antennas are a ubiquitous sight across most of the world. These provide services such as terrestrial broadcast television, FM radio, cellular voice, and mobile data service. Less common radio frequency systems that use high transmit antennas are radar systems for air traffic control, weather monitoring, and defense. In [53], the authors found that cellular UHF systems may be optimized by placing the transmitter 30-40m above the terrain surface, while the Radiocommunication Sector of the International Telecommunication Union(ITU-R) implicitly recommends in [54] that point-to-area systems should operate with transmitters at least 10m off the ground over the entirety of both the VHF and UHF bands. These patterns and recommendations of high antenna placement are due to two factors. Firstly, the large-scale path loss of a far-field channel increases with

decreasing transmitter antenna height. Secondly, small scale fading becomes more severe as transmitter height decreases. The reasons why both large-scale and small-scale channel behavior changes with decreasing channel height are elucidated in the remainder of Section 1.3.

1.3.1 Large-scale path loss

As previously mentioned, large-scale path loss increases with decreasing antenna height in a near-Earth radio channel. This can be attributed to the following factors: two-ray propagation [55, 48]; rough surface scattering and shadowing of the wave off of ground features and clutter [56, 57, 58, 59]; and antenna-ground coupling effects [60, 61, 62]. These effects have been reported in the literature in both indoor and outdoor measurements. For example, the authors of [63] found that in an indoor UWB channel, a link separated by 2m of distance incurs 7dB of additional path loss as the antennas are lowered from 1m to ground level. In a mixed indoor/outdoor environment, the authors of [64] found a maximum of 16.8 dB additional loss incurred by moving lower to the ground. The same trend has been observed in data collected as part of the present work, as presented in the proposal for the present work [65]. Such results seem to be a direct consequence of the effect of destructive interference from a ground reflection, a behavior that is captured by the two-ray model.

1.3.2 Small-scale fading

Small-scale fading is often described in terms of statistical distributions that provide the probability density of a received signal. The Rician K-factor, which is the ratio of specular power to diffuse power in a wireless channel [66], is taken as a figure-of-merit in analyzing fading severity. When this ratio is relatively high, there are fewer diffuse scattered field components in a received signal. This leads to a more stable signal that does not fade in and out with small changes in receiver position. On the other hand, when the K-factor is small, the diffuse field components are relatively large compared to the dominant component and

therefore have a larger effect. This causes wider fluctuations in the total signal even under small changes in receiver position.

In general, as antenna height is decreased, the environment through which the RF energy propagates becomes more cluttered, causing diffuse RF energy to propagate from transmitter to receiver. This increase in diffuse energy corresponds to increased fading severity. Recent experimental work has shown this to be true in the near-ground link compared to traditional point-to-area links with large transmitter heights. The authors of [67] found that lower height channels have lower Rician fading parameters. They relate channel K-factors with height through a simple power-law. Joshi et al. [68] also observed the Rician K-factor to decrease with decreasing antenna height in a 300 MHz outdoor line-of-sight link. Finally, foliage and vegetation commonly occlude the near-Earth link, and this vegetation moves in the wind. The wind serves to aggravate the problem by inducing motion in the scattering vegetation, which has been observed to cause more fading in near-ground channels [69, 70].

1.4 Previously Unconsidered Near-Earth Propagation Phenomena

The previous section demonstrated that near-Earth UHF wireless channels exhibit more loss and more severe fading than traditional large-height point-to-area systems of the past. The mechanisms that cause these effects were also identified. The present work considers previously unconsidered propagation mechanisms in the near-Earth channel, namely, the effects of atmospheric refractivity. The index of refraction of air depends weakly on its temperature, humidity, and pressure [71, 72]; this will generally affect propagation through refractive bending of wave paths. In [71], Smith and Weintraub provide a review of the empirical equations relating the index of refraction of air to atmospheric temperature, pressure, and humidity. They present an equation that is valid in the UHF regime of the form

$$N = (n-1) \times 10^6 = K_1 \frac{P}{T} + K_2 \frac{e}{T} + K_3 \frac{e}{T^2} \quad , \tag{1}$$

where n is the index of refraction of air, P is the pressure of the air, T is the absolute temperature of the air, e is the partial pressure of water vapor in the air, and (K_1, K_2, K_3) are dimensioned constants. Because N is a unitless ratio, P, T, e, can be expressed in any pressure and absolute temperature units, so long as the constants (K_1, K_2, K_3) are appropriately scaled. When all pressures and temperatures are expressed in millibars and kelvins, respectively, the constants are $K_1 = 77.6$ K/mbar, $K_2 = -6$ K/mbar, and $K_3 = 3.75 \times 10^5$ K^2/mbar [71]. The form of Equation 1 is based on physical considerations, while the constants (K_1, K_2, K_3) were empirically determined through experiments. Finally, Equation 1 is not frequency-dependent; the refractivity of air is approximately constant across the broad range of frequencies 0-30 GHz according to [71].

The way in which the index of refraction appears as $N = (n - 1) \times 10^6$ is because there is a weak dependence of the index of refraction on the specified atmospheric conditions. In many circumstances, air is approximated by a medium that has an index of refraction value identical to the free space value of 1. The quantity $(n - 1) \times 10^6$ captures the parts-per-million deviation between the index of refraction of free space and of air with a specified pressure, temperature, and water vapor content. The quantity N is often known as the scaled refractivity, or simply as the refractivity when context makes the choice of units obvious. Another common convention is to describe scaled refractive quantities as being in "N-units."

Solar heating of the Earth is known to drive temperature and humidity gradients in height over the first few meters of the Earth (see, e.g., [73]). This, combined with Equation 1, creates refractivity gradients along the Earth in an outdoor environment. Refractivity gradients should affect the propagation characteristics of such a channel. Conventional systems of the past, however, generally have had high transmitters, typically at least 10 meters above the local ground surface, as evidenced by the recommendations of [54]. It appears that no work has been published which tries to study the impact of these gradients in the near-Earth environment.

Designers and operators of high-transmitter systems also only needed to account for these refractive effects when the links were relatively long. The effects of weak atmospheric variations in refractivity require long distances to accumulate. In particular, these effects must be accounted for in long range radars operating in maritime environments. If refractive effects are not considered in maritime radar applications, incorrect ranges to targets can result [74, 75, 76]. However, in the experimental work of Chapter 3, refractivity gradients were measured within the first meter of the ground that are much larger in magnitude than the conventional gradients seen in maritime radar propagation; this suggests that for the near-Earth environment, refractive gradients should be considered when evaluating propagation.

To compare high-transmitter scenarios (e.g., 30 m high transmitters at VHF/UHF frequencies) to typical near-Earth scenarios, consider the International Standard Atmosphere model [77, 78], which predicts that temperature in the troposphere decreases linearly with height (up to about 11 km) through the relationship $T(z) = T_0 - Lz$, where $T(z)$ is the temperature as a function of altitude z, L is a constant temperature lapse rate (typically taken to be 6.5 K/km) and T_0 is the surface temperature. Using this model and a few physical arguments (outlined in Appendix D), the pressure depends on height through

$$P(z) = P_0 \left(1 - \frac{Lz}{T_0}\right)^{g/(RL)} ,$$

where $P(z)$ is the pressure as a function of height, P_0 is the surface pressure, L and T_0 retain their previous meanings, g is the standard acceleration due to gravity near the Earth's surface, and R is the specific gas constant of air. Neglecting the effect of water vapor, inserting this temperature and pressure into Equation 1 results in a refractivity profile of the form

$$N(z) = \frac{K_1 P_0}{T_0 - Lz} \left(1 - \frac{Lz}{T_0}\right)^{g/(RL)} .$$

Plots of this model equation $N(z)$, and its gradient $N'(z)$ appear in Figure 3 for a standard atmospheric surface pressure $P_0 = 1013.25$ mbar and a range of surface temperatures

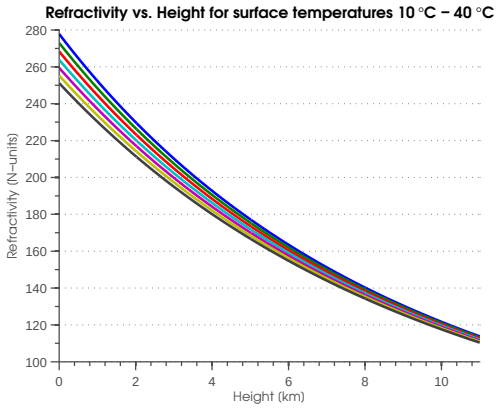

(a) An example of a family of tropospheric refractivity profiles for various surface temperatures, mostly driven by atmospheric pressure drop with altitude

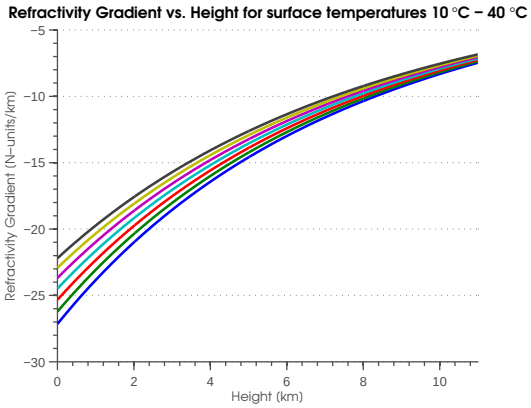

(b) The gradient in height of the figure at left

Figure 3: Refractivity and its height gradient are plotted; the order of N is hundreds of units, while the order of the gradient is negative tens of N-units per kilometer. The line represents the refractive profile (left panel) or refractive gradient profile (right panel) for seven surface temperatures between 10°C and 40°C.

corresponding to T_0 in the 10°C to 40°C range. The refractivity is in the hundreds of N-units in Figure 3a. The refractivity gradient dN/dz is in the negative tens of N-units per km in Figure 3b. This case very roughly encapsulates the kind of atmosphere that is considered a standard condition in studies of tropospheric radar propagation. In the radar literature, a typical standard atmosphere is one with an N gradient of -40 N-units/km [79, 80, 81]. This value is approximately the center of the what is considered the "normal" range, $(-79, 0)$ N-units/km. A table defining the refractivity gradient ranges typically discussed in the radar literature appears in Table 1.

Table 1: **Refractive Gradients and Conditions. Adapted from [1].**

	N-gradient
Trapping	< -157 N-units/km
Superrefractive	-157 to -79 N-units/km
Normal	-79 to 0 N-units/km
Subrefractive	> 0 N-units/km

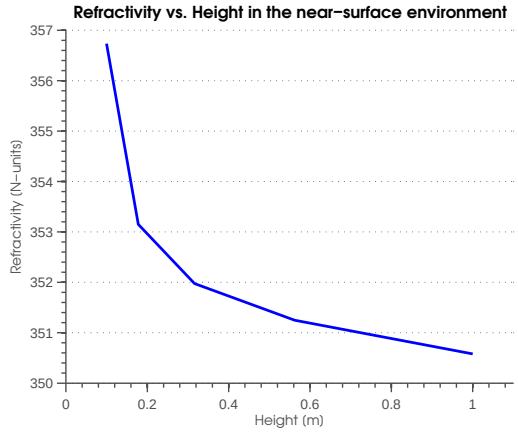

(a) Refractivity vs. height near the Earth surface

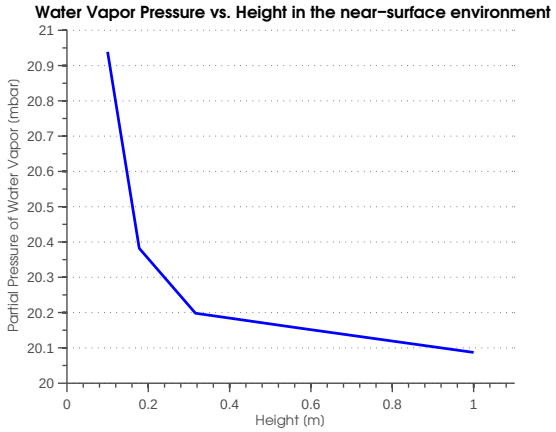

(b) Water vapor pressure vs. height near the Earth surface

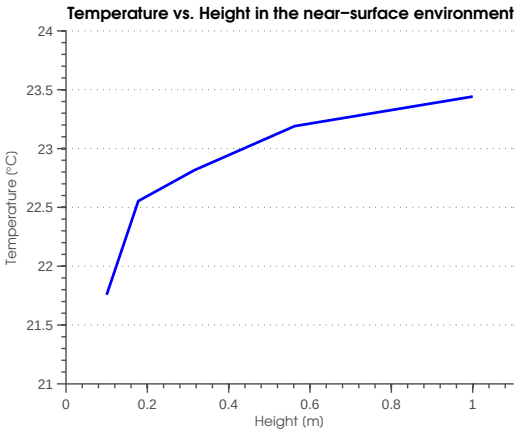

(c) Temperature vs. height near the Earth surface

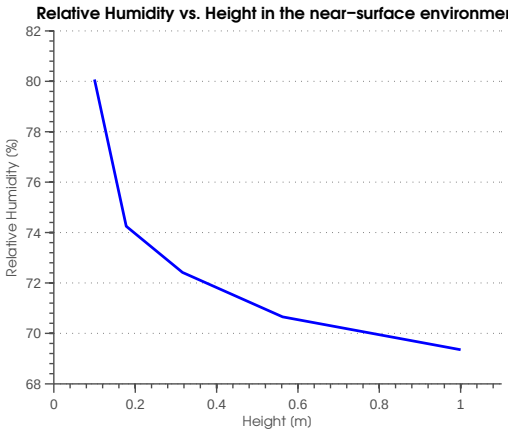

(d) Relative humidity vs. height near the Earth surface

Figure 4: Plots of measured near-Earth refractivity, water vapor pressure, temperature, and relative humidity appear above. The data were captured using a tree of five combined relative humidity/temperature sensors as part of the measurements described in Chapter 3. The relative humidity/vapor pressure of water drive the behavior of the refractivity.

The ranges in Table 1 are explained as follows. When the gradient is strictly positive, the atmosphere is "subrefractive", indicating that radio paths will be bent upwards from the straight line path they would follow otherwise. In "normal" and "superrefractive" conditions, the gradient is somewhat negative, and radio paths bend downwards from the expected straight line path. However, the radius of curvature of the radio path in normal and superrefractive conditions is not small enough to follow the curvature of the earth. The most extreme condition, known as "trapping", occurs when the refractivity gradient is quite negative, less than -157 N-units per km. The corresponding radio paths will be strongly bent downwards on earth-sized length scales. If fact, the radius of curvature of the radio path will be smaller than the curvature of the earth, meaning that such a path will intersect the earth, where it might be reflected upwards. The upward path can again refract downwards and intersect the earth, and this process may repeat many times, trapping the radio wave in a waveguide formed by the earth surface and refractive atmosphere. The trapping threshold value (-157 N-units per km) contrasts greatly with the measured atmospheric conditions and refractivity profile near the Earth, as seen in Figure 4.

The figure shows time-averaged height-profiles of refractivity, water vapor pressure, temperature, and relative humidity from six hours of measurements conducted during the late-night/early-morning hours between August 22 and August 23, 2009, in Panama City, FL, as part of the work presented in Chapter 3. The major features contributing to the refractivity are the temperature increase of about 1.75 degrees and the water vapor pressure decrease of about 1 mbar in the first meter. While in the tropospheric case the natural decline of pressure in altitude was the main driving force behind refractivity changes on the order of 10 N-units per km, here it is seen that humidity is in fact driving much stronger gradients in the near-Earth atmosphere. Indeed, it is worth noting that Equation 1 is such that a 1 mbar change in atmospheric water vapor pressure introduces about 4 N-units of refractivity change when the temperature is 25°C. Also, unlike the tropospheric scenario, the scale is not over kilometers of height; the refractivity changes several N-units per meter.

The near-Earth gradient is on the order of *thousands* of N-units per kilometer, a result that is extreme compared to the gradients considered "trapping" in tropospheric scenarios. The extreme observed gradient is the primary motivating factor in studying atmospheric effects near the ground. Since a qualitatively much weaker gradient has been known to affect long range propagation in the tropospheric scenario, it is desired to understand the impact of much stronger gradients in a refractive channel of a different scale.

1.5 Modeling the Near-Earth Refractive Channel

The previous section demonstrated that near-earth wireless channels are different from classical long-range radio channels in both scale and refractive character. The models that were developed throughout the twentieth century, as outlined in Section 1.2, were designed for various applications, with varying degrees of support for propagation prediction over terrain or in the presence of refractive effects. Those models typically focused on channels of tens to hundreds of kilometers of range and kilometers of height, operating in typical tropospheric gradients. On the other hand, the near-earth channel of interest is only meters tall and hundreds of meters long, and had demonstrably much stronger refractive gradients over this shorter height. These factors make some of the previously mentioned propagation models unsuitable to direct application in the near-earth environment. The remainder of this section will outline the limitations of two such approaches (the PE and GO techniques), and introduce the primary modeling technique used in this dissertation (the spectral domain/SI approach).

1.5.1 Limitations of PE Models for Near-Earth Applications

The PE-based models are from the family of direct discretization methods, based on approximating differential operators on a discrete, finite grid of spatial points. All of these methods approximate an unbounded domain by a truncation to a finite computational domain. As such, they all share the problem of handling boundary conditions at the truncation boundary. The correct condition is that the simulated fields propagate as if the boundary

were not there. This can be achieved by a radiation boundary condition (RBC), where no fields enter the simulation domain through the boundary and no incident fields are reflected from the boundary back into the simulation domain. Formulating RBCs in a numerical simulation is often the most difficult part of a developing a finite-discretization algorithm.

Although a myriad of techniques exist for the implementation of approximate RBCs, in most PE models this is accomplished by extending the computational domain to be larger than the region of interest, and then introducing a fictitious lossy absorbing material layer in this extended region; the models in [82, 83, 36, 34] represent the major PE model codes in use today, and all use this approach. At the newly extended boundary, a simple boundary condition that is easy to implement can be applied since reflections off this boundary will propagate back through the lossy medium and be attenuated further. Any initial reflection off the absorbing material can be minimized by choice of the material parameters for a given configuration of domain size, frequency, and source geometry. This is the computational analog of the real world approach of applying RF absorbing material to the walls of an antenna chamber. Although the chamber is finite and will have standing electromagnetic waves excited by a radiator, applying an absorbing layer to the walls emulates a radiation condition because reflected fields are greatly diminished in amplitude, allowing measurements of free-space characteristics within a bounded volume.

An absorbing approximate RBC works quite well for PE models in tropospheric propagation scenarios, where the top of the region of interest is kilometers away from the radiating sources. The fields are naturally quite attenuated at these heights, and absorbing layer parameters can be tuned for the types of geometry in tropospheric problems to minimize reflections. However, it can be shown that the reflective properties of such a layer are strong functions of the incident angle of electromagnetic energy upon them; therefore the optimal absorber strongly depends on the geometric relations between the source, boundary, and domain length. PE models that were designed for tropospheric scenarios actually suffer from strong spurious reflections from the computational domain top boundary when

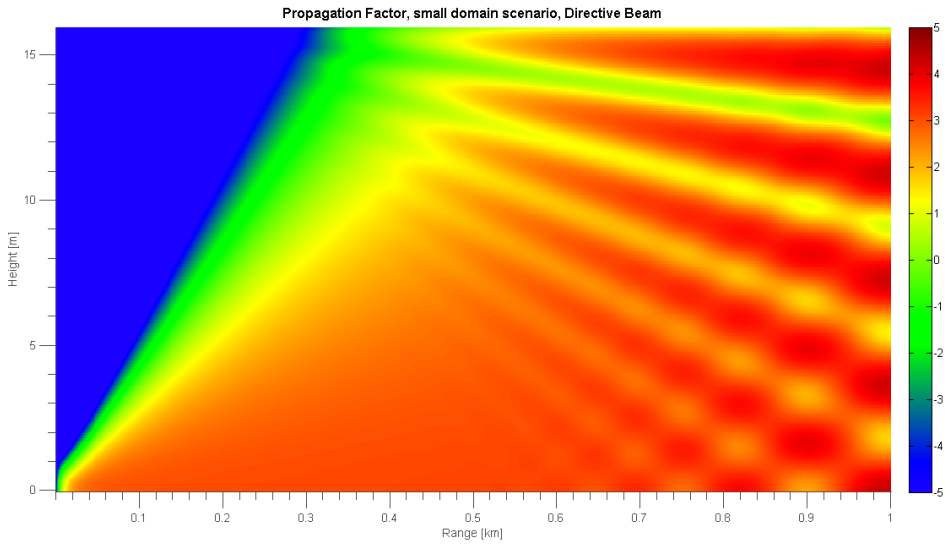

Figure 5: The TEMPER propagation model was used to simulate a domain 16 m in height. Interference patterns of peaks and nulls are visible in the propagation factor near the top of the plot, indicating that the top of the simulated domain is reflecting incident energy downwards. This is not the expected behavior of an RBC, and occurs because the absorbing layer in TEMPER was designed for domain boundaries that are at least hundreds of meters away from the sources.

applied to near-earth scenarios. An example of this effect is demonstrated in Figure 5, computed using the PE model software package known as TEMPER [36].

If the domain upper boundary were relatively far away from the sources, then the reflected fields would not have a large effect on the fields in the rest of the simulation domain. However, in a near earth scenario where the upper boundary is only several meters from the surface, the reflected fields interfere with the incident fields, making an interference pattern of peaks and nulls in the field strength that is characteristic of reflections. The problems are not localized to the top boundary: these reflections propagate back into the simulation domain and cause errors throughout. In the most extreme cases, the simulated fields lack the expected geometrical spreading in 3D that causes power to fall off as an inverse-square law. Because the fields are confined between the ground and the approximate RBC, they spread in 2D as cylindrical waves. The approximate RBC can lead to simulated domains that are very good waveguides, but not very good models of atmospheric propagation.

Current PE models for RF applications all seem to be tuned for large height scenarios; this is apparent in the implementation of the absorbing RBC at the domain top boundary. One might wonder if it is possible to implement alternative approximations to the RBC that are more general and applicable regardless of the propagation angle. Indeed, this has been extensively studied; a good outline of techniques including perfectly matched layers (PMLs) and non-local boundary conditions (NLBCs) for PE models is presented in the work of Levy [41]. Implementing these ideas is an attractive approach to modeling the near-earth propagation channel, since the PE is known for it's speed and computational efficiency. Such work is outside the scope of this dissertation, but might be considered as part of future research.

1.5.2 Limitations of Ray-Based Models for Near-Earth Applications

Ray-tracing approaches are quite attractive for near-Earth EM modeling due to their apparent conceptual simplicity. There is some "intuitive" understanding that accompanies these methods, likely due to the way humans experience visible light propagation in terms of shadowing, refractions, and reflections. This intuition is deeply embedded in our brains, and causes us to look up for clouds or planes when we experience a moment of darkness on a sunny day, to not be bothered by apparently discontinuous straws in glasses of water, and allows us to adjust our mirrors upon sitting down in an unfamiliar car without consciously thinking about which way we have to twist things in order to adjust the view. These intuitive ideas about light are depicted in Figure 6.

Because we know light is just a certain band of frequencies of EM radiation, we naturally use this intuition when reasoning about other frequencies such as RF. The ray analogy is used as the first explanatory tool in almost any treatment of propagation. Ray-tracing is generally illustrative and helpful for understanding the approximate path EM energy will take through a refractive structure. However, it can be difficult to use for practical power and field strength predictions. The mathematical connections between GO and full-wave

(a) An airplane shadow. We instinctively look up when this crosses our paths and occludes the sun, although the experience is of a darkening on the ground. This demonstrates the natural intuition we have about light propagation and shadowing.

(b) Light refracts through glass and water, creating an apparent break in the continuous straw. We so thoroughly intuit refraction that this apparent impossibility does not seem remarkable to us.

(c) Upon sitting in a car, the rear-view mirrors are adjusted typically with little conscious thought given to which way the mirror must be turned and twisted to manipulate the view in the desired way; such is the deep, ingrained understanding of light reflection in the human brain.

Figure 6: Three examples of human intuition about light propagation.

mechanics can be used to show that GO predictions are the dominant or first-order propagation effects in an asymptotic expansion, with error associated with the neglected terms in the expansion. Even if this error is acceptable in a particular application, simple implementations of ray-tracing through refractive gradients also inherently suffer from a variety of problems, including caustics, problems at turning points, unphysical perfect shadow regions, discontinuous fields, and no capability for handling diffraction from surfaces. These undesirable properties of GO solutions stem from the fact that GO is an approximation of EM fields of infinite frequency, something that is rather unphysical.

Each of these problems can be overcome with extensions to the GO approximation by appealing to the true physics from the wave equations and forcing the ray solutions to have the correct form at places where the ray-approximation breaks down. For example, at turning points or caustics, where rays change directions with respect to a preferred axis or focus to a point, the full-wave solution is used to derive the form of a ray solution that continues through the problematic point. Doing this shows that some additional phase shift is introduced to the ray, but GO theory itself does not predict this effect. Ray-based

models must be augmented with full-wave results in ad-hoc and heuristic ways to give more accurate results or to work at all.

Another example of extensions to GO are the geometrical/unified theories of diffraction (GTD/UTD), which provide a method by which diffraction can be modeled in GO [84, 85]. If a ray strikes a surface, in GO the ray reflects off the surface and transmits through the surface with refraction. However, it is known that EM waves excite currents in the materials they strike, and that these currents re-radiate fields, which is the mechanism by which scattering and diffraction occurs. The GTD/UTD approach is to use analytical full-wave solutions for some canonical geometries to account for diffraction around these structures in a ray approximation. The pure ray-based field calculations are augmented with an appropriate asymptotic solution to the full-wave problem. Each canonical shape then has a diffraction coefficient that can be interpreted as the magnitude and phase of a fan of rays that is emanated from the shape for a given ray incidence angle. These new rays can then continue to be traced to calculate further fields.

The inherent limitations of GO methods can often be overcome, but the combination of pure GO, full-wave corrections, and additional considerations for diffraction motivate the use of alternatives to ray-based methods in this dissertation. The aforementioned extensions to GO can give good results, but the heuristic collection of techniques used to achieve acceptable results makes this approach undesirable from a firm theoretical perspective. While GO methods are conceptually very simple and match much of our intuition about propagation, they are mathematically very complex and inelegant.

1.5.3 Revisiting an Old Approach: Sommerfeld Integrals

In Section 1.2, it was stated that the earliest method for tackling the Sommerfeld problem was the spectral domain approach used by Sommerfeld himself. In those days, the best that could be done was extraction of asymptotic results from the oscillatory integrals that resulted from the technique. Furthermore, the types of problems considered were very simple geometries of either two half-spaces or just a few layers. This was likely because of

the difficulty in calculating the integrands for increasing numbers of layers. Although these integrands can always be written in closed form, doing so becomes increasingly complex, requiring the solution of a large system of linear equations for a given geometry. For example, for a structure of 10 layers bounded by half-spaces containing a vertical electric or horizontal magnetic dipole, the closed form solution for the integrands involves solving a system of 22 equations in 22 unknowns. Aside from being a tedious calculation, the written expression of any one of the resulting 22 functions can take up pages. The solutions of this system of equations would then have to be analyzed in the complex plane in order to determine the asymptotic contributions, something that was intractable in the time of Sommerfeld, and indeed, is still so today for hand calculations.

With the advent of computers, however, numerically solving a 22 by 22 linear system became tractable. In practice at the time of writing, having enough memory to hold the matrices is the limiting factor: if the matrix can be stored in memory, it can likely be inverted in under a few seconds in the worst case. While the tedium of the calculation is not necessarily *lessened* by a computer, the computational time is; this tedium is taken up by circuits in silicon performing billions of operations per second. And in fact, the software algorithms specially designed for solving linear systems have been highly optimized over the years, using clever tricks that people would not think to use when solving such problems by hand. This makes formulating problems of thousand or tens of thousands of layers possible in a way that was inconceivable in the pre-computer era.

Given that this problem can be efficiently solved in the spectral domain using standard numerical linear algebra methods, the remaining part of calculating a solution is an integration step from the spectral domain back to the spatial one. This kind of inverse-Fourier transform integral is called a Sommerfeld integral (SI) when applied to electromagnetics problems. As previously mentioned, this step was historically handled through asymptotic approximations that extracted dominant terms in certain limits. However, more direct quadrature methods are available today to numerically calculate the relevant integrals. It

appears that an SI quadrature model has not been previously implemented for RF propagation, making these studies a unique contribution to the understanding of RF propagation in refractive gradients. It seems that the popularity of the PE and ray-based models in recent decades has superseded the more exact formulation of using spectral methods and SIs. No one has apparently revisited this method for long range RF propagation with the numerical and computer advances of the last fifty years. The popularity, ease of implementation, and acceptable results of GO and PE models are likely the reason that rigorous SI methods have not been considered for long-range radio propagation applications.

It is worth mentioning that while SI techniques *have* found widespread use in multilayered printed circuit board (PCB) simulations for RF trace and antenna characterization and design, these are of a different scale than what is of concern in long range RF propagation. A typical PCB consists of a multilayered structure that is a fraction of a wavelength thick and perhaps tens of wavelengths in transverse dimensions at typical RF frequencies. The far fields of concern are somewhere away from the PCB, outside of the layered structure, typically in the direction normal to the interfaces (e.g. a planar antenna on a PCB radiates normally to it's surface). In contrast, in a typical RF propagation problem, it might be desired to calculate the fields thousands of wavelengths away from the sources *inside* the layered structure representing the ground and atmosphere. It therefore is the case that software algorithms that were designed and fine-tuned to calculate SIs for PCBs are unsuitable to the long range RF propagation problem in refractive gradients. Figure 7 illustrates the differences in these two cases.

There are also wave propagation communities outside of electromagnetics that have studied and implemented the Sommerfeld integral approach for long range propagation. Both acoustic and seismic wave propagation is governed by the same wave equation that governs EM propagation. The speed of sound under the ocean or in the earth's crust also varies with depth below the ocean or earth surface, analogous to how the index-of-refraction of air varies with height above the earth surface. The mathematical descriptions of these

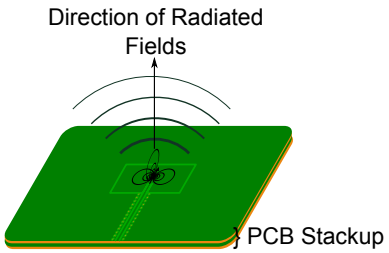

(a) A representation of a PCB patch antenna radiating. The currents are confined to the thin layers of metal material, parallel to the layered structure. The radiated fields of interest are outside of and orthogonal to the layered structure.

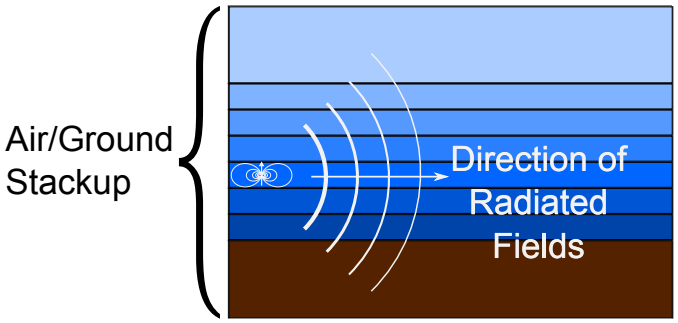

(b) A source radiates inside a layered structure representing the earth and ground. Unlike the PCB case, the fields far away, normal to the interfaces are of no interest in this problem. The direction of interest is parallel to and inside the layered structure.

Figure 7: Two figures illustrate the scale and geometrical differences between PCB scenarios and outdoor long range propagation in a multilayered air/ground model.

three disparate problems can be formulated in an identical way. In the ocean acoustics community, Sommerfeld integral methods are known alternatively as wavenumber integration or fast-field programs, while in seismology they are called reflectivity or discrete wavenumber methods [86]. An SI method for ocean acoustics has been published in a software package known as OASES, which is an enhanced version of an earlier code called SAFARI [87, 88]. The ideas behind SAFARI and OASES, particularly the matrix solution in the spectral domain, are a major inspiration to the method to be presented in Chapter 2.

1.6 Dissertation Outline

The purpose of this introduction has been to give a historical perspective of the study of radio propagation, motivate continued study with emerging applications that require consideration of new phenomena, and make the case that the standard modeling techniques available for RF problems may be unsuitable to the emerging near-earth domain. The methods used in this dissertation will center around the SI, and the following summarizes how this will be elaborated upon in the remaining chapters:

Chapter 2 is a mathematical description of SIs for near-earth RF propagation problems,

along with an examination of the correctness of the implementation that has been developed as part of this dissertation. The SI code that has been developed is compared against other solutions, including analytical forms for some canonical scenarios.

Chapter 3 is a set of comparisons of the presented SI model against a measured RF data set that was collected as part of previous work. The fluid-dynamics theory required to model the atmospheric measurements is also presented in detail.

Chapter 4 is a parametric study of long-range RF propagation using the tools developed in Chapter 2. The parameters varied include the frequency, receiver heights and ranges, ground conditions, and the refractive conditions. Qualitative conditions under which refractivity plays a significant role in the near-earth environment are identified and represent a significant contribution to the understanding of these phenomena in the emerging near-earth propagation environment.

Chapter 5 will conclude the dissertation by discussing it's contributions, limitations, and possible future research directions.

CHAPTER 2

SPECTRAL DOMAIN AND SOMMERFELD INTEGRAL METHODS

Chapter Summary: Spectral domain methods for EM propagation in planar stratified media are reviewed. A spectral domain method is presented to calculate the magnetic vector potential of a vertical dipole in a multilayered medium as a model of long-range radio propagation through a stratified atmosphere. The spectral domain Green's function (SDGF) for structures with up to hundreds of thousands of layers is calculated using an efficient matrix formulation, thus enabling simulation of continuously stratified media. A method is described that samples the SDGF, and uses these samples for all subsequent calculations of the Green's function. These methods include pole/residue-extraction using contour quadratures, novel asymptotic Filon-Clenshaw-Curtis (FCC) quadrature to calculate the far-field Green's functions, and direct Clenshaw-Curtis quadrature used for the near-field Green's function. Results of numerical simulations for propagation in free-space and above a flat ground plane are presented and compared to analytical solutions. A case in which a refractive gradient is used to emulate the effects of a curved earth are also presented. **Note:** Portions of this chapter have been presented in a conference paper that has appeared in PIERS2013 [89].

Spectral domain methods result from Fourier transforming a suitable formulation of Maxwell's equations in space. The Fourier-dual of the Cartesian spatial domain is called the *spectral domain* throughout this work. In the spectral domain representation of electromagnetic fields, all fields are decomposed into a wavenumber-spectrum, and each spectral component represents a plane wave. For example, the z component of the magnetic vector potential, A_z, that is emitted by a source at a height z' could be expanded in a spectral

representation as

$$A_z(x, y, z, z') = \int_{-\infty}^{\infty} \int_{-\infty}^{\infty} \tilde{A}_z\left(k_x, k_y, z, z'\right) e^{j(k_x x + k_y y)}\, dk_x\, dk_y\ , \tag{2}$$

where the Cartesian (x, y) coordinates are the Fourier duals to the (k_x, k_y) wavenumbers, and the presence of the tilde serves to distinguish the spectral domain functions from the spatial domain ones. The basis function for the integral transform above is $e^{j(k_x x + k_y y)}$, which is a plane wave propagating in the direction (k_x, k_y). Each such wave in the spectrum is scaled by the spectral domain function $\tilde{A}_z$ and superposed in the above integral. Several example depictions of plane wave basis functions with various wavenumbers are presented in Figure 8.

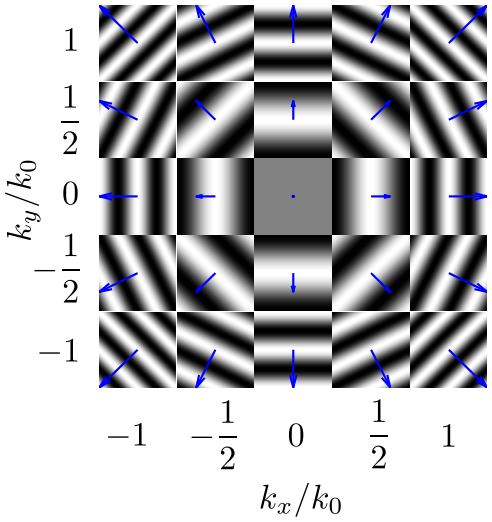

Figure 8: A selection of 2D plane wave basis functions is presented, with various wavevectors. $\Re[e^{j(k_x x + k_y y)}]$ is depicted as a function of (x, y) for various (k_x, k_y). The value $k_0 = 2\pi$.

Inserting representations like Equation 2 into Maxwell's equations result in governing equations for the spectral domain functions that can be simpler than their spatial domain counterparts, depending on the material geometry involved. In planar multilayered media, the spectral domain equations can be reduced to linear ordinary differential equations (ODEs) and ultimately to algebraic equations and solved using methods of linear algebra. An application of this method was presented in a conference paper that was written as a part

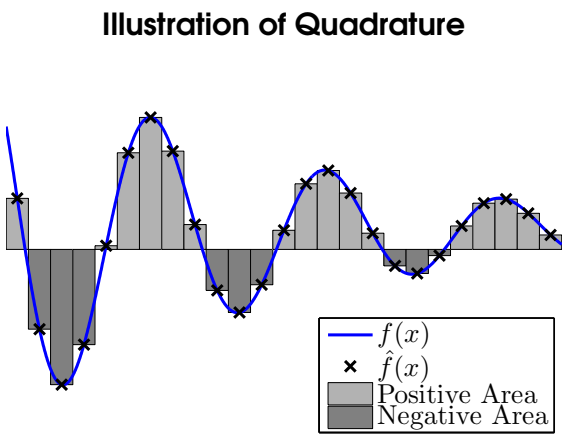

Figure 9: A simple quadrature rule is illustrated. The integrand f is approximated by a piecewise constant function, $\hat{f}$, defined by 25 constant values. The integral of $\hat{f}$ can be calculated by summing the signed-areas of the rectangular regions. The sum approximates the integral of f. As the size of rectangular regions are made smaller and smaller, the approximation is expected to converge to the the integral of f.

of previous work [89]. This chapter expands upon that previous work and describes in detail a complete spectral domain algorithm for calculating all the electromagnetic fields and signal strength of a vertical electric dipole radiating in a multilayered medium as a model of propagation near the surface of the earth in the presence of atmospheric refraction.

Under simplifications in the Fourier integral that are discussed in Appendix B, Equation 2 reduces to a Hankel transform of order zero. It can further be shown that all the electromagnetic fields can be expressed in terms of Hankel transform integrals up to order two (e.g., see Equation 1 of [90]). In electromagnetics, all such Hankel transforms are called *Sommerfeld integrals* (SIs). The exact form is given in the last equation of Appendix B. If the spectral domain function can be solved, then the SIs could be calculated by *numerical quadrature*. Numerical quadrature is the process of calculating integrals by finite-sum approximations. For example, if a function $f(x)$ is approximated by a piecewise constant function $\hat{f}(x)$, then the definite integral of $f(x)$ can be approximated by summing the signed-areas of the rectangular regions comprising $\hat{f}(x)$. Figure 9 illustrates this simple "midpoint-rule" quadrature.

The illustrated midpoint rule is among the simplest of quadratures. It relies on approximating the underlying function $f(x)$ as a piecewise constant function on a uniform (equispaced) grid of x values. On each grid interval, integration becomes a simple closed-form expression (width times height), and the results are summed. A natural extension is to approximate the function by linear interpolation between uniform grid points. When this is done, the rectangles are replaced by trapezoids, resulting in the *trapezoidal* rule. Higher order polynomial representations between equispaced grid points result in the general class of Newton-Cotes quadrature formulas. Still other quadrature approaches interpolate the integrand on a non-uniform grid by a polynomial. Because the integral of a polynomial is another polynomial, methods can be devised to quickly transform the coefficients in a polynomial interpolant of f to those of its integrand.

Quadrature and numerical integration rely on the notion of *convergence*. As more points are sampled from the integrand, and the approximation of the integrand improves, it is expected that the approximation of the original integral also improves. A typical approach for accurate quadrature is to sequentially increase the order of the quadrature and consider the difference between successive results. This difference is a measure of the error between the approximations and the limiting, true value to which the procedure converges. When the difference is small, it can be assumed that successive higher order quadratures will not provide much more accuracy in the final result. The rate at which the error decreases with increasing the quadrature rule order is the *rate-of-convergence* of the rule.

SI expressions for the magnetic vector potential will be calculated using convergent numerical quadratures. In practice, however, implementing efficient numerical schemes for SIs is complicated by a variety of factors that cause quadrature to converge slowly. These include the slow rate of decay of the integrands, singularities in the spectral domain functions, oscillations of the basis function at ranges far away from the sources, and the semi-infinite integration interval. The study of speeding up the convergence of SI quadrature has resulted in a variety of techniques. All the techniques use contours in the complex

plane along which the SI is evaluated. Some use a fixed contour, while others rely on contour deformation to the steepest descent path [91, 92]. Certain choices lead to additional pole and branch cut integral terms, which are also evaluated on a chosen contour in the case of branch cut integrals, and by the residue theorem for pole contributions. Next, an interpolation or extrapolation of the spectral domain function along the various contours is numerically computed. The interpolation/extrapolation basis functions are generally chosen with known SIs in closed form, so the last step is to sum up the contributions from each term in the interpolation or extrapolation. This can be thought of in terms of conventional quadrature, where the interpolation functions are polynomials on a finite domain. However, there are other methods for the SI that involve the use of functions that extrapolate the semi-infinite integral tails using exponential approximations [93, 94, 95, 96, 97] or rational approximations [98, 99]. Another method involves calculating the tail integrals on a sequence of intervals by conventional quadrature, and then applying non-linear series acceleration techniques [90, 100]. The above demonstrates that there is practically unlimited freedom in choosing an approach for these integrals, which has lead to the large variety of published techniques.

In the remainder of this chapter, a particular implementation of spectral domain methods and Sommerfeld integral quadrature is presented for the calculation of the fields of a vertical dipole. The problem geometry, mathematical formulation, spectral domain solution, and SI quadrature implementation are discussed in detail. The results for some simplified geometries are compared against known analytical solutions to demonstrate the correctness of the technique.

2.1 Problem Geometry and Mathematical Model

Spectral domain methods are general enough to calculate fields emitted from arbitrary current distributions inside multilayered media. In the general time-harmonic formulation,

four unique scalar potential functions are emitted from three orthogonal orientations of impulsive current densities [101, 102]. All four potential functions are calculated together so that the response of the medium to any arbitrarily oriented impulsive current density can be calculated. However, if all current densities are oriented orthogonally to the ground surface in a vertical orientation, only one component of the potentials is required to calculate all time-harmonic electromagnetic fields [25]. This simplification is used throughout this work. Handling the other three potential components in a general formulation requires additional calculations that are very similar to those presented here. The methods and algorithms developed for the present special case will be adapted to the general case as part of future studies.

As an approximation of the physical geometry of long range, narrowband RF propagation in refractive conditions, the atmosphere and ground are modeled by a planar-stratified medium that consists of layers of homogeneous, isotropic, nonmagnetic, linear materials. All field quantities are assumed to vary sinusoidally in time with radian frequency ω, with $e^{-j\omega t}$ time dependence. General time-dependence can be considered a superposition of time-harmonic frequency components, so studying the time-harmonic case suffices to characterize the propagation environment. The time-harmonic factor $e^{-j\omega t}$ mathematically cancels everywhere in the equations because it appears on both sides of all the relevant field equations; as such, its notation will be suppressed throughout.

A depiction of the aforementioned planar-stratified geometry appears in Figure 10. The interfaces where adjacent media meet are parallel planes, each orthogonal to the Cartesian z direction. The electromagnetic characteristics of each homogeneous material layer are specified uniquely by its complex dielectric constant, or equivalently, it's index of refraction. Each layer is homogeneous with index of refraction $n_\ell = \sqrt{\varepsilon_0 \varepsilon_{r\ell}}$, where $\varepsilon_{r\ell}$ is the relative permittivity of the ℓ^{th} medium and $\varepsilon_0 \approx 8.85418782 \times 10^{-12}$ F/m is the permittivity of free space. Each layer has an associated wavenumber, $k_\ell = n_\ell k_0$, where $k_0 = 2\pi f / c_0$, f is the frequency of the wave, and $c_0 = 299,792,458$ m/s is the speed of light in vacuum. The

wavenumber in a layer is the wavenumber of a plane wave solution that would propagate in an infinite homogeneous extension of that layer. The top and bottom layers are semi-infinite half-spaces, extending to $z = +\infty$ and $z = -\infty$, respectively. The bottom half-space representing the ground is a lossy dielectric with a finite conductivity, while layers representing the air will be lossless dielectric materials, with dielectric constants representing refractivity gradients of the type discussed in Section 1.4.

The medium contains an impressed, spatially impulsive, z-oriented current density in one of the layers. It is located at height of z' over the origin. More general current densities can be handled by the superposition principle, and so this is a Green's function problem. An impulsive current density in space also approximates a short dipole, so considering this particular Green's function directly will give insight into how short vertical wire antennas perform in refractive conditions. Therefore, the term "dipole" will be used interchangeably with "impulsive current density" throughout this chapter.

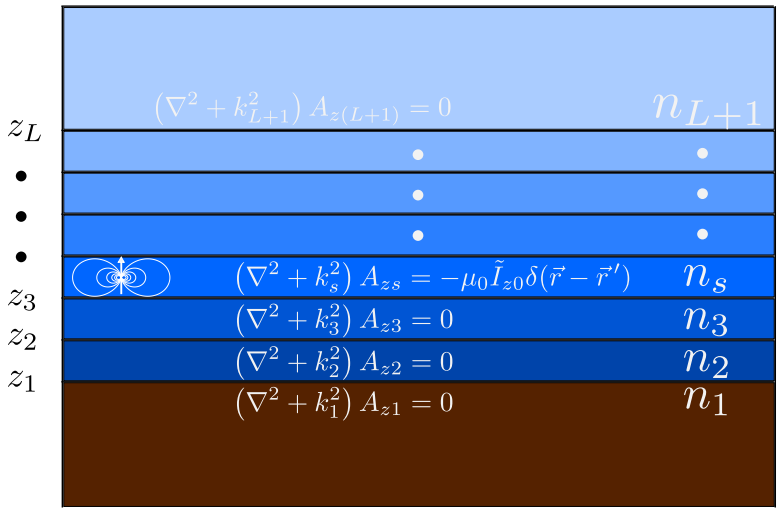

Figure 10: A dipole radiates inside layers of dielectric material. There are L layer interfaces, and $L + 1$ layers including the top and bottom semi-infinite half-spaces.

The EM fields in the geometry of Figure 10 can be expressed in terms of only the z-component of the magnetic vector potential, $A_z(\rho, z, z')$, where ρ is the xy-distance away from the dipole and z is the height above the origin at which the potential is being calculated. Under the Lorenz gauge condition, the potential A_z obeys a forced wave-equation

in the source layer, where the forcing comes from the dipole term. The derivation of the Helmholtz equation for the magnetic vector potential from Maxwell's equations is detailed in Appendix A for completeness. In other layers, the wave equation is unforced because there are no impressed currents within the layers. Under harmonic time dependence, the wave operator reduces to the Helmholtz operator, $(\nabla^2 + k_\ell^2)$, thus Maxwell's equations reduce to a system of coupled Helmholtz equations in this geometry, all of which is also indicated in Figure 10. The coupling between equations is not directly apparent in Figure 10 because the equations are valid inside each homogeneous volume. At the interfaces between media, however, there must be some appropriate continuity conditions that couple the solutions together.

2.2 Spectral Domain Formulation

Performing a Fourier transform in (x, y) on the equations of Figure 10 causes quantities to transform according to

$$\begin{aligned} A_{z\ell} &\overset{\mathcal{F}_{x,y}}{\Rightarrow} \tilde{A}_{z\ell} \\ (x, y) &\overset{\mathcal{F}_{x,y}}{\Rightarrow} (k_x, k_y) \\ (\nabla^2 + k_\ell^2) &\overset{\mathcal{F}_{x,y}}{\Rightarrow} \tfrac{\partial^2}{\partial z^2} + k_{z\ell}^2 \\ k_{z\ell}^2 = k_\ell^2 - k_\rho^2 \quad &, \quad k_\rho^2 = k_x^2 + k_y^2. \end{aligned}$$

Of particular note is that this transformation reduces the three dimensional Helmholtz PDE into a one dimensional ordinary differential equation (ODE). Applying the transformation to Figure 10 results in a system of ODEs in the spectral domain, expressed as

$$\frac{\partial^2 \tilde{A}_{z\ell}}{\partial z^2} + k_{z\ell}^2 \tilde{A}_{z\ell} = \begin{cases} -\mu_0 \tilde{I}_{z0} \frac{\delta(z-z')}{4\pi^2}, & \text{in source layer} \\ 0, & \text{in other layers,} \end{cases} \qquad \text{for } \ell = \{1, 2, \ldots L+1\}, \tag{3}$$

where $\tilde{I}_{z0}$ is the complex magnitude of the current flowing in the dipole, $\mu_0 = 4\pi \times 10^{-7}$ H/m is the permeability of free space, and in each layer the z wavenumber is given by the auxiliary relationship $k_{z\ell} = \sqrt{k_\ell^2 - k_\rho^2}$.

Equation 3 is to be solved in all layers simultaneously for a given k_ρ. In the source layer, this is a standard Green's function problem. In the other layers, it is an eigenfunction

problem. In either case, it can be solved by standard methods for ODEs involving complementary and particular solutions. The complementary solutions that exist in the absence of forcing are the eigenfunctions, and consist of linear combinations of $e^{\pm jk_{z\ell}z}$, which are upgoing and downgoing waves in one dimension. The particular solution is a piecewise combination of these that has a derivative discontinuity such that a delta function results from taking two derivatives. The general solution can be shown to be given by

$$\tilde{A}_{z\ell} = j\frac{\mu_0 \tilde{I}_{z0}}{8\pi^2} \times \begin{cases} \frac{e^{jk_{z\ell}|z-z'|}}{k_{z\ell}} + R_\ell^+ e^{jk_{z\ell}(z-z_{\ell-1})} + R_\ell^- e^{-jk_{z\ell}(z-z_\ell)}, & \text{in source layer} \\ \\ R_\ell^+ e^{jk_{z\ell}(z-z_{\ell-1})} + R_\ell^- e^{-jk_{z\ell}(z-z_\ell)}, & \text{in other layers,} \end{cases} \tag{4}$$

where $R_\ell^\pm$ are unknown coefficients in each layer that represent the magnitude of upward and downward propagating waves in the potential. These have the interpretation of being *generalized reflection coefficients* that account for the net effect of all reflections and refractions from below (for R_ℓ^+), or above (for R_ℓ^-). The unknown coefficients $R_\ell^\pm$ have to be fixed by boundary conditions, which are that the tangential EM fields have to be continuous at the layer interfaces, and that there are no incoming waves ($R_1^+ = R_{L+1}^- = 0$, which is a consequence of physical causality made rigorous by the Sommerfeld radiation condition [103]). Applying these to Equation 4 reduces the problem to a linear system of equations for the $R_\ell^\pm$ coefficients, which is explored in detail in the next section.

2.3 Boundary Conditions at the Interfaces

The solution in Equation 4 is a piecewise combination of one dimensional waves in z, with different rates of spatial oscillation in each layer, plus a term with a derivative discontinuity in it. In order to understand how to perform this piecewise combination of waves, the boundary conditions at the layer interfaces must be determined. For lossy, nonmagnetic dielectric materials with finite conductivity, the integral forms of Maxwell's equations can be used to derive that electric and magnetic fields that are tangential to a material interface must be continuous across it; [104] contains the detailed calculations. The electromagnetic

fields can be written entirely in terms of spatial derivatives of the potentials, as given in Appendix A. Tangential continuity of the electromagnetic fields leads to

$$\left(\tilde{A}_{z\ell} = \tilde{A}_{z(\ell+1)}\right)_{z=z_\ell} \tag{5}$$

$$\left(\frac{1}{n_\ell^2}\frac{\partial \tilde{A}_{z\ell}}{\partial z} = \frac{1}{n_{\ell+1}^2}\frac{\partial \tilde{A}_{z(\ell+1)}}{\partial z}\right)_{z=z_\ell}, \tag{6}$$

which express that the vector potential and a scaling of its normal derivative is continuous at every layer interface. Equation 5 expresses the electric field continuity, and Equation 6 expresses the magnetic field continuity. Inserting the solution from Equation 4 into Equations 5 and 6 results in a system of $2L$ linear *algebraic* equations for the unknowns $R_\ell^\pm$. In general there are two unknowns per layer in the structure, which would result in $2L+2$ unknowns. However, by the Sommerfeld radiation condition, sources should produce fields that radiate to infinity [103]. This precludes any downward propagation in the upper half-space and and upward propagation in the lower half-space. This can be enforced by setting the coefficients that correspond to these waves to zero, $R_1^+ = R_{L+1}^- = 0$. Doing so reduces the total number of unknowns by 2, resulting in a system of $2L$ linear equations for $2L$ unknown coefficients.

2.4 The Spectral Domain Solution

Solving the system represented by Equations 4, 5, and 6 is possible symbolically by hand or using a computer algebra system. However, the resulting solutions become longer in proportion to the number of layers, becoming intractable for more than 2 or 3 layers. The solution to Equations 4, 5, and 6 admit relatively compact expressions in terms of recursive formulas and products of series, which are the most popular approach for numerical calculations of the generalized reflection coefficients in electromagnetic problems [101, 105, 106]. These recursive formulas prescribe a particular algorithm by which a linear system of equations is to be solved. In the most general form, however, the system of linear equations is simply represented by a $Mu = b$, where M is a matrix, u is a vector

of unknown coefficients, and b is a vector of forcing terms. This general system can be solved by any of a number of standard numerical algorithms. This is favorable compared to recursive formulas, which can have problems of numerical stability when converted to a finite precision numerical implementation; Section 4.3 of [86] gives a good overview of these problems.

The approach taken in this work has been to form the system represented by Equations 4, 5, and 6 into a matrix directly, and use existing, well established linear system solvers. Because the MATLAB computing package has been used throughout this work, the details of the implementation of the matrix solution are generally hidden from the user. However, MATLAB can be made to expose these implementation details. For the type of matrix that results from this system, the LAPACK banded routines are used to solve this system, which use an optimized version of the LU decomposition [107]. The LU decomposition algorithm of a matrix is known to have numerical instability problems for general matrices; however, the LU decomposition algorithm *is* numerically stable for the class of diagonally dominant matrices. If the matrix entries can be rescaled and and columns reordered to bring the matrix to a form that is diagonally dominant, then numerical stability is ensured [108, 86]. However, column reordering and matrix rescaling for stability are handled automatically by the "expert" LU routines available in LAPACK [107], and so no further processing is done to the system of equations before solving.

2.4.1 Spectral Domain Solution Example in Five Layers

The method of solving Equations 4, 5, and 6 is illustrated in Figure 11. The example is calculated in a structure with five layers. In each layer, the solution takes the form given in Equation 4, i.e., the sum of two complex exponentials in the variable z with different rates of spatial oscillation given by $k_{z\ell}$. An overall normalization factor of $j\frac{\mu_0 \tilde{I}_{z0}}{8\pi^2}$ is suppressed in each layer. At each layer interface, Equations 5 and 6 are enforced, which is depicted to the far right of the right panel. Each equation at an interface involves only the unknown $R_\ell^\pm$ values from adjacent layers, meaning that each equation couples together four unknowns

at most. The equations at z_1 and z_4 only couple together three unknowns, since the solutions in the top and bottom layers have been modified to exclude downward and upward propagation, respectively, to enforce the Sommerfeld radiation condition. If the equations and unknowns are ordered as depicted, a sparse pentadiagonal matrix results. The entries of the matrix are functions of the material indices of refraction, n_ℓ, the interface heights, z_ℓ, and the parameter k_ρ. Note that Equation 4 indicates that one of the layers should contain an additional forcing term due to an impressed dipole source. However, this term does not depend on the unknown $R_\ell^\pm$ values, and so is not depicted in the figure. This forcing term only appears as the right-hand-side in the linear system of equations $Mu = b$, where the sparse matrix depicted in Figure 11 is denoted as M and the unknowns are denoted as $u = (R_1^-, R_2^+, R_2^-, R_3^+, R_3^-, R_4^+, R_4^-, R_5^+)^T$. The quantity b is also sparse, and only includes four non-zero entries. The nonzero entries only occur in the equations at interfaces adjacent to the source dipole, and derive from the spectral domain forcing term, $e^{jk_{z\ell}|z-z'|}/k_{z\ell}$, as given previously in Equation 4.

The system of equations of Figure 11 is for the specific case of the spectral domain solution in a five layer medium. However, the software implementation of the algorithm is capable of constructing and solving the spectral domain matrix for an arbitrary number of layers. All the parameters that enter in the calculation are uniquely specified by the layer indices of refraction and layer thicknesses, except for the wavenumber k_ρ. Once the value of k_ρ is fixed, then the spectral domain matrix solution is a purely numerical task that is calculated in finite precision using the aforementioned LAPACK routines. The solution for the unknown generalized reflection coefficients can then be seen to be a function of the wavenumber k_ρ: for each numerical value of k_ρ, the proposed matrix-based algorithm can calculate all the generalized reflection coefficients in all layers.

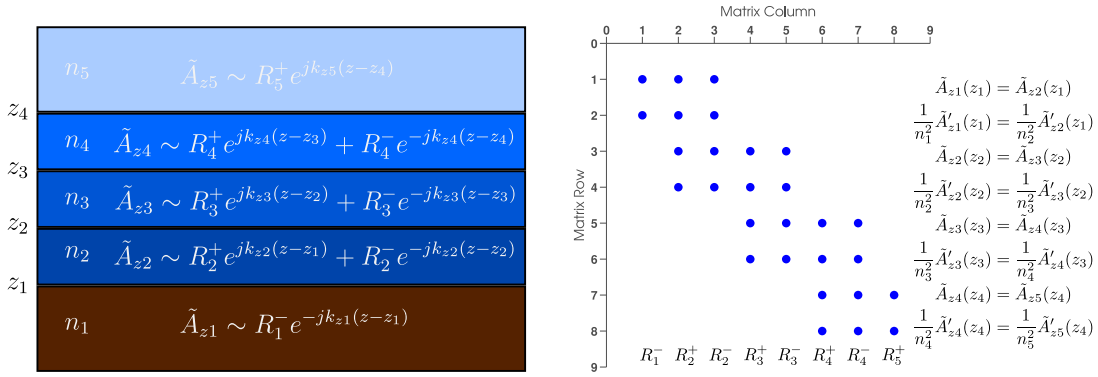

(a) The spectral domain solution in a five-layer structure.

(b) Illustration of the spectral domain matrix sparsity pattern.

Figure 11: The spectral domain matrix solution is illustrated. The left panel depicts a multilayer medium with five distinct layers. Each layer has an associated index of refraction, denoted n_ℓ with $\ell \in \{1, 2, 3, 4, 5\}$. The heights of the interfaces between the layers are denoted by z_ℓ with $\ell \in \{1, 2, 3, 4\}$. In each layer, the spectral domain solution is presented in terms of the unknown variables $u = (R_1^-, R_2^+, R_2^-, R_3^+, R_3^-, R_4^+, R_4^-, R_5^+)^T$. Enforcement of the boundary conditions of Equations 5 and 6 at each layer interface leads to a sparse system of equations for the unknown variables, which is depicted in the right panel. The equations at each interface appear along the right of the panel, and the unknowns involved in the equations appear along the bottom. A dot in a row and column indicates that the corresponding unknown quantity at the bottom appears in the corresponding equation at the right. Spaces with no dots represent zero entries in the matrix.

2.5 Integration of the Spectral Domain Solution: The Sommerfeld Integral

Using the matrix solution of Section 2.4, the spectral domain potential functions $\tilde{A}_{z\ell}$ can be found for all ℓ values in the structure, for a fixed value of k_ρ. Let the function $\tilde{A}_z(k_\rho, z, z')$ be the following piecewise combination of the $\tilde{A}_{z\ell}$ functions that are valid in each layer.

$$\tilde{A}_z(k_\rho, z, z') = \begin{cases} \tilde{A}_{z1}(k_\rho, z, z'), & z < z_1 \\ \tilde{A}_{z2}(k_\rho, z, z'), & z_1 < z < z_2 \\ \vdots & \\ \tilde{A}_{zL}(k_\rho, z, z'), & z_{L-1} < z < z_L \\ \tilde{A}_{z(L+1)}(k_\rho, z, z'), & z > z_L \end{cases} \tag{7}$$

The function $\tilde{A}_z(k_\rho, z, z')$ is known as the *spectral domain Green's function* (SDGF) for the z-component of the magnetic vector potential due to a z-directed current density. It represents the response of a multilayered medium to the spectrum of plane waves generated by a z-directed current density in the medium. For any plane wave component identified by the wavenumber k_ρ, $\tilde{A}_z(k_\rho, z, z')$ can be calculated numerically using the procedure outlined in Section 2.4. To transform back to the spatial domain, an integral over the plane waves present in the spectrum of the dipole potential needs to be calculated. Recalling that $k_\rho^2 = k_x^2 + k_y^2$ and noting that the SDGF only depends on k_x and k_y through this quantity, the double integral over the spectrum reduces to a single integral given by

$$A_z(\rho, z, z') = 2\pi \int_0^\infty \tilde{A}_z\left(k_\rho, z, z'\right) J_0(k_\rho \rho) k_\rho \, dk_\rho, \tag{8}$$

where J_0 is the Bessel function of the first kind and order zero. See Appendix B for a detailed derivation. This expression is known as the *Sommerfeld integral* (SI) representation of the magnetic vector potential Green's function for the geometry of Figure 10. Equation 8 can, in principle, be approximated numerically by sampling the SDGF on a discrete set of k_ρ values, and then approximating the integral by quadrature on the sampled values. Each sample of the SDGF would involve setting up and solving the spectral domain matrix

equation of Section 2.4. However, calculating SIs by numerical quadrature is practically complicated by factors including 1) the oscillatory nature of the Bessel function, 2) the semi-infinite interval of the integration, 3) the slow decay characteristics of the integrand, and 4) singularities in the integrand including poles and branch cuts. Each of these leads to a slow convergence of the numerical quadratures involved. If these factors can be eliminated, minimized, or accounted for, then computer algorithms can calculate the integrals more efficiently and quickly.

2.5.1 Poles and Guided Modes

The singularities in the integrand play a very important role in the convergence of the quadrature routines, and also have important physical interpretations. Any singular behavior of the integrand of Equation 8 must come from the spectral domain Green's function, because the other terms are analytic in the entire complex plane. The procedure for determining $\tilde{A}_z$ involved the solution of a system of linear equations by matrix methods, which can of course be singular or non-invertible in general. The matrix itself can be shown to only depend on the material properties, geometry and the wavenumber, and not on the source or field positions (ρ, z, z'). Therefore, the wavenumbers at which singularities appear in the spectral domain matrix solution are a property of the layer structure only; they are characteristic wavenumbers for the structure in the spectral domain. The SDGF grows without bound in the vicinity of these singular wavenumbers in the form of a pole singularity. These singularities appear in opposing pairs, $\pm k_{\mathrm{p}}$, in multilayered SI problems [102].

Spectral domain poles translate to the spatial domain in the following way. The spectral domain representation of a pair of poles that would appear in an SDGF in practice is

$$\tilde{A}_{z\mathrm{p}}\left(k_\rho, z, z'\right) = \frac{f(z, z')}{k_\rho^2 - k_{\mathrm{p}}^2}. \tag{9}$$

The poles all have the same k_ρ dependence, but the "strength" of the pole will depend on the evaluation and source heights, (z, z'). Plugging this pole function into the SI of Equation

8 transforms the pole from the spectral domain to the spatial domain,

$$2\pi \int_0^\infty \frac{f(z,z')}{k_\rho^2 - k_\mathrm{p}^2} J_0\left(k_\rho \rho\right) k_\rho \, dk_\rho = j\pi^2 f(z,z') H_0^{(1)}(k_p \rho), \tag{10}$$

where $H_0^{(1)}$ is the Hankel function of the first kind and order zero. The physical significance of this is that poles in the SDGF contribute waves in the spatial domain that have a special form. Firstly, the fields vary in range (ρ) according to a Hankel function, which has the physical interpretation of being an outward propagating cylindrical wave. Secondly, the height and range dependencies are decoupled; therefore a cylindrical wave of the same form propagates outwards from the z-axis with a different amplitude and phase that only depends on the source and field heights. This has all the hallmarks of a *guided mode* in a waveguide. Waveguiding is a property physically expected of a refractive structure, and this development puts that expectation on a firm theoretical basis. In the language of spectral theory, the pole wavenumbers are eigenvalues of the structure, and the eigenfunctions are the mode functions with the form given by Equation 10.

2.5.2 Guided Mode Extraction

Aside from having closed form integrals and a physical interpretation in terms of modal propagation, poles in the SDGF contribute to slow decay of the integrand. As a function of k_ρ, a pole term decays as $O\left(\frac{1}{k_\rho}\right)$. Aside from any possible convergence issues, integrating functions with such a decay rate by numerical quadrature also takes relatively longer than if the decay were faster. The approach in this dissertation is to extract the poles from the SDGF and integrate them analytically according to Equation 10. First, the poles must be located, which can be done with numerical search algorithms in the complex plane. An effective search algorithm based on complex contour integrals, which automatically finds the pole wavenumbers and residues, has been described in the literature [91, 109]. In the present implementation, the poles are located by refining user-provided initial guesses with a direct search optimization. Secondly, the residues at the poles must be calculated. These are the numbers that dictate the "strength" of a pole, indicated by $f(z,z')$ in Equation

9. The current implementation to extract these is an application of the residue theorem using quadrature to approximate continuous contour integrals. A small polygonal contour is constructed around each pole in the SDGF. The SDGF is sampled along this contour and an adaptive Gauss-Kronrod quadrature, adapted from [110, 111], is applied along the contour until the results converge to 12 digits of precision. The residues at all desired field heights are calculated in parallel by the chosen Gauss-Kronrod algorithm. Knowing the residues of all the extracted poles allows the SDGF to be expanded as a sum of the poles and remainder function as

$$\tilde{A}_z(k_\rho, z, z') = \tilde{A}_{z\text{-np}}(k_\rho, z, z') + \sum_{m=1}^{M} \frac{f_m(z, z')}{k_\rho^2 - k_{\text{p}m}^2}, \tag{11}$$

where there are M poles and the $f_m(z, z')$ are the extracted residues. A visualization of this technique appears in Figure 12. The SDGF has the poles extracted, and the remainder function is seen to be smoother and decay more quickly. The SI of the SDGF is then calculated as the sum of the modal contributions, and numerical quadrature is done only on the smoother remainder function. This speeds convergence and extracts the modal fields.

2.5.3 Oscillations and Asymptotic Quadrature

The standard approach to quadrature of oscillatory integrands is to sample them on enough points to resolve the oscillations and then approximate the integral as a weighted sum of the sampled values. For the present case this would mean that the number of SDGF samples would increase in proportion to the range ρ. Calculation of far-fields would require *more* computational effort than the near-fields. However, there are several families of *asymptotic* quadratures that *increase* in accuracy as the oscillation increases [112, 113]. The method used presently is the Filon-Clenshaw-Curtis (FCC) rule [114, 115]. Although designed for complex exponential oscillation, far-field SIs can be adapted for the FCC in the following way. Since asymptotic results are of interest, the Bessel function is replaced by its asymptotic expansion in Equation 8, giving

$$A_z(\rho, z, z') \approx \sqrt{\frac{1}{2\pi\rho}} \int_0^\infty \tilde{A}_z\left(k_\rho, z, z'\right)\left(e^{jk_\rho\rho - j\frac{\pi}{4}} + e^{-jk_\rho\rho + j\frac{\pi}{4}}\right)\sqrt{k_\rho}\, dk_\rho\ , \tag{12}$$

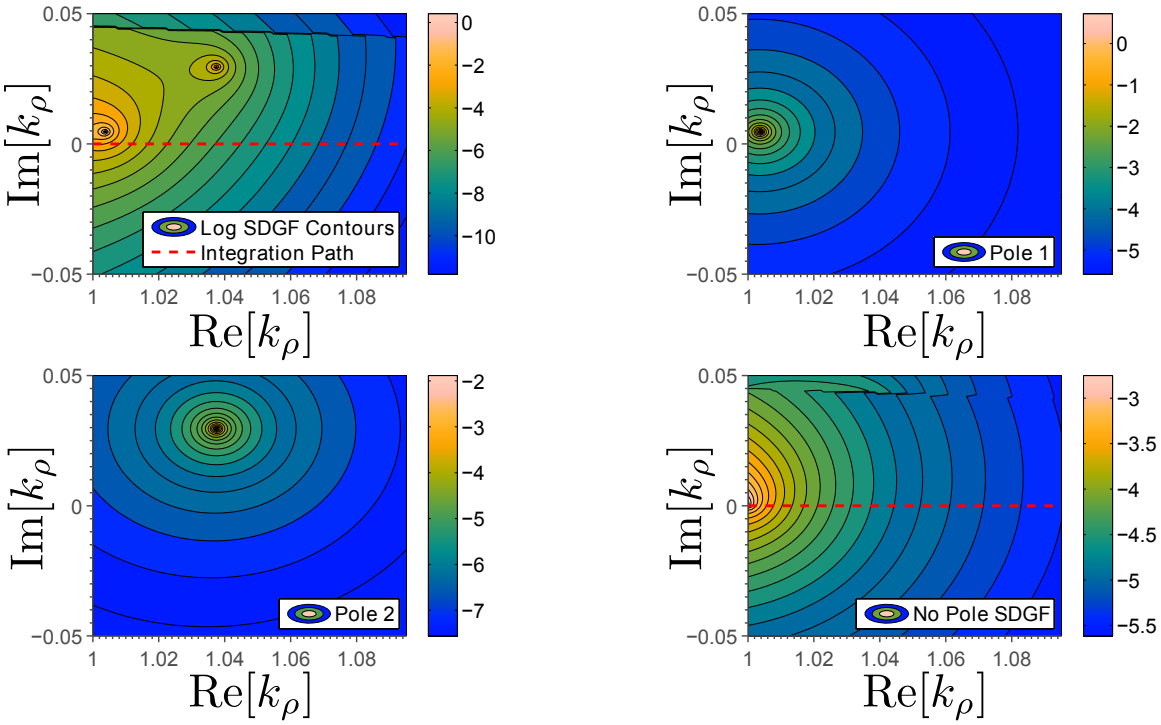

Figure 12: Contours of the logarithm of the magnitude of the SDGF in a propagation scenario are presented in the upper left panel. The two main features are concentric circles around two pole singularities. The upper right and lower left panels present just the numerically extracted poles. The precise locations of the poles are found by maximizing the SDGF, and the strength of the pole is found by approximating the complex residues by contour quadrature around the poles. The lower right panel shows the result of subtracting these two pole contributions from the original SDGF. The result is a smoother and faster decaying function along the original integration contour.

which can be broken up into two integrals, each of which has a form that is directly amenable to FCC quadrature after the semi-infinite interval is truncated to a large finite value. Finite truncation is justified physically because the pole-extracted SDGF decays exponentially beyond the largest material wavenumber and the rapid spatial oscillations of large wavenumbers are known to contribute only to the near-field singularity; the corresponding waves do not propagate into the far-field.

2.6 The Full Quadrature Algorithm

Sections 2.5.2 and 2.5.3 describe methods to overcome two of the complicating factors in numerically integrating the SI for the magnetic vector potential. The algorithmic implementation of these ideas can now be described as follows. Any time samples of the SDGF are required, they are calculated using the matrix-inversion methodology of Section 2.4. The samples are taken on a finite truncation of the original, infinite interval of Equation 8. The truncated interval is divided into a partition of subintervals, denoted k_v^{int}, for $v = 1, 2, \ldots, V$. On each subinterval, the SDGF is represented as a Chebyshev polynomial-interpolant passing through sample points. The number of points and the order of the polynomial representation is chosen by an automatic adaptive procedure that guarantees that the polynomial interpolant is accurate to near machine-precision using algorithms from the Chebfun package [116]. Once the SDGF at all heights of interest and on all subintervals is approximated by polynomial-interpolants, one of two algorithms is used for quadrature.

In the first algorithm, the Bessel function in the integral of Equation 8 is also approximated to near machine-precision by Chebyshev polynomial-interpolants. Then the product of the Bessel function interpolant and the SDGF interpolant is formed, resulting in a polynomial-interpolant for the integrand of interest. Once the integrand is approximated to near machine-precision by polynomial-interpolants, numerical integration becomes feasible because integrals of polynomials are calculable in closed form. The method of using

Chebyshev polynomial interpolants for numerical integration is known as the Clenshaw-Curtis algorithm, and the Chebfun package provides a fast and numerically stable implementation of the Clenshaw-Curtis algorithm.

The second algorithm does not approximate the Bessel function by a Chebyshev interpolant. Instead, the Bessel function is approximated as the first term in a large-argument asymptotic expansion. The approximation introduces an additional factor of $\sqrt{k_\rho}$ to the integrand, and the Bessel function reduces to a sinusoidal term of the form $\cos(k_\rho\rho)$, as seen in Equation 12. The additional square-root factor is approximated by Chebyshev polynomials, and an approximation to the integrand is again formed. The remaining sinusoidal factor is inherently accounted for by the previously mentioned Filon-Clenshaw-Curtis algorithm, which is designed for integrating products of Chebyshev polynomials and sinusoidal factors. Therefore, only the product of the SDGF and the square-root factor is passed directly into the Filon-Clenshaw-Curtis algorithm. Figure 13 presents the algorithm on one subinterval using a flowchart representation.

2.6.1 Integration Interval Finite Truncation and Subintervals

It was previously mentioned that the present SI quadrature algorithm operates on a finite-truncation of the original integration interval $[0, \infty]$. This infinite interval is approximated by $[0, k_{\max}]$; in other words, the infinite upper limit of integration is replaced by a large finite value. The value of of $k_{\max}$ is a user selectable parameter, and is typically taken to be $k_{\max} = 10k_0$ for the majority of the plots in this work. The finite truncation is justified if the integrand has a relatively small magnitude at $k_{\max}$. Waves with wavenumber larger than the medium wavenumber decay exponentially with distance. Therefore, this *evanescent* spectrum of exponentially decaying waves should contribute very little to the fields far away from the source. The spatial decay rate also increases with increasing wavenumber beyond the medium wavenumber. Since the SI is a superposition of such waves, the evanescent waves that decay fastest (the larger wavenumbers) can reasonably be neglected in the superposition, without causing significant errors in the final integral.

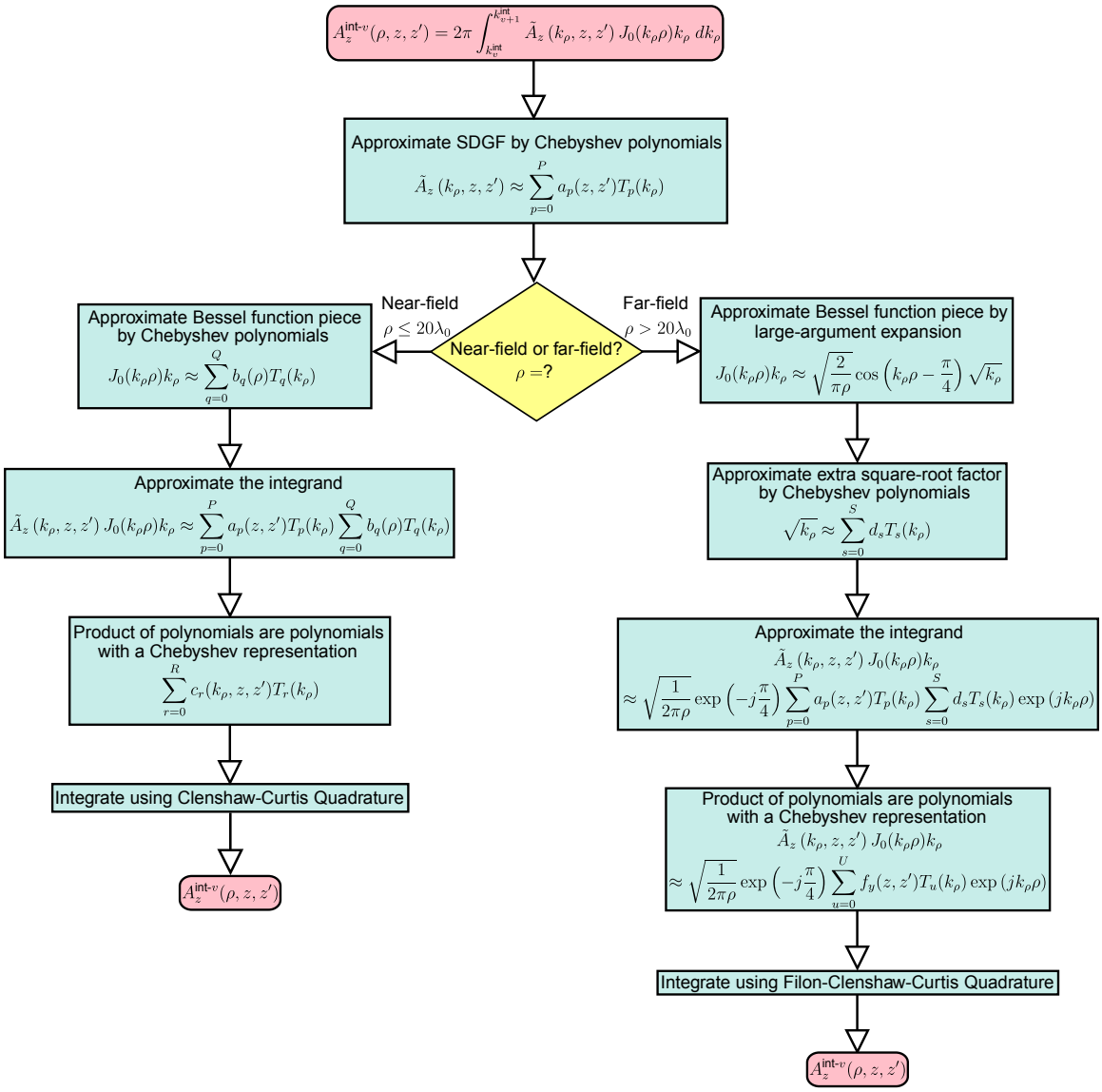

Figure 13: The integration algorithm on a subinterval is presented. For final results, this algorithm is iterated over k_ρ-subinterval number v and the results are summed.

The subinterval boundaries are parameters that can be selected by the user as well. This is primarily done to ensure numerical stability of the Clenshaw-Curtis and Filon-Clenshaw-Curtis algorithms, particularly around branch points. The relationship between the layer wavenumbers $k_{z\ell}$, the radial wavenumber of integration, k_ρ and the layer z-wavenumbers, $k_{z\ell}$ is

$$k_{z\ell} = \sqrt{k_\ell^2 - k_\rho^2}. \tag{13}$$

The above relationship contains a square-root, indicating that $k_{z\ell}$ is not smooth at $k_\rho = k_\ell$ in each layer. In fact, since the square-root is multivalued in general, it is known that there must be a line of discontinuity in $k_{z\ell}$ when considered in the complex-k_ρ plane. This is a branch-cut singularity, which is a curve in the complex plane beginning at the branch-point and continuing on to complex-infinity, along which the square-root function is discontinuous. Since the SDGF $\tilde{A}_{z\ell}$ is a function of k_ρ only through the $k_{z\ell}$ values, then the SDGF is in general discontinuous across these branch cuts. From the above analysis, it would appear that the SDGF would contain branch points at every medium wavenumber $k_{z\ell}$; however, it can be shown that the SDGF is actually only discontinuous along branch-cuts corresponding to the wavenumber for the lower half-space (wavenumber k_1), and to that for the upper half-space (wavenumber k_{L+1}); this is related to enforcement of the radiation condition in those layers, and is briefly discussed in [95]. In the refractive structures studied in this document, the lower half-space is always a lossy medium with a strictly non-real wavenumber. The upper half-space is always a lossless air medium with a purely real wavenumber, i.e., $k_{L+1} \approx k_0$. If the integration interval of interest is the purely real interval $[0, k_{\max}]$, and $k_{\max} >> k_0$ for the reasons given in Section 2.6.1, then it is clear that the integration interval contains the real branch point corresponding to the upper lossless half-space. The branch-cuts in the complex plane and their typical relationship to the integration path is show in Figure 14.

The integration path passes directly through the real branch-point associated with the

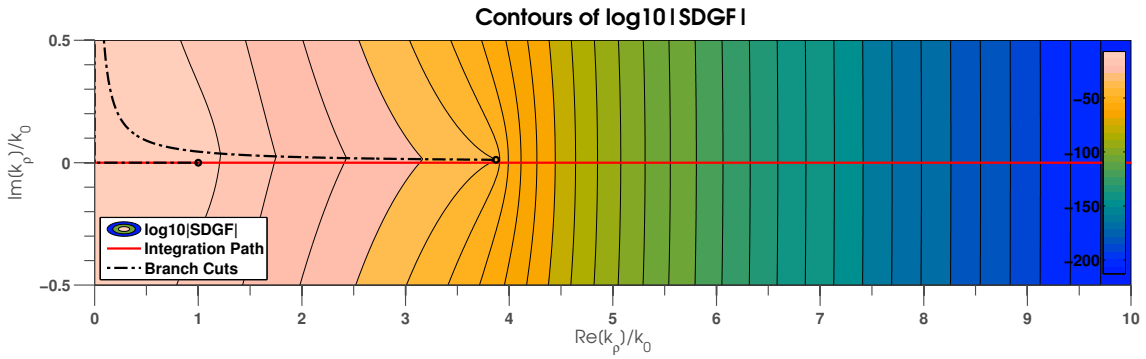

Figure 14: The branch-cut structure of the SDGF is visualized. The branch cuts begin at the complex wavenumbers associated with the ground and uppermost half-spaces. The integration path passes directly through the real branch point associated with the upper air half-space.

upper half-space, where the SDGF is continuous. However, it contains a derivative singularity at this point. The singular derivative is visualized in Figure 15. The Chebyshev inter-

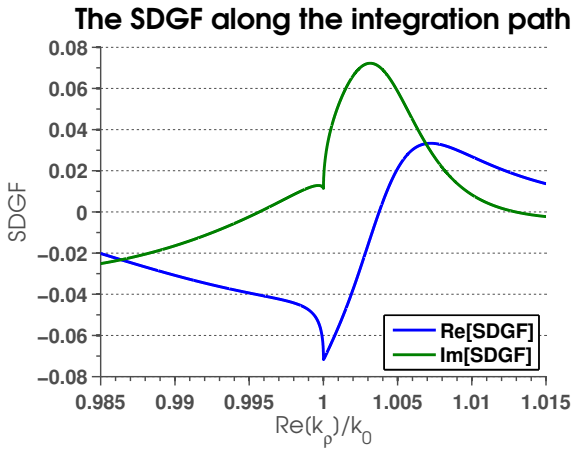

Figure 15: The behavior of the SDGF near the branch-point $k_\rho \approx k_0$ is presented. The real and imaginary parts of the SDGF both are discontinuous in their first derivatives at the branch point, apparent in the "kink" in the curves near $k_\rho \approx k_0$. Furthermore, the real part of the SDGF has a nearly-infinite slope at the branch point, indicating a singularity in the derivative of the SDGF at that point.

polants used have difficulty in representing functions with infinite derivatives. In particular, the order of an accurate Chebyshev interpolant becomes prohibitively large if the approximation interval is long and contains derivative singularities. However, if short intervals are used near the branch-point, then the interpolant only has to represent the singular behavior

at the branch-point, and not any other behavior away from the branch point. Therefore, the problematic branch-point is isolated by very short intervals. A typically used set of subinterval partitions in this work is

$$\left\{k_v^{\text{int}}\right\}_{v=1}^{5} = \{0, k_0, n_{L+1}k_0 - \Delta, n_{L+1}k_0, n_{L+1}k_0 + \Delta, 10k_0\}, \tag{14}$$

where Δ is a small parameter typically taken to be $\Delta = (6\times10^{-6})k_0$. This value was found to minimize the overall polynomial order required to represent the SDGF for a typical propagation simulation. In this scheme, the first subinterval captures the complex amplitude of all the waves that would propagate in free-space, and typically required interpolation at over 2048 points to represent the SDGF to machine precision. The second, third, and fourth subintervals capture the amplitudes of the waves that propagate nearly horizontally, with wavenumbers in the vicinity of the problematic branch-point. A representative number of SDGF evaluations over these intervals is 8192. Finally, the fifth interval captures the amplitudes of the waves that are evanescent and contribute primarily to the near-field singularity at the source. The fifth subinterval typically required 16 to 256 SDGF evaluations. Therefore, the spectral domain solution is carried out over approximately 10000 wavenumbers in total for a typical propagation calculation, and the SDGF is represented by polynomial interpolants between these 10000 sample points. The Chebfun package guarantees that this polynomial is within $\approx 10^{-15}$ of the underlying continuous function.

2.7 Calculating all Fields and Received Power

The algorithms of this chapter calculate the magnetic vector potential of a time-harmonic dipole source embedded in a multilayered medium. However, the magnitude and phase of the magnetic vector potential are not directly useful for practical engineering calculations. In practice, radio engineers, communications link designers, and wireless telecommunications professionals are primarily interested in the average amount of wireless power or signal strength available at a receiver. To provide numerical results of power and signal strength requires additional processing of magnetic vector potential data. Fortunately, all

electromagnetic fields can be calculated from the magnetic vector potential, and the signal strength can be calculated from the fields . This section briefly outlines the method used in this work to finally arrive at physically and practically meaningful quantities.

The broad approach to calculating power is to approximate the differential relationship between the magnetic vector potential and the electromagnetic fields by finite differences. Once the electromagnetic fields are calculated by finite-differences, the time-averaged Poynting vector, which is the power-flux in $\mathrm{W/m^2}$ of the fields, is calculated. Finally, this power-flux is multiplied by a cross-sectional area corresponding to the receiver aperture of an isotropic receiving antenna, giving an answer in real watts of power available at a receiver antenna.

Expressions for the differential relationship between the magnetic vector potential and the electromagnetic fields for time-harmonic excitation are derived in Appendix A. The expressions are

$$\mathbf{H} = \frac{1}{\mu_0}\nabla\times\mathbf{A}, \tag{15}$$

$$\mathbf{E} = -\nabla\varphi + j\omega\mathbf{A}, \tag{16}$$

$$\nabla\cdot\mathbf{A} = j\omega\mu_0\varepsilon_r\varepsilon_0\varphi, \tag{17}$$

where $\mathbf{H}$ is the magnetic field vector, μ_0 is the permeability of free space, $\mathbf{A}$ is the magnetic vector potential, $\mathbf{E}$ is the electric field vector, φ is the scalar electric potential, $\omega = 2\pi f$ is the radian frequency of the time-harmonic excitation, ε_r is the complex dielectric constant of the medium in which the waves are propagating, and ε_0 is the permittivity of free space. Equation 15 is the definition of the magnetic vector potential and Equation 16 is the defining equation for the scalar electric potential. Equation 17 is the Lorenz gauge condition that relates the two potentials to each other. For convenience, we take a cylindrical coordinate system, (ρ, ϕ, z), for all calculations, where ρ is a radial range outwards in the $x-y$ plane, ϕ is an azimuth angle in this plane, and the coordinate z measures orthogonal distances away from this plane. All vector fields will be written in these components, i.e., $\mathbf{H} = (H_\rho, H_\phi, H_z)$

and $\mathbf{E} = (E_\rho, E_\phi, E_z)$.

Rearranging Equation 17 and inserting into Equation 16 results in

$$\mathbf{E} = -\frac{\nabla\nabla\cdot\mathbf{A}}{j\omega\mu_0\varepsilon_r\varepsilon_0} + j\omega\mathbf{A}. \tag{18}$$

Equations 15 and 18 are formulas that allow calculation of the electric and magnetic fields from the magnetic vector potential. Other different but equivalent expressions are often encountered in the literature, and can be derived, e.g., by using the Maxwell-Ampère law to calculate $\mathbf{E}$ from $\mathbf{H}$. However, Equations 15 and 18 will serve as the basis for all field calculations in this work.

In a multilayered medium with an impressed vertical electrical dipole, the magnetic vector potential only has one one nonzero component,

$$\mathbf{A} = (0, 0, A_z(\rho, z)). \tag{19}$$

Note that A_z is also ϕ-invariant. Using these two facts in a direct calculation of the gradient, curl, and divergence operations from Equations 15 and 18 in cylindrical coordinates shows that

$$H_\rho = E_\phi = H_z = 0, \tag{20}$$

and

$$H_\phi = -\frac{1}{\mu_0}\frac{\partial A_z}{\partial\rho}, \tag{21}$$

$$E_\rho = -\frac{1}{j\omega\mu_0\varepsilon_r\varepsilon_0}\frac{\partial}{\partial z}\frac{\partial A_z}{\partial\rho}, \tag{22}$$

$$E_z = -\frac{1}{j\omega\mu_0\varepsilon_r\varepsilon_0}\frac{\partial^2 A_z}{\partial z^2} + j\omega A_z. \tag{23}$$

Power calculation proceeds numerically by first evaluating $A_z(\rho, z)$ on a nine-point grid around all (ρ, z) points where the fields are required. The grid spacing was taken as $\Delta = \lambda_0/200$ in all plots presented in this work. This value was selected purely heuristically as a small value that scales with the wavelength. A simple calculation can show that for waves

with wavelength λ_0, first derivatives calculated by finite differences on a $\Delta = \lambda_0/200$ grid have approximately 6 digits of precision. This grid is depicted in Figure 16.

The derivatives in Equations 21-23 are approximated by finite differences on this grid. The radial derivatives are calculated as

$$\frac{\partial A_z(\rho, z)}{\partial \rho} \approx \frac{A_z(\rho + \Delta, z) - A_z(\rho - \Delta, z)}{2\Delta}. \tag{24}$$

First order and second order z-derivatives are approximated by finite differences using

$$\frac{\partial A_z(\rho, z)}{\partial z} \approx \frac{A_z(\rho, z + \Delta) - A_z(\rho, z - \Delta)}{2\Delta}, \tag{25}$$

$$\frac{\partial^2 A_z(\rho, z)}{\partial z^2} \approx \frac{A_z(\rho, z + \Delta) - 2A_z(\rho, z) + A_z(\rho, z - \Delta)}{\Delta^2}, \tag{26}$$

Finally, the mixed second order derivative ($\frac{\partial}{\partial z}\frac{\partial A_z}{\partial \rho}$) that appears in Equation 22 is calculated in two steps. First, two radial derivatives at the upper and lower z positions on the grid are approximated by

$$\frac{\partial A_z(\rho, z + \Delta)}{\partial \rho} \approx \frac{A_z(\rho + \Delta, z + \Delta) - A_z(\rho - \Delta, z + \Delta)}{2\Delta}, \tag{27}$$

$$\frac{\partial A_z(\rho, z - \Delta)}{\partial \rho} \approx \frac{A_z(\rho + \Delta, z - \Delta) - A_z(\rho - \Delta, z - \Delta)}{2\Delta}. \tag{28}$$

Then the mixed partial is evaluated by again differencing the results, i.e.,

$$\frac{\partial}{\partial z}\frac{\partial A_z}{\partial \rho} \approx \frac{\frac{\partial A_z(\rho, z+\Delta)}{\partial \rho} - \frac{\partial A_z(\rho, z-\Delta)}{\partial \rho}}{2\Delta}. \tag{29}$$

Graphical depictions of the finite differencing grid points used in each calculation appear in Figures 17, 18, and 19.

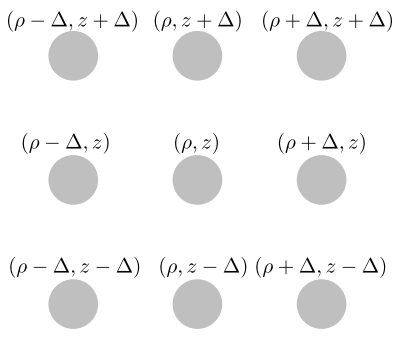

Figure 16: For each field point (ρ, z), A_z is evaluated on a regular grid with spacing Δ.

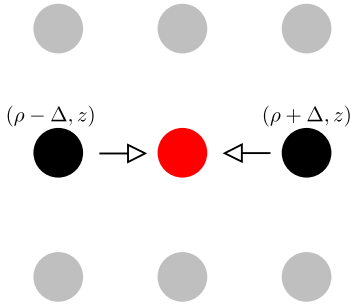

Figure 17: For radial derivatives, points in front of and behind the point of interest are selected. A_z values at the selected points are differenced to give an approximation of the derivative at the center point.

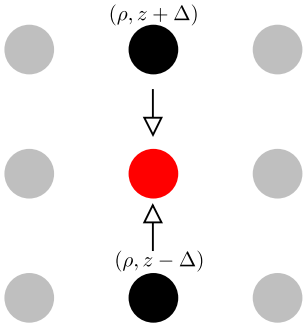

Figure 18: For first order height derivatives, points above and below the point of interest are selected. A_z values at the selected points are differenced to give an approximation of the derivative at the center point. For second order derivatives, all three highlighted points are selected and the second-order difference formula of Equation 26 is used.

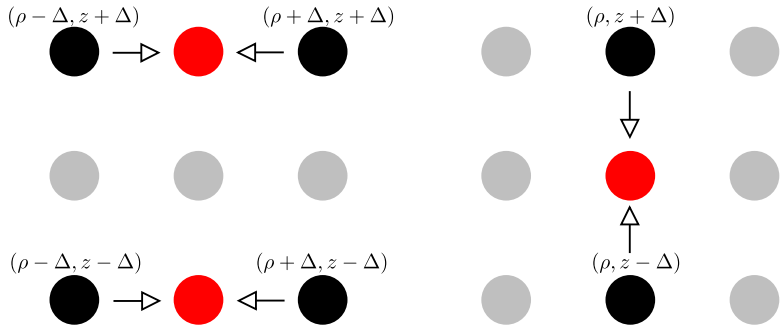

(a) The radial derivative at $z + \Delta$ and $z - \Delta$ is calculated by finite differences. The four corner points are selected and differenced in the approximation.

(b) The radial differences from the left panel are differenced again along the height dimension of the grid.

Figure 19: The two step algorithm to calculate second order mixed partial derivatives is detailed.

Once the fields E_ρ, H_ϕ, and E_z are known at all (ρ, z) values of interest, the time-average Poynting vector $\mathbf{S} = (S_\rho, S_\phi, S_z)$ can be calculated at those points by the relationship

$$\mathbf{S} = \frac{1}{2}\Re[\mathbf{E} \times \mathbf{H}^*], \tag{30}$$

where the symbol $\Re$ denotes the real-part of a complex quantity, and * is the complex conjugation operator. Expanding this cross-product and recalling that many of the components of the fields are zero by Equation 20 reveals that $S_\phi = 0$ and

$$S_\rho = \frac{1}{2}\Re\left[-E_z H_\phi^*\right], \tag{31}$$

$$S_z = \frac{1}{2}\Re\left[E_\rho H_\phi^*\right]. \tag{32}$$

The time-averaged Poynting vector magnitude is calculated from the vector components as

$$S = |\mathbf{S}| = \sqrt{S_\rho^2 + S_z^2}. \tag{33}$$

This is the magnitude of the incident flux of electromagnetic power in $\mathrm{W/m^2}$ at a given point in space. To go from a flux to an amount of available power, the time-averaged Poynting vector magnitude is multiplied by an effective area of an isotropic receiver, which is $\frac{\lambda_0^2}{4\pi}$. The final formula for the received power is then

$$P_{RX} = \frac{\lambda_0^2}{4\pi} S. \tag{34}$$

This concludes the description of how the magnetic vector potential, as calculated by SI quadrature, is used to calculate physically and practically meaningful signal power/strength values in a wireless channel. The sequence of Equations 24-34 are implemented to give power values in space on any set of points. A side-effect is that the electromagnetic field components are also known at all points of interest, something that will be of future use in formulating surface scattering methodologies to simulate metallic or other inhomogeneous inclusions in the medium.

2.8 Numerical Experiments and Verification

The previous sections have discussed a specific set of numerical algorithms for calculating the potentials of a vertical dipole in multilayered media. This computer model of propagation should be verified for correctness, which is the purpose of this section. One approach to verification of an electromagnetics code is to compare the results it provides to available analytical, reference, or benchmark solutions. A complimentary approach is to analyze the resulting fields for consistency with expected properties of all solutions to Maxwell's equations. For example, electromagnetic fields should conserve energy according the the Poynting theorem. They should also obey the boundary conditions. The phase propagation of solutions should be outward, and this phase propagation should be radially away from the sources in straight lines in homogeneous media. The degree to which the simulated results satisfy these properties and conditions can be evaluated as an internal consistency check.

At the time of writing, a reference code for EM propagation problems in general multilayered media was unavailable. The general problem also does not admit a known closed-form solution, which motivated the developments of this chapter to begin with. However, for certain simplified geometries and idealized material properties, closed-form analytical solutions are available. For an impulsive current-density element radiating in free-space, the solutions for the fields can be written in closed form. The form can be directly derived from the multilayer theory developed in this chapter. In particular, free-space can be considered a single infinite slab with index of refraction $n = 1$. By the radiation condition, the two generalized reflection coefficients in the layer must be zero. Equation 4 then simplifies to

$$\tilde{A}_z(k_\rho, z, z') = j\frac{\mu_0 \tilde{I}_{z0}}{8\pi^2}\frac{e^{jk_z|z-z'|}}{k_z}. \tag{35}$$

Recall that $k_z = \sqrt{k_0^2 - k_\rho^2}$ is the free-space z-wavenumber corresponding to a radial wavenumber k_ρ. This is derived by using Equation 13 with the single layer wavenumber $k_\ell = k_0$, and

the ℓ subscripts have been suppressed since there is only one layer. The spatial field corresponding to Equation 35 can be calculated by inserting Equation 35 into the SI of Equation 8, resulting in

$$A_z(\rho, z, z') = j\frac{\mu_0 \tilde{I}_{z0}}{4\pi} \int_0^\infty \frac{e^{jk_z|z-z'|}}{k_z} J_0(k_\rho \rho) k_\rho \, dk_\rho = \mu_0 \tilde{I}_{z0} \frac{e^{jkR}}{4\pi R}, \tag{36}$$

where $R = \sqrt{\rho^2 + (z - z')^2}$ and $\rho^2 = x^2 + y^2$. The equality is a well-known integral identity known as the *Sommerfeld identity*; the interested reader is referred to a proof that appears in Section 5.1.1 of [25]. The rightmost expression of Equation 36 is a spherical wave that can be directly calculated in the spatial domain. It serves as a closed-form, easily calculable, reference solution against which to validate the Sommerfeld integral calculations.

To simulate free-space conditions in the developed computer code, a three-layer environmental model was used. Each layer has index of refraction equal to the free-space value, $n_1 = n_2 = n_3 = 1$. A dipole is embedded in the middle layer of the structure. The resultant magnetic vector potential and the reference solution of Equation 36 are visualized in Figure 20.

The SI method presented, when used to verify the Sommerfeld identity, results in field values that are in maximum error of less than 0.3 dB of the analytical solution, in a $50\lambda_0$ tall region extending $200\lambda_0$ away from the source. This translates to SI results that are within approximately 3.5% of the analytical solution. The error is surprisingly large, given that all the intermediate calculations are carried out to close to machine precision. The Chebyshev polynomial interpolant of the integrand is supposed to be precise to 15 digits when using the Chebfun package [116], and yet the final results are in error by 3.5%. The error also appears to increase with range near the dipole height $z = z'$. Increasing error with range ensures that the solution will be essentially useless for very far-field calculations. However, asymptotic Filon-type quadrature routines are supposed to become *more* accurate for large values of the oscillation parameter [113], which is the range ρ in this case. These inconsistencies are caused by neglecting a qualification in the use of Filon-type quadratures: the integrands should have several degrees of regularity and smoothness.

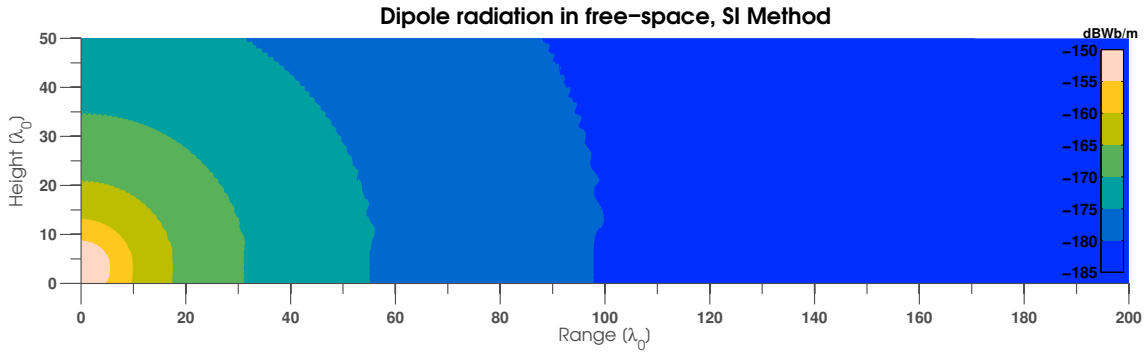

(a)

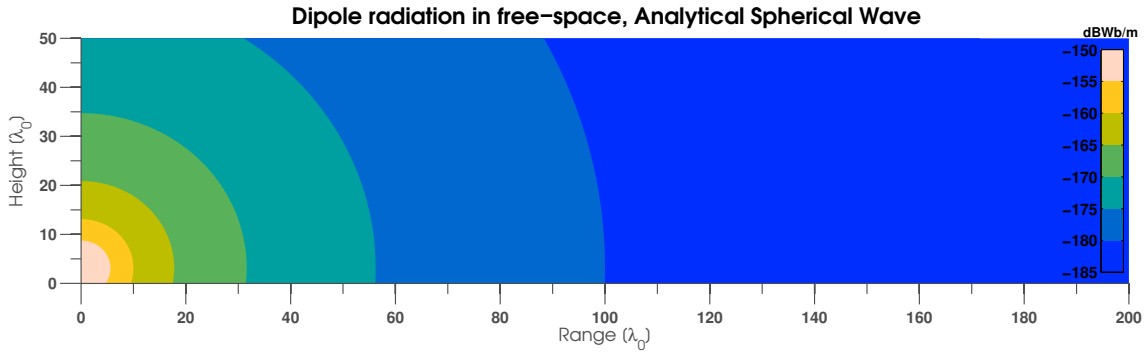

(b)

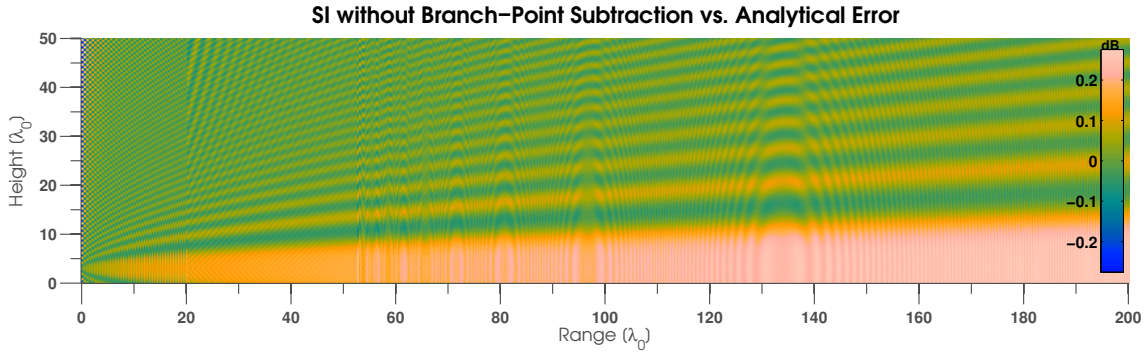

(c)

Figure 20: A dipole source radiates in unbounded free-space. The magnetic vector potential is calculated via the SI method in the top panel, and by the closed form expression of Equation 36 in the middle panel. The most visible difference in the fields is a subtle undulation in the contours in the SI method plot that is not present in the closed form solution. The bottom panel shows that the error between the analytical solution and the SI solution is less than 0.3 dB across the entire plot. However, the error appears to become larger with distance in a parabolic-shaped region away from the source.

However, the free-space SDGF contains a particularly non-smooth type of discontinuity . The free-space SDGF of Equation 35 is proportional to $1/k_z = (k_0^2 - k_\rho^2)^{-1/2}$, which takes an infinite value at $k_\rho = k_0$. This contrasts with SDGF behavior in multilayers representing realistic propagation in atmospheric refractivity above lossy ground. The behavior of a realistic SDGF was previously presented in Figure 15, where it was seen that the SDGF is continuous at the branch-point $k_\rho = k_0$. There is a singularity at the branch-point in Figure 15, but it is in the first derivative of the SDGF. On the other hand, Equation 35 contains an infinite value at the branch-point, which is a problem for accurately representing the function by a Chebyshev polynomial interpolant. A polynomial function cannot attain a value of infinity for any finite argument. Therefore, a Chebyshev polynomial interpolant is a very poor approximation to any function with a singularity, which is the case for the SDGF in unbounded free-space.

For more accurate results in unbounded free-space, an alternative quadrature approach is required that accounts for the $1/k_z$ singularity explicitly in it's formulation. One approach would be to analytically extract the singularity in a way similar to how pole singularities were extracted previously in Section 2.5.1. Note that at the branch-point $k_z = 0$. Expanding the SDGF about the point $k_z = 0$ in a Taylor series gives insight into the nature of the singularity.

$$\tilde{A}_z(k_\rho, z, z') = j\frac{\mu_0 \tilde{I}_{z0}}{8\pi^2}\frac{e^{jk_z|z-z'|}}{k_z} = j\frac{\mu_0 \tilde{I}_{z0}}{8\pi^2}\left(\frac{1}{k_z} + j|z-z'| - \frac{|z-z'|^2 k_z}{2} + O(k_z^2)\right) \tag{37}$$

Therefore, the quantity $\tilde{A}_z(k_\rho, z, z') - j\frac{\mu_0 \tilde{I}_{z0}}{8\pi^2}\frac{1}{k_z}$ is regular and contains no singularities. The subtracted singularity must be accounted for by integrating it in closed form, and adding it back into the spatial domain. The final decomposition of the SDGF is then

$$\tilde{A}_z(k_\rho, z, z') = j\frac{\mu_0 \tilde{I}_{z0}}{8\pi^2}\left(\frac{e^{jk_z|z-z'|} - 1}{k_z} + \frac{1}{k_z}\right). \tag{38}$$

Upon inserting into the SI, the decomposition is

$$A_z(\rho, z, z') = j\frac{\mu_0 \tilde{I}_{z0}}{4\pi}\left(\int_0^\infty \frac{e^{jk_z|z-z'|} - 1}{k_z} J_0(k_\rho\rho)k_\rho \, dk_\rho + \int_0^\infty \frac{1}{k_z} J_0(k_\rho\rho)k_\rho \, dk_\rho\right). \tag{39}$$

The left integrand in Equation 39 is non-singular at $k_z = 0$ by the Taylor series expansion of Equation 37 and the integral can be evaluated by quadrature. The right integral admits a closed form solution, given by

$$\int_0^\infty \frac{1}{k_z} J_0(k_\rho \rho) k_\rho \, dk_\rho = -\frac{j e^{jk_0\rho}}{\rho}. \tag{40}$$

Subtracting a $1/k_z$ singularity makes the part of the SDGF that will be integrated by quadrature continuous at the branch point, for all values of $|z - z'|$. However, the subtracted singularity has also introduced more slowly decaying integrand tail for values away from $z = z'$. The original SDGF quantity decays exponentially for $k_\rho > k_0$ for any heights $z \neq z'$ that are away from the source. This can be seen by considering the $k_\rho >> k_0$ asymptotic approximation

$$\frac{e^{jk_z|z-z'|}}{k_z} = \frac{e^{j\sqrt{k_0^2-k_\rho^2}|z-z'|}}{\sqrt{k_0^2 - k_\rho^2}} \overset{k_\rho\to\infty}{\approx} \frac{e^{-|z-z'|k_\rho}}{jk_\rho}, \tag{41}$$

which is dominated by the exponential behavior for large k_ρ. On the other hand, the singularity-subtracted SDGF is asymptotically

$$\frac{e^{jk_z|z-z'|} - 1}{k_z} = \frac{e^{j\sqrt{k_0^2-k_\rho^2}|z-z'|} - 1}{\sqrt{k_0^2 - k_\rho^2}} \overset{k_\rho\to\infty}{\approx} \frac{e^{-|z-z'|k_\rho}}{jk_\rho} - \frac{1}{jk_\rho} \approx -\frac{1}{jk_\rho}, \tag{42}$$

regardless of $|z - z'|$. Because a finite truncation of the infinite integration interval will ultimately be used, $O(1/k_\rho)$ behavior in the integrand tail is not expected to give accurate results either. An alternative spectral-domain branch-point singularity subtraction function has been proposed by [117]. The idea used in [117] is to subtract not only the singular term at the branch point, but to also introduce a second correction term of $O(1/k_\rho)$ that cancels the slowly decaying tail introduced by the first term, while not interfering with the behavior at the branch point. The correction term was also chosen such that it has a closed-form SI, and can be analytically added back in the spatial domain. Adapting these ideas, the SDGF will now be decomposed as

$$\tilde{A}_z(k_\rho, z, z') = j\frac{\mu_0 \tilde{I}_{z0}}{8\pi^2} \left(\frac{e^{jk_z|z-z'|} - 1 + \frac{k_z}{j\sqrt{k_0^2+k_\rho^2}}}{k_z} + \frac{1}{k_z} - \frac{1}{j\sqrt{k_0^2 + k_\rho^2}} \right). \tag{43}$$

The new singularity-subtracted term is asymptotically

$$\frac{e^{jk_z|z-z'|} - 1 + \frac{k_z}{j\sqrt{k_0^2+k_\rho^2}}}{k_z} \overset{k_\rho\to\infty}{\approx} \frac{e^{-|z-z'|k_\rho}}{jk_\rho} - \frac{1}{jk_\rho} + \frac{1}{jk_\rho} = -\frac{e^{-|z-z'|k_\rho}}{jk_\rho}, \tag{44}$$

to first-order. Although the $O(1/k_\rho)$ terms cancel, a higher order asymptotic analysis can demonstrate that the above is $O(1/k_\rho^3)$. A next asymptotic correction of $O\left((k_0^2 + k_\rho^2)^{-3/2}\right)$ can be derived, and the resulting singularity-subtracted SDGF is $O(1/k_\rho^5)$. The process can be iterated over larger odd-order correction terms, until the tail decays sufficiently by the finite integration interval truncation point, $k_{\max}$. Each subtracted correction term must be added back into the spatial domain, using analytical formulas for the SI of each correction term. Calculation of the first few terms in a such an expansion suggests that analytical formulas exist for all higher orders. An algorithm based on higher order approximations is a fascinating direction for future research.

For the present work, only the first order correction originally presented by [117] is retained. In order to account for the effect of singularity-subtraction, the corresponding closed form SIs must be added back to the result in the spatial domain. Inserting the SDGF decomposition of Equation 43 into the SI results in expressions involving the integral

$$\int_0^\infty \left(\frac{1}{k_z} - \frac{1}{j\sqrt{k_0^2 + k_\rho^2}}\right) J_0(k_\rho\rho)k_\rho \, dk_\rho = -\frac{je^{jk_0\rho}}{\rho} + \frac{je^{-k_0\rho}}{\rho}, \tag{45}$$

which is analogous to Equation 11 of [117]. Figure 21 presents the results of using the proposed branch-point singularity subtraction approach to calculating a free-space SI.

Comparing the errors in Figures 20 and 21, one can conclude that the two SI methods, with and without branch-point singularity subtraction, are complementary. The method without branch-point singularity subtraction performs very well in a parabolic-shaped region outward in range directly away from the source; the method with branch-point subtraction performs very poorly in the same region. Complementarily, outside the parabolic-shaped region, the method without branch-point subtraction often attains less error than the method with branch-point subtraction. If analytical estimates of the error were available *a*

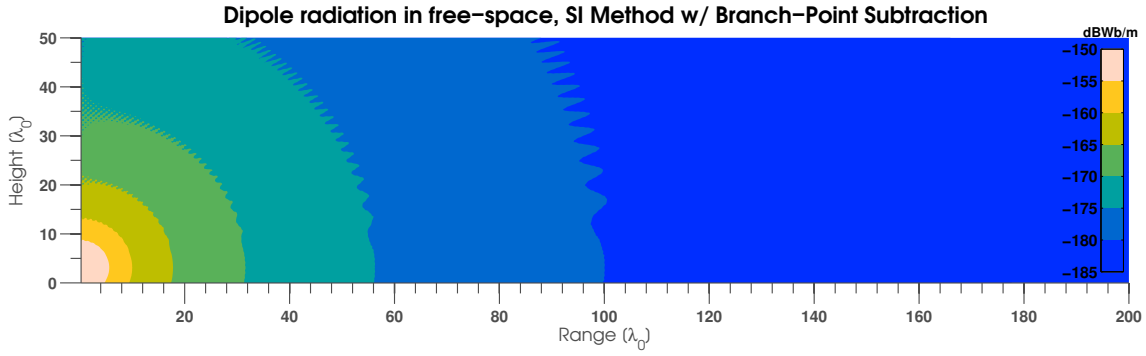

(a)

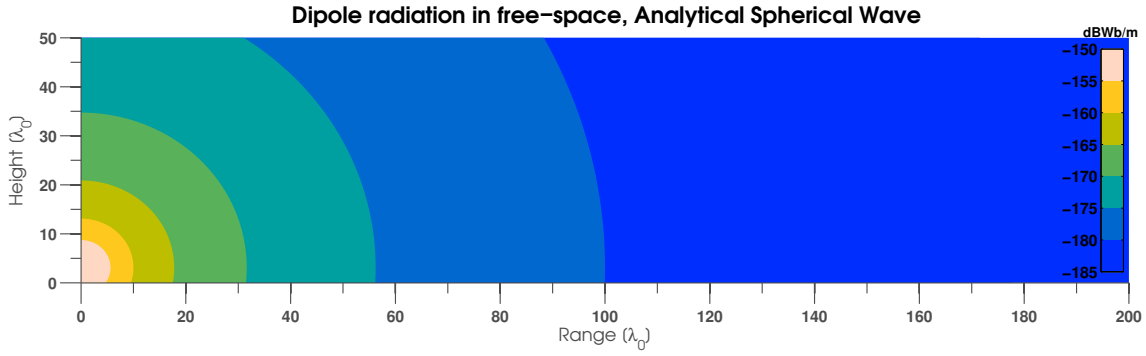

(b)

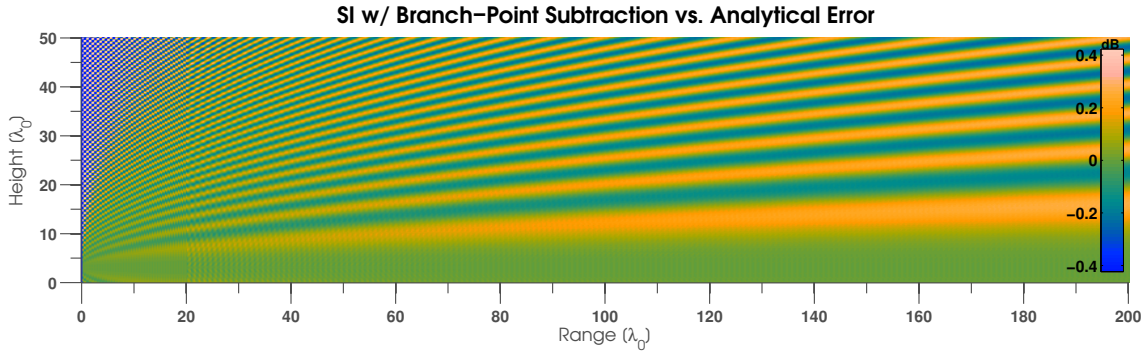

(c)

Figure 21: A dipole source radiates in unbounded free-space. The magnetic vector potential is calculated via the SI method in the top panel, and by the closed form expression of Equation 36 in the middle panel. The SI method employs branch-point singularity subtraction in the spectral domain, and adds the effect of the singularity back in the spatial domain. The most visible difference between the analytical and SI solution is a subtle undulation in the contours. The bottom panel shows that the error between the analytical solution and the SI solution is less than 0.45 dB across the entire plot. However, the error in a parabolic-shaped region away from the source is much smaller, making this approach suitable to far-field calculations.

priori, then a hybrid algorithm could be constructed that selects the more accurate method at each requested field evaluation point based upon the expected error of both methods there.

It should finally be noted that the test case of free-space propagation only serves to validate the SI method. For practical free-space calculations, one would never use the SI method, but instead use the available closed-form spherical wave formula. This section has demonstrated that one must go to extended lengths to obtain accurate results from the SI in free-space. In other, more complex media with multiple layers and loss, the SDGF has been observed to be more regular at the branch point. These more complex multilayer structures correspond to typical propagation problems with atmosphere and ground, and the problems at the branch-point appear to be lessened in practical problems with lossy ground and multiple layers. The simplest multilayer lossy problem is considered next, and serves as a more realistic benchmark for the kinds of calculations for which the present SI implementation was designed.

2.8.1 Comparison with Image-Theory Solutions

In addition to the free-space reference solution, another readily available analytical solution to a multilayer propagation problem is the *image theory* solution that applies when waves are radiated by a source above an infinite half-space (ground plane) of zero resistivity. It is well known that such a perfect electric conductor (PEC) can be replaced by a fictitious image source in such a way that the boundary condition of zero tangential E on the surface of the conductor is enforced. The fields radiated by the original source and image source satisfy Maxwell's equations in the upper half-space, and satisfy the boundary conditions on the conductor. Then by the uniqueness theorem, they represent a valid expression of the field solution in the region above the conductor. This is depicted in Figure 22.

Using image theory, a closed form expression for the magnetic vector potential above a PEC can be derived; it is a simple sum of two terms, each of the form of Equation 36. In order to make calculations over true PEC, the developed computational model would

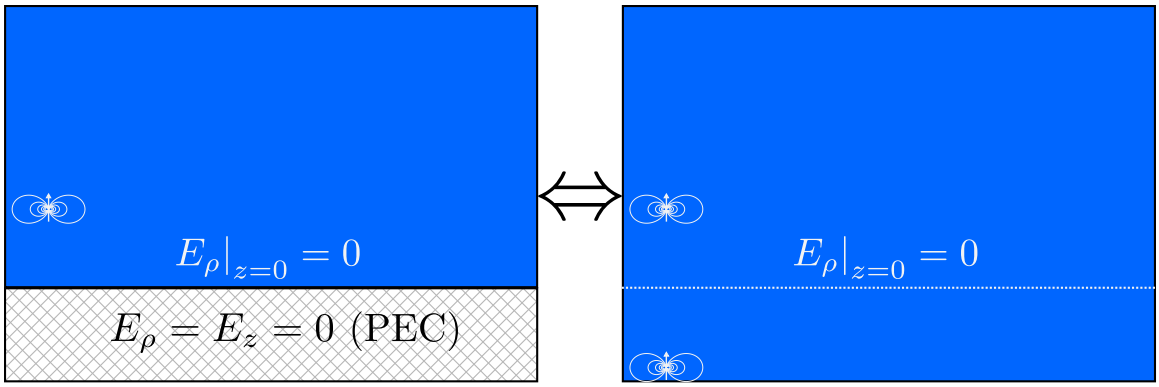

Figure 22: A dipole radiates above a PEC material. The PEC is replaced by an image source radiating in free space in the right panel. The boundary condition on the PEC interface (vanishing tangential **E**) is satisfied by this arrangement of two sources, and the fields radiated by the two dipoles satisfy Maxwell's equations outside the PEC. By the uniqueness theorem, the fields in the upper half-space of both panels are equal.

require additional modifications and explicit handling of the special-case of PEC boundary conditions. Instead, we seek to directly make comparisons between the image-theory solution and the SI solution. This can be accomplished by selecting an environmental model that closely approximates the image-theory scenario. A dipole radiating in air above a highly conductive material in place of the PEC should be a very good approximation to the image-theory scenario. The material chosen to approximate PEC in the simulation was copper, with conductivity of $\sigma = 5.96 \times 10^7$ S/m and dielectric constant $\varepsilon_r = 1$. Figure 23 presents contour plots of the magnetic vector potential of a dipole located $3.1123\lambda_0$ over copper, calculated by the SI method, and over PEC, calculated using closed-form image theory expressions.

The spatial average of the dB difference between the two solutions over the simulated domain is less than 0.03 dB in magnitude. Though not visibly apparent in the contour plots, larger discrepancies of up to 22 dB exist between the two solutions; however, these isolated errors occur in or near the destructive-interference minima that are visible as dark radial lines appearing to emanate from the origin. These minima occur where the source and image contributions to the fields cancel in the far-field limit. It appears that using the SI method over copper produces interference minima that are not precisely aligned with those

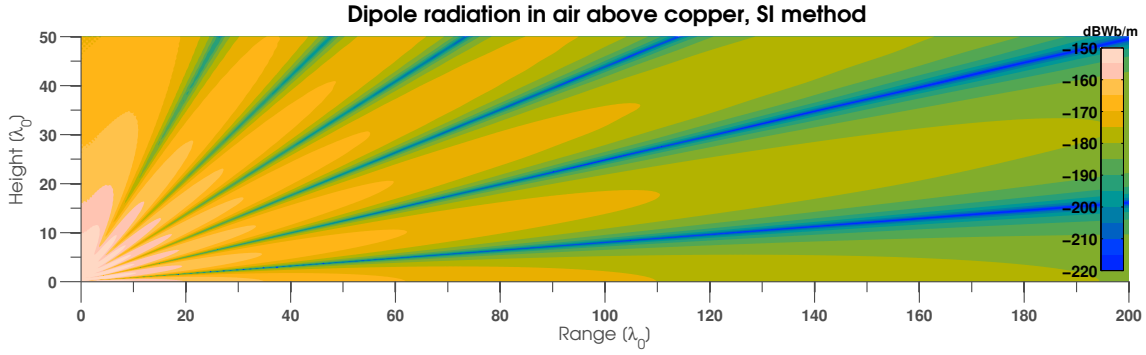

(a)

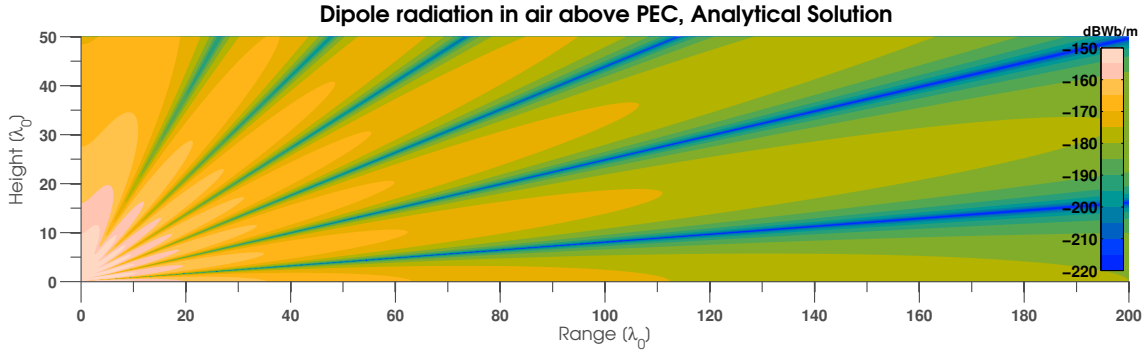

(b)

Figure 23: A dipole source placed $3.1123\lambda_0$ over a ground plane radiates. The magnetic vector potential is calculated via the SI method in the upper panel, and by image-theory expressions in the lower. The results are visually indistinguishable, but analysis shows that the two can be in error by 20 dB in the visible minima bands.

from the analytical PEC case. However, given that the environmental models between the two scenarios actually are different, perhaps this effect is a real difference between propagation above PEC as opposed to propagation above copper. Another possibility is that finite-precision calculations result in sums that do not cancel to the same precision as the PEC analytical formulas. In strong destructive-interference regions, perhaps the presented SI method cannot be considered accurate. Nonetheless, the SI result is within fractions of a dB of the analytical solution away from these destructive interference regions, and predicts the interference regions themselves with error in magnitude, so this discrepancy is not considered a severe limitation of the technique.

2.8.2 Performance Under Coordinate Transformation

The Helmholtz equation has the very general property that when it undergoes a conformal (angle preserving) coordinate transformation, the result is another Helmholtz equation with transformed material properties (see Section 2 of [118]). This property has most recently been studied for the design of optical devices in the burgeoning field of transformation optics. However, the property holds in general for any frequency of EM propagation, and has been widely used in the radar propagation modeling community as the "earth-flattening" transformation [41]. This section presents an earth-flattening transformation of the SI methodology as a validating example. Figure 24 demonstrates how a coordinate transformation can be interpreted as propagation in a transformed medium, and vice-versa.

The transformation from Figure 24c to Figure 24d is of particular importance to long range propagation for radar applications. Accurately modeling beyond-the-horizon propagation requires accounting for the curvature of the earth, which generally requires an explicit surface scattering calculation in the picture of Figure 24c. However, by accounting for earth curvature in a flat coordinate system like Figure 24d with a *modified* refractive index that bends radio paths upwards, the correct results for a curved earth can be obtained. For a mapping from a spherical patch with radius of curvature a to flat surface, the modified

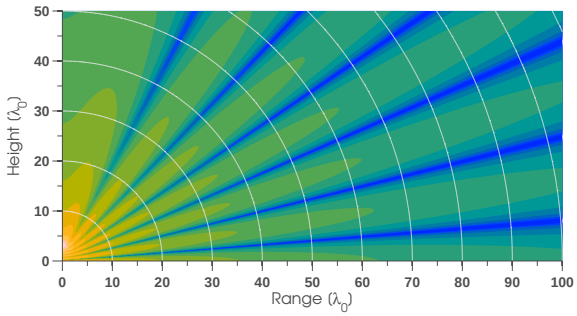

(a) A dipole radiates above a flat plane.

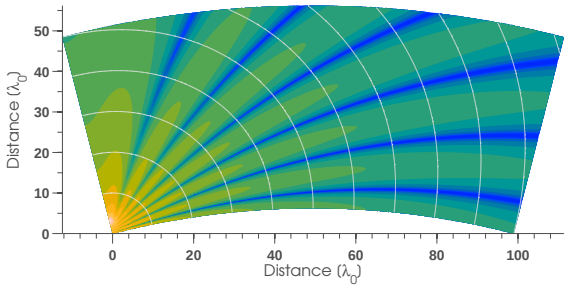

(b) The coordinates of panel (a) are mapped from flat to curved coordinates

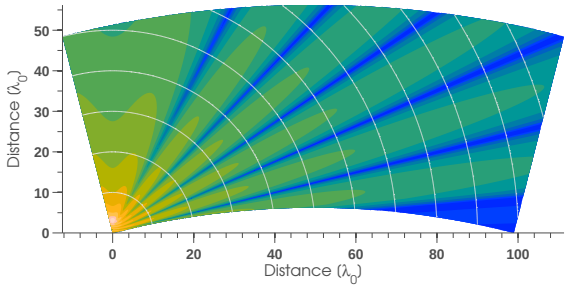

(c) A dipole radiates above a sphere.

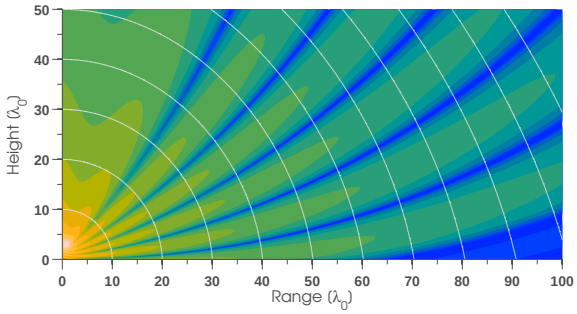

(d) The coordinates of panel (c) are mapped from curved to flat coordinates

Figure 24: The fields of panel (a) satisfy the free-space Helmholtz equation above a plane. If the coordinates are remapped without changing the field values, as in panel (b), the new fields satisfy the Helmholtz equation in a refractive medium that bends rays downwards. The downward bend is apparent upon comparing panels (b) and (c). The fields in panel (c) satisfy the free-space Helmholtz equation near the sphere, and when mapped to a flattened coordinate system in panel (d), the new fields satisfy a Helmholtz equation in an upward-refracting medium.

refractive index is [41]

$$m(z) = n(z)\left(1 + \frac{z}{a}\right), \tag{46}$$

where z is measured radially outward from the sphere surface and $n(z)$ is the original refractive index profile. This is the standard modified refractive index used in the radar community to account for the curvature of the earth, known as the standard *earth-flattening transformation*. The coordinate transformation corresponding to the modified refractive index of Equation 46 is not, strictly speaking, a conformal mapping. However, it can be shown that it approximates a conformal mapping near the surface of the sphere, e.g., for low altitude propagation problems above the earth [41].

Figure 25 presents the results of using a modified refractive index above the earth to account for earth curvature in the SI methodology of this chapter. A dipole radiating at 3 GHz is placed 20 m above the surface of a conductive earth with radius $a = 6371$ km. The earth radius was used with Equation 46 to calculate a modified refractive index corresponding to no initial gradient, $n(z) = 1$. The modified refractive index is a linear function of height that takes a value of 1 at the surface, and increases linearly with height at a rate of $1/a \approx 1.57 \times 10^{-4}$ units per kilometer. The simulated domain was 500 m in height and 100 km in range.

In the flat-earth coordinates of Figure 25a, the modified refractive index has the expected effect of refracting the visible beams and nulls upwards into curved paths. When mapped to curved-earth coordinates in Figure 25b, the paths can be seen to follow straight lines, as expected. This result serves as a check for consistency of the presented method. Using a mathematically derived refractive profile to account for a coordinate transformation, the SI method, which has no explicit information about coordinate changes, calculates the correct result of straight radio paths. Furthermore, what looks like a low power region due to upward refraction in the flat coordinates correctly maps to propagation by diffraction in the geometrical shadow region.

As a final note, at a frequency of 3 GHz, this domain is *extremely* electrically large: it

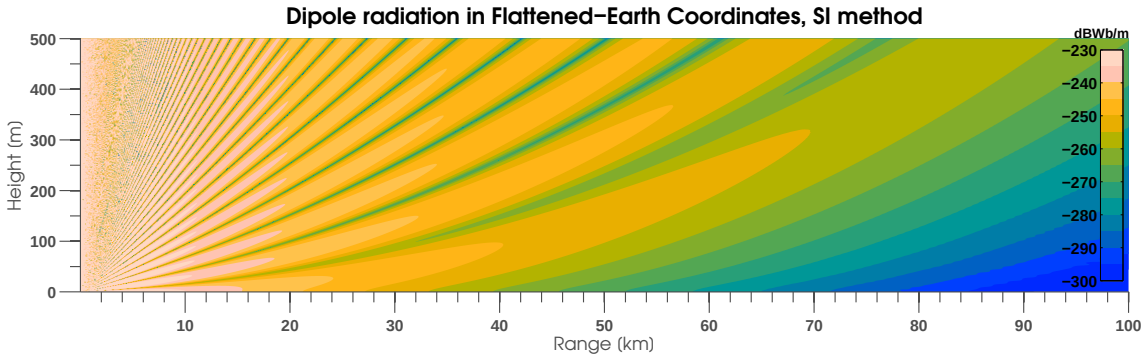

(a) A dipole radiates in subrefractive conditions.

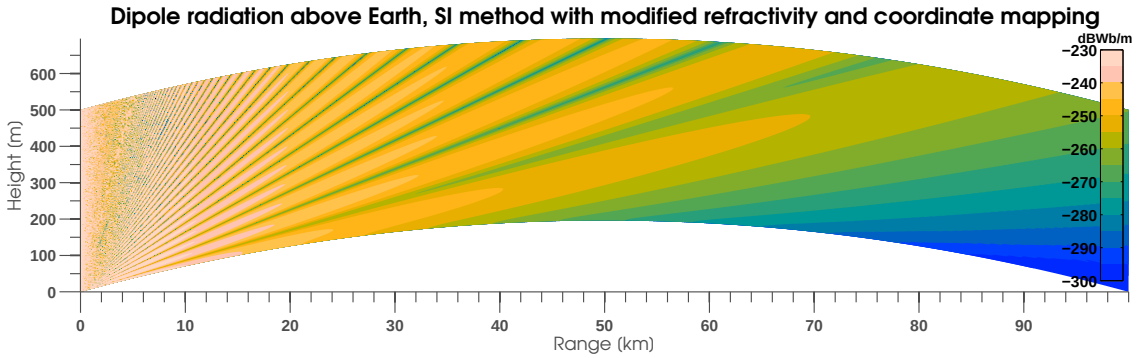

(b) The coordinates of panel (a) are mapped from flat to curved coordinates

Figure 25: The SI method is used in subrefractive conditions derived from the earth-flattening transformation in panel (a). Upon mapping the fields to curved-Earth coordinates in panel (b), the apparent interference fringes and beams above the sphere form straight lines.

is over $5000\lambda_0$ in height and $10^6\lambda_0$ in range. The SI method with asymptotic quadrature, as presented in this chapter, is very well suited to calculations in these extremely large domains. Once the Green's functions are sufficiently resolved to machine precision in the spectral domain, the far-fields at any arbitrary range can be calculated by the asymptotic FCC quadrature for a fixed-cost. There is no additional computational cost to calculating the fields at 100 km compared to the same calculation at 10 m. This property also enables decoupling of the field evaluation grid from that on which the refractive profile is defined. Although the refractive index profile was simulated at $\Delta z \approx 10$ cm resolution, the contours of Figure 25 were generated from calculations on a grid of 10 m range and 1 m height resolution. This is remarkable when compared to other full-wave methods for EM propagation (e.g. FEM, FDTD), which generally require the evaluation and material grids to be of the same subwavelength resolution. At the time of writing, a high end laptop computer can generate Figure 25 in about 30 minutes using the developed MATLAB software algorithm.

2.8.3 Conclusion

This chapter has presented a model for EM propagation in the class of nonmagnetic multilayers using Sommerfeld integrals. The novel aspects of the presented method have been highlighted, and include using 1) a direct sparse-matrix solution in the spectral domain, 2) an adaptive sampling to resolve the spectral domain integrands, and 3) an asymptotic quadrature routine for far-field calculations. A sequence of finite-difference based methods have been presented to calculate all EM fields and power-related quantities from the magnetic vector potential. The model was validated against two available analytical solutions, and checked for consistency with expected results in a third case.

CHAPTER 3

COMPARISONS OF SOMMERFELD INTEGRAL MODEL AND MEASURED DATA

Chapter Summary: Concurrent RF and atmospheric measurements were conducted August 22 - August 23, 2009, in Panama City, Florida by a team of researchers associated with the US Navy. The collected RF data contain periods of fluctuating signal level that are unexpected given the experimental setup of constant transmitter power and fixed antenna placement, indicating the possibility of atmospheric effects on propagation. Both the RF and atmospheric data are analyzed, and the propagation environment is simulated using the Sommerfeld integral model developed in Chapter 2. The atmospheric data are analyzed in the context of the Monin-Obukhov theory of the near-surface atmosphere. The combined atmospheric and RF analysis at UHF frequencies near the land surface is the first of its kind to be presented. The simulation results are compared against the measurements to examine if the observed fluctuations can be plausibly attributed to refractive conditions in the atmosphere. It is found that in this particular scenario, it is unlikely that the observed levels of variation are attributable to atmospheric effects.

3.1 Description of the Measurements

In the summer of 2009, RF and atmospheric measurements were conducted in a flat, grassy field in Panama City, Florida. The grass height was approximately $4 - 8$ cm tall. The experimental system consisted of RF transmitter and receiver units. A signal generator in the transmitter produced a sinusoid at a frequency of $f = 1.78$ GHz. The generated sinusoid was amplified to a nominal power level of 1 W (30 dBm) and then transmitted via a horn antenna. The receiver consisted of three different antennas: a corner reflector, a discone, and a horn. The output of each antenna was passed into a separate receive chain.

Each chain consists of a band-pass filter centered at 1.78 GHz and a power detector. The output from the power detectors were logged to solid state memory, nominally once every nine milliseconds. Concurrently, measurements of atmospheric parameters, including the temperature and humidity, were collected once per second at various heights on a mast. The atmospheric sensor heights were 10.0 cm, 17.8 cm, 31.6 cm, 56.2 cm, and 100.0 cm above the ground surface.

The transmitter and receiver were fixed at a separation distance of 70 m, with the directional antennas (the corner reflector and horns) oriented with the main beam aligned with the straight line between transmitter and receiver. The alignment was achieved by adjusting the angles of transmitter and receiver antennas until maximal power was achieved at the receiver. This alignment procedure is estimated to be accurate to within $\pm 5^{\circ}$ in both azimuth and elevation angle. The transmit horn antenna was placed at a height of 90 cm above ground level, and the receive antennas were also placed at the same height 70 m away, with the horn in the center of a horizontal cross-bar that supported all three antennas. The experimental data collection began on the night of August 22, 2009 at 7:00PM local time in Panama City, Florida, and data collection continued for approximately 15 hours, into the morning of August 23.

3.2 Radiofrequency Data Collection Results

The RF portion of the experiment resulted in three time-series of power levels measured at the three receiver antennas over the course of the experiment. A plot of the measured power vs. time on the three receiver chains in depicted in Figure 26.

The first fact of note is that the three traces are broadly separated from each other. This is the effect of the differing gain / pattern effects of the three antennas. The other interesting fact is that the power level on all three receiver channels is not constant in time. This is unexpected because all antennas were stationary, and the measured transmitter power did not vary. In addition to temporal variations of the order of hundredths of decibels, there are

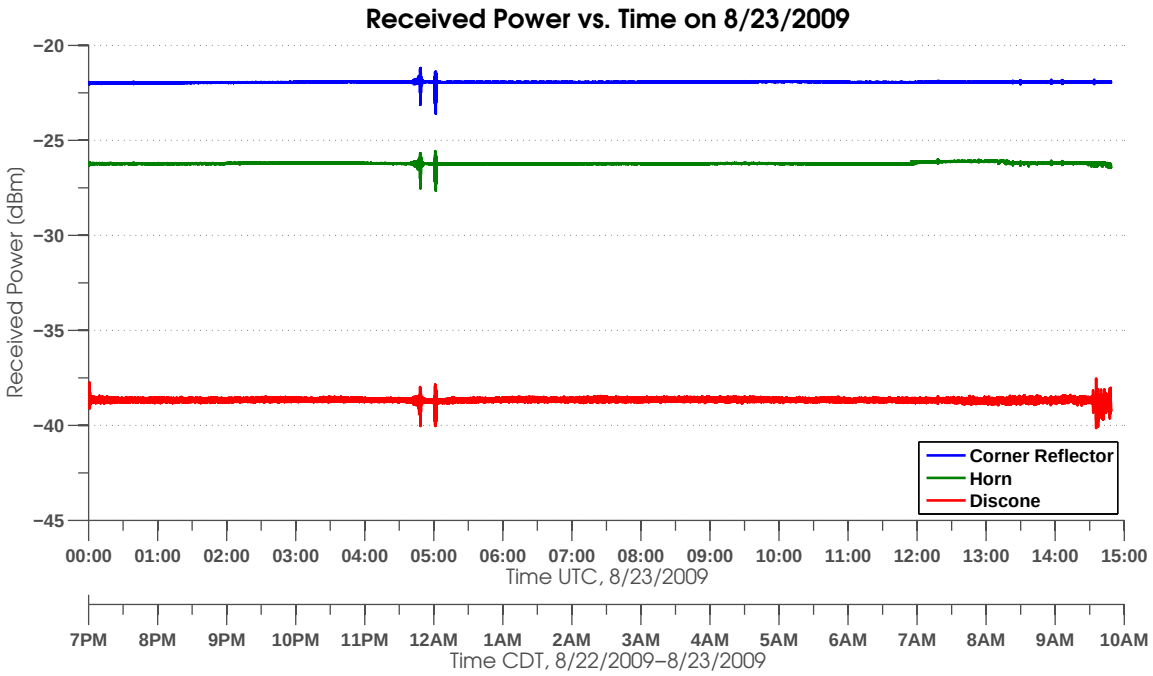

Figure 26: Three time-series were recorded for different receiver antenna types.

periods of time lasting minutes when the received signal levels vary by several decibels, e.g., around 5:00 UTC.

3.3 Atmospheric Data Collection Results

The temperature and humidity of the air were measured at five different heights during the course of the data collection using the aforementioned mast of sensors. The sensors' outputs were written to solid state memory at a nominal rate of once per second. Measurements at multiple heights allows for a profile of air temperature and humidity vs. height to be determined, which can then be used to calculate a refractivity vs. height profile using Equation 1. Although the refractivity given in Equation 1 is also dependent on pressure, this quantity does not vary significantly over the height domain of the measurements. Hence, the pressure is approximated as constant in height for the purposes of this analysis. The temporal variation of the pressure in Panama City on 8/22/2009 to 8/23/2009 was less than three millibars, which corresponds to a 0.3% difference in the refractivity. This justifies neglecting the time-variation of the pressure as well, and so, the pressure is considered a

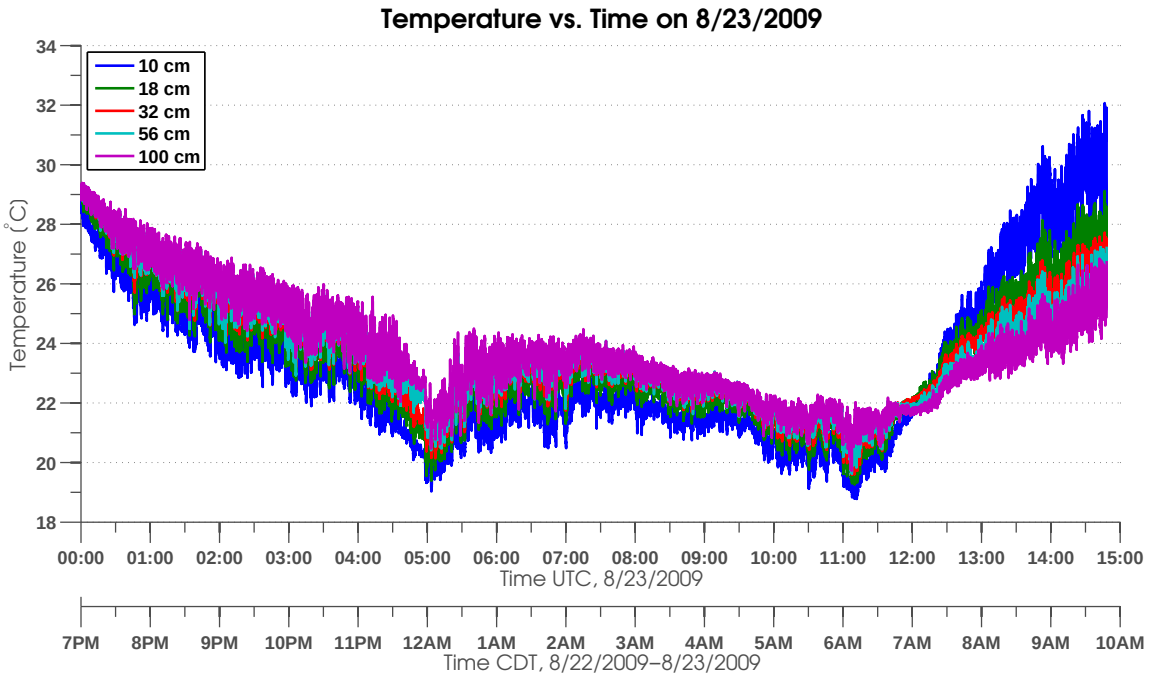

Figure 27: Temperature data were recorded at various heights on a mast of sensors. The sensor heights are indicated in the legend.

constant in height and time for this analysis. The results of the data collection appear in Figures 27 and 28.

3.4 Stochastic Treatment of the Atmospheric Profiles

> **Note:** Because the atmospheric theory of turbulence is unfamiliar to many who take an interest in radio propagation, Appendix C sets up some of the preliminaries of the following discussion of the atmospheric boundary layer. The reader is invited to consult Appendix C or [119] if some detail is unclear or symbol usage unfamiliar in this section.

The collected humidity and temperature data are a spatiotemporal sample of a complicated dynamical process in which heat and humidity diffuse in turbulent eddies of the atmosphere. The standard mathematical approach in the atmospheric literature for turbulent problems is to model the dynamics as a stochastic or random process, consisting of the sum of an average component and a perturbation component. In fluid dynamics communities, this is most

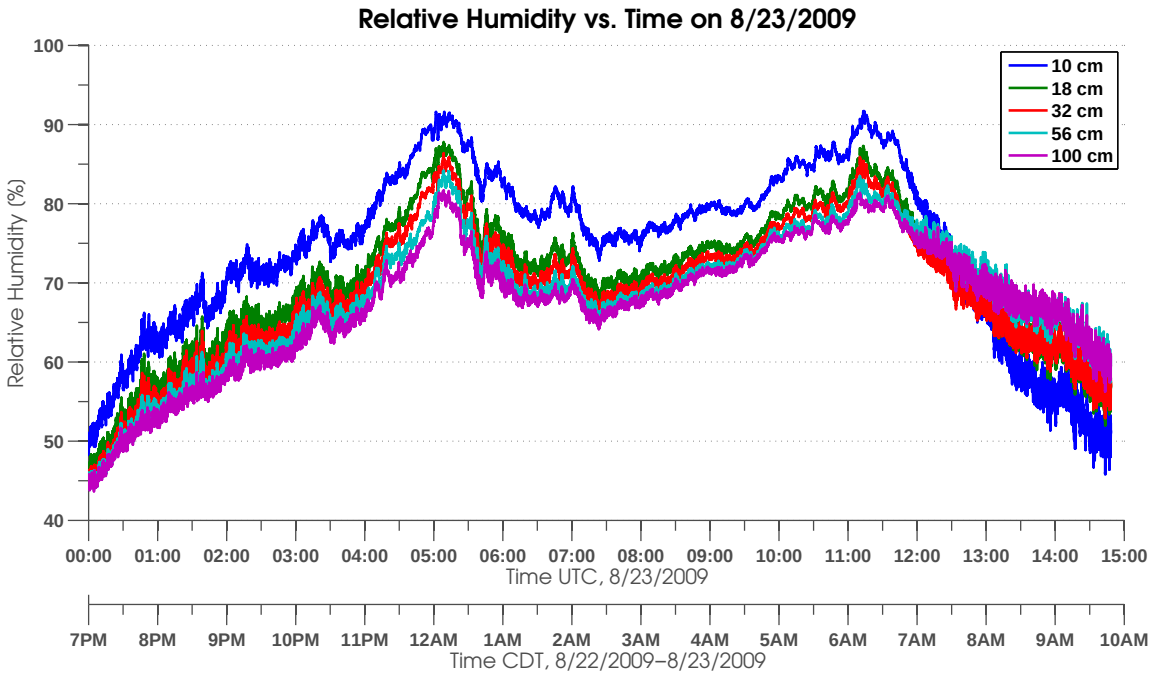

Figure 28: Relative humidity data were recorded at various heights on a mast of sensors. The sensor heights are indicated in the legend.

commonly known as the Reynolds decomposition [120]. The Reynolds decomposition of the temperature T_{tot} and specific humidity q_{tot} can be written as

$$T_{\text{tot}} = T + T', \tag{47}$$

$$q_{\text{tot}} = q + q', \tag{48}$$

where $T = \mathbb{E}[T_{\text{tot}}]$ is the ensemble average of the temperature, T' is the zero-expectation temperature perturbation, $q = \mathbb{E}[q_{\text{tot}}]$ is the ensemble average of the specific humidity, and q' is the zero-expectation humidity perturbation. This kind of decomposition into average and perturbation components is also commonly used in signal processing and telecommunications, making this representation compatible with concepts commonly used in electrical engineering. The ensemble averaged atmospheric effects correspond to the average RF propagation effects; the perturbations in the atmospheric quantities correspond perturbations in the RF about its mean behavior. For the purposes of the present work, the perturbation in the RF effects will be considered a *small-scale* or *scintillation* effect (by analogy

to optical communications through air). The scintillation effects are not considered in this dissertation; instead, the large-scale propagation effects of the average atmospheric profiles are of interest.

Ensemble averages of random processes cannot be directly calculated from observations, since only one realization of a random process can ever be observed in one data collection. However, under the assumption that the temperature and humidity are *ergodic* random processes, time-averages of these quantities can approximate ensemble averages if the averaging time-interval is larger than the correlation time or integral time-scale of the turbulence [119]. Under the ergodic hypothesis, the Reynolds decompositions of temperature and humidity have the form

$$T_{\text{tot}}(z,t) = T(z) + T'(z,t), \tag{49}$$

$$q_{\text{tot}}(z,t) = q(z) + q'(z,t). \tag{50}$$

Both temperature and humidity are the sum of an average height-profile function, and a time-dependent term that captures the stochastic effects of turbulence. To study the large-scale effects on RF propagation, the average atmospheric height-profiles need to be investigated further.

3.4.1 Time-Averaging the Atmospheric Data

The average profiles that appear in Equations 49 and 50 are time independent due to the ergodic assumption about the random processes. However, in addition to small time-scale variations that might be expected from turbulent effects in the atmosphere, the temperature and humidity data exhibit a slowly varying diurnal time-scale and the broader effects of weather systems moving through the area. For example, in Figure 28, between the hours of 4:30-5:30 UTC, the observed relative humidity on all the sensors goes through a cycle of increase and decrease by $7-10$ percentage points. This time-variation cannot be attributed to small-scale turbulent eddies of the kind that would cause scintillation effects in the RF signal. Estimating the time-scale of the slower variations, and separating the large-scale

weather effects from the small scale turbulent effects becomes a formidable estimation problem in itself. To address this issue, a heuristic technique is used, as outlined below.

The difference between two consecutive temperature or humidity samples from one sensor, separated by one second, must approximately be caused by only turbulent effects; the drift that occurs due to large-scale weather and the diurnal cycle can be neglected over one second time scales. By considering the autocorrelation of the differences between data samples of temperature and humidity, it is then possible to estimate the turbulence time-scale. In Figure 29, a portion of the sample autocorrelation of the differences between temperature samples at the lowest sensor height is presented. The autocorrelation function presented decreases from it's maximal value at zero lag, and after 20 seconds, it oscillates with magnitude less than 0.0368.

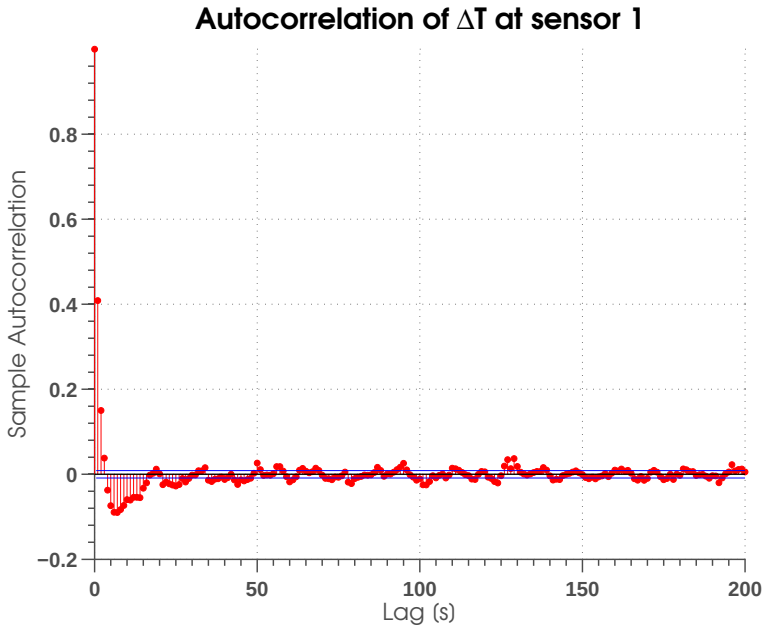

Figure 29: The autocorrelation of dT/dt at sensor 1. The samples are correlated for about twenty seconds, after which they decorrelate.

Figure 29 is representative of the other autocorrelation functions of the measured temperature and humidity at all sensors. In each case, after 20-30 seconds of lag, the measured temperature and humidity decorrelates by oscillating between small values. Informed by these plots, the time-scale of 30 seconds was chosen as a trade-off between reducing the

temporal correlation of the measurements, while not including the effects of significant drifts due to the large-scale weather effects in the area. For the purposes of determining the average height profiles then, the temperature and humidity data were averaged in 30 second blocks. Figure 30 demonstrates that 30-second averaging does indeed reduce the autocorrelation of the temperature data.

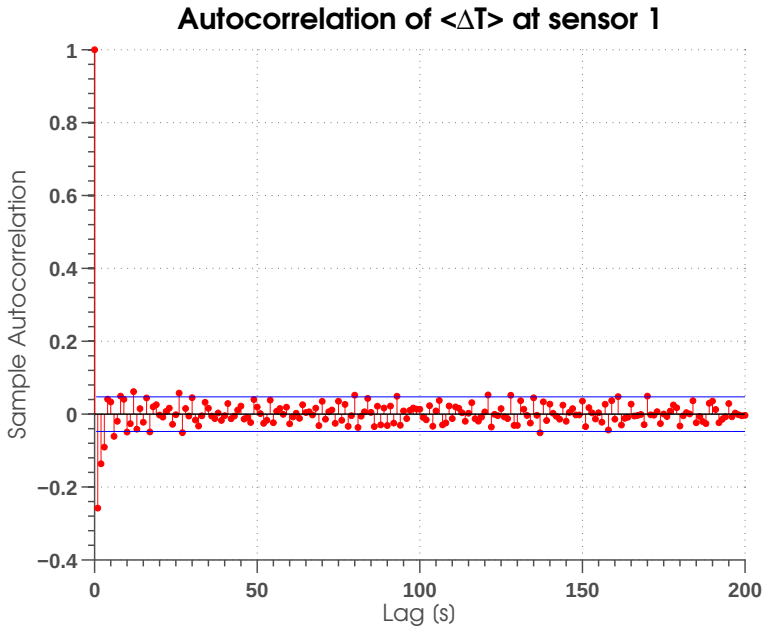

Figure 30: The autocorrelation of $d/dt\ T_{30\text{pt}}$ at sensor 1. The samples decorrelate much more quickly after averaging over 30 seconds. The decorrelation time is about 5 samples now.

3.5 Estimating Continuous Atmospheric Profiles from Measurements

Time-averaging the measured temperature and humidity in blocks of 30 seconds helps to minimize the effects of turbulence and large-scale weather, and approximates the quantities $T(z)$ and $q(z)$ from Equations 49 and 50, sampled on five points in height. These data could be used to directly calculate the refractivity by using Equation 1, which would provide a five-point estimate of the refractive profile in height. A simple five slab dielectric structure could be devised to approximate the atmosphere, and then the RF propagation could be simulated using the model of Chapter 2. However, this coarse model of the environment

could cause artifacts in the RF solution; it is possible that some unresolved detail of the refractive structure, which is not captured by the five-point measurements, will have an effect on the RF propagation. A more desirable approach is to attempt to interpolate the profiles between measurements, and possibly extrapolate them outside the range of measurements, particularly down to the ground level.

Interpolation between observed values can be justified by appealing to assumptions of smoothness and continuity of the profiles. If the profiles are smooth and not highly variable between measurements points, then a smooth function can be used for piecewise interpolation of these data. Common choices for interpolating functions include linear functions or low order polynomials. A related approach is to fit the data to a function with several free parameters, and then find the optimal parameters that minimize the error between the fit-function and the measurements. The "curve-fit" approach can be especially attractive when the parametric fit-function reflects the underlying physics of the measured data. It is important to choose fit-functions that are justifiable from a physical perspective; otherwise, the person conducting the analysis is imposing an underlying principle on the measurements that is not present in nature. When extrapolating measurements outside of their measured domain, strong physical arguments are absolutely necessary to justify a particular fit-function shape. Because extrapolating down to the surface level is desired for conducting RF simulations in the measured refractive environments, attention is now turned to developing fitting-function profile shapes for the humidity and temperature that can be justified from established principles of the fluid dynamics of the atmospheric surface layer.

3.5.1 Temperature and Humidity Profiles in the Surface Layer

Note: Because the atmospheric theory of turbulence is unfamiliar to many who take an interest in radio propagation, Appendix C sets up some of the preliminaries of the following discussion of the atmospheric boundary layer. The reader is invited to consult Appendix C or [119] if some detail is unclear

or symbol usage unfamiliar in this section.

The most general fluid dynamics equations, including the Navier-Stokes equations and physical conservation laws, can be applied to all pertinent quantities written in the Reynolds decomposition, and the averaged equations can be written down. However, the averaged fluid dynamics equations do not depend on only the averaged atmospheric quantities; they also explicitly depend on second order combinations of the perturbation quantities. For example, under horizontal homogeneity, the averaged equation for the humidity is [119]

$$\frac{\partial q}{\partial t} = -\frac{\partial \mathbb{E}\left[u_z' q'\right]}{\partial z}, \tag{51}$$

where u_z' is an upward velocity perturbation and the other quantities retain their previous meaning. The quantity $\mathbb{E}\left[u_z' q'\right]$ is in the form of a statistical covariance between the humidity and upward velocity. Unfortunately, this quantity is unknown, making this another variable to solve for in the system of dynamical equations. These covariances have the physical interpretation of being the mean flux of a quantity that is carried by turbulent eddies. In this case, $\mathbb{E}\left[u_z' q'\right]$ represents the mean flux of humidity that is carried upwards in turbulent eddies. It is possible to derive another set of equations for the covariance quantities like $\mathbb{E}\left[u_z' q'\right]$; however, doing this produces equations that depend on unknown *third order* combinations of the perturbations. In general, the equations for the k^{th} order statistics of the unknown atmospheric quantities involves an expression in the $(k+1)^{\text{th}}$ order statistics. This is known as the turbulence closure problem. To "close" the set of unknowns, the equations are written up to k^{th} order, and the $(k+1)^{\text{th}}$ order terms are approximated or *parameterized* in terms of quantities derivable from the lower order terms.

One such first order closure is derived by observing that if the covariances have the interpretation of the flux of a quantity, then perhaps they obey a diffusion-like equation depending on the mean quantities. It is then postulated that the spatial gradient of the mean quantity drives the flux. Under this postulate, the humidity-flux is given by

$$\mathbb{E}\left[u_z' q'\right] = K_W \frac{\partial q}{\partial z}, \tag{52}$$

where the quantity K_W is an eddy diffusivity for water vapor. The diffusion parameter K_W is not a constant property of the fluid, but can be a function of the flow velocity or position in the flow [119]. The following series of assumptions and approximations is required to derive a form for the diffusivity and solve Equation 52.

- Near the ground, the humidity flux is approximately constant in height, and will be approximated by it's surface value, $\mathbb{E}\left[u_z' q'\right] \approx q_* u_*$, where $u_* = \sqrt{-\mathbb{E}\left[u_x' u_z'\right]}$ (evaluated at the surface) is the *surface friction velocity* and $q_* = \mathbb{E}\left[u_z' q'\right] / \sqrt{-\mathbb{E}\left[u_x' u_z'\right]}$ is a constant also evaluated at the surface.

- The diffusion parameter in turbulent eddies should be proportional to the size of the eddy. Very near the ground, the eddy size is limited by it's proximity to the ground. This is depicted in Figure 31. This result is known as Prandtl's mixing length hypothesis and the result is that $K_W \sim z$. The constant of proportionality is denoted k, and is known as the von Kármán constant.

- From dimensional arguments, the diffusivity should also be proportional to the surface friction velocity ($K_W \sim u_*$).

- The above give that $K_W \sim u_* k z$; any additional height dependence of the diffusivity K_W is accounted for by a postulated dimensionless factor, $\Phi_W\left(\frac{z}{L}\right)$, where L is a characteristic length that is a function of the first order terms and the parameterized covariance terms. Combining all of the above, the eddy diffusivity of water vapor is given by $K_W = u_* k z / \Phi_W\left(\frac{z}{L}\right)$

Plugging the diffusivity that results from the above list of assumptions into the flux-gradient relationship of Equation 52 gives

$$\frac{\partial q}{\partial z} = \frac{q_*}{kz} \Phi_W\left(\frac{z}{L}\right). \tag{53}$$

This equation is part of the *Monin-Obukhov similarity theory*, and the function Φ_W is known as the universal-function or stability function for humidity. The left hand side is a local

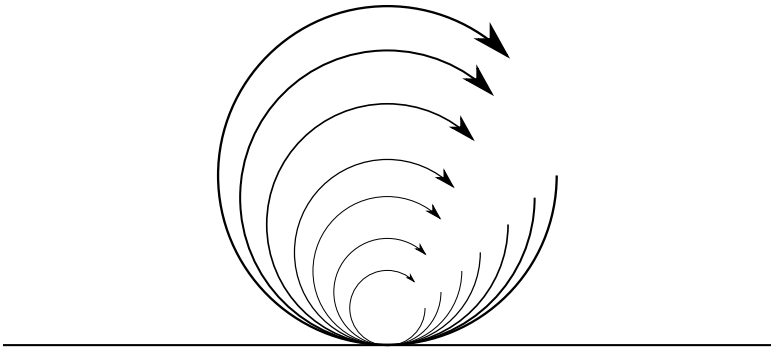

Figure 31: Illustration of how the eddy size is limited by proximity to the surface. The lines represent the flow of circulating eddies. The ones closest to the ground cannot be larger than their distance to the ground, meaning that the eddy size or mixing length must scale proportionally to height z.

gradient in height z of the quantity q, while the right hand side contains a term that is proportional to the humidity flux. The accepted empirical form of the universal function $\Phi_W(\zeta)$ according to [119] is

$$\Phi_W(\zeta) = \begin{cases} 1 + \beta_1 \zeta & , \quad 0 < \zeta \leq 1 \\ (1 - \gamma_2 \zeta)^{-1/2} & , \quad -5 < \zeta \leq 0 \end{cases}, \tag{54}$$

for constants $\beta_1 = 5,\ \gamma_2 = 16$, empirically determined from experiments [119]. The linear first order ODE of Eq. 53 can be solved by integration, after inserting the functional form of Eq. 54. The solution is

$$q(z) = \frac{q_*}{k}\left(\ln\left(\frac{z}{z_q}\right) - \Psi_W\left(\frac{z}{L}\right)\right) \tag{55}$$

where z_q is a constant of integration and the function $\Psi_W(\zeta)$ is the following integral of $\Phi_W(\zeta)$

$$\Psi_W(\zeta) = \int_0^\zeta \frac{1 - \Phi_W(\zeta')}{\zeta'} d\zeta' = \begin{cases} -\beta_1 \zeta & , \quad 0 < \zeta \leq 1 \\ 2\ln\left(\dfrac{1 + \sqrt{1 - \gamma_2 \zeta}}{2}\right) & , \quad -5 < \zeta \leq 0 \end{cases} \tag{56}$$

When $L > 0$, the atmosphere is called *stable*, and Equation 55 simplifies to

$$q(z) = -\frac{q_*}{k}\ln(z_q) + \frac{q_*}{k}\ln(z) + \frac{q_* \beta_1}{kL} z. \tag{57}$$

After grouping the associated constants together as new variables, this is written in a general form as

$$q(z) = A + B\ln(z) + Cz. \tag{58}$$

During *unstable* conditions when $L < 0$, Equation 55 becomes

$$q(z) = \frac{q_*}{k}\left(\ln\left(\frac{z}{z_q}\right) - 2\ln\left(\frac{1+\sqrt{1-\gamma_2\frac{z}{L}}}{2}\right)\right)$$

$$q(z) = \left(-\frac{q_*}{k}\ln(z_q) + 2\frac{q_*}{k}\ln(2)\right) + \frac{q_*}{k}\left(\ln(z) - 2\ln\left(1+\sqrt{1-\gamma_2\frac{z}{L}}\right)\right)$$

Grouping the associated constants together as new variables gives the general form

$$q(z) = A + B\ln(z) - 2B\ln\left(1+\sqrt{1-Cz}\right). \tag{59}$$

Together, the forms of Equations 58 and 59 provide the fit-functions for the average specific humidity as a function of height. The measured data are time-averaged over a time period that corresponds to a local measure of time correlation. After "averaging out" the turbulence, what remains are average profiles of humidity. The two functional forms of Equations 58 and 59 are fitted to the measured height profiles for the constants (A, B, C). The fit that gives the smaller root-mean-squared error (RMSE) when compared with the measurements is chosen as the profile that best fits the data. Given this, we can immediately determine if the conditions were stable or unstable. In the process, we recover a best-fit profile of humidity in the Monin-Obukhov theory.

A similar line of reasoning applies to the temperature profile. The Monin-Obukhov theory applies to the the potential temperature θ, which is related to the absolute temperature through

$$\theta = T\left(\frac{P_0}{P}\right)^{R/C_p},$$

where T is the absolute temperature, P_0 is a reference pressure, P is the actual pressure, R is the specific gas constant of air, and C_p is the specific heat capacity of air at constant pressure. The potential temperature obeys a flux-gradient equation of the form

$$\frac{\partial\theta}{\partial z} = \frac{\theta_*}{kz}\Phi_H\left(\frac{z}{L}\right). \tag{60}$$

Since only the first few meters above the ground are of interest, the pressure profile with height is practically constant. Taking this as an approximation, the absolute temperature obeys a similar equation

$$\frac{\partial T}{\partial z} = \frac{T_*}{kz}\Phi_H\left(\frac{z}{L}\right), \tag{61}$$

with $T_* = \theta_*(P/P_0)^{R/C_p}$. This equation can be integrated analogously to the previous derivation for q, giving the result

$$T(z) = \frac{T_*}{k}\left(\ln\left(\frac{z}{z_T}\right) - \Psi_H\left(\frac{z}{L}\right)\right) \tag{62}$$

Finally, the universal function for heat, Φ_H, and it's integral, Ψ_H, are equivalent to their humidity counterparts, Φ_W and Ψ_W, according to both observations and theoretical considerations ([119] p.54). Given this fact, the temperature profile takes the exact same form as Equations 58 and 59. To recapitulate then, the temperature and humidity profiles will both take the same form,

$$q(z), T(z) \sim \begin{cases} A + B\ln(z) + Cz & , \quad \text{stable} \\ A + B\ln(z) - 2B\ln\left(1 + \sqrt{1 - Cz}\right) & , \quad \text{unstable.} \end{cases} \tag{63}$$

Equation 63 serves as the fit-function that is used to determine the best-fit continuous profiles of humidity and temperature for the measured data. The full expression in Equation 63 is an original development; however, the portion of the expression corresponding to a sable atmosphere has appeared in the meteorological literature [121].

3.5.2 Examining the Fitted Profiles

The time-averaged temperature and humidity profiles were fit to the three parameter model of Equation 63. A random selection of 8 averaged humidity profiles and fits is presented in Figure 32. After averaging the data in 30 second blocks, a total of 1776 humidity and temperature profiles resulted, whereas only 8 of these are visualized in Figure 32. To visualize how the fitted curves compare to the measured temperature and humidity across all 1776 averaged observations, the RMSE of the fitted curves is plotted against the mean

time at which the profile was observed in Figure 33. The RMS error in the profiles is seen to be less than 1.6 percentage points of relative humidity across all observations.

A selection of 8 averaged temperature profiles and fits is presented in Figure 34, taken from the same observations as the humidity profiles from Figure 32. The RMSE in the fitted curves across all the averaged observations is presented in Figure 35. The RMS error in the temperature profiles is seen to be less than 0.64 °C across all observations, with a markedly smaller upper bound of 0.25 °C for times prior to 13:00 UTC. This corresponds to sunrise in Panama City, at which time the atmosphere becomes more turbulent. It is possible that during the daylight hours, the chosen 30 second averaging interval is not reflective of the turbulence time-scale. A future analysis would be to separate the data into two sets, one during hours with sunlight, and one during dark hours. Then the turbulence time-scales could be calculated separately for dark and light using the autocorrelation ideas presented in Section 3.4.1. Using a single averaging time-scale for the entire experiment, during both light and dark hours, is a potential limitation or error source for the analysis presented in this chapter.

There is also an offset between the measurements and the fit lines that bears mention. The second sensor up from ground level appears to be systematically off the fit lines in a way that stands out under visual inspection of the profiles, in both humidity and temperature. Plots of the humidity fit error vs. time at the various sensor heights in Figure 36 demonstrates this effect. The 18 cm green trace in that plot has a typical error value of $\sim 1.25\%$ relative humidity during the dark hours prior to 13:00 UTC, while the other traces are typically in error of less than $\sim 0.5\%$ relative humidity over the same period of time. There are several possible explanations for this discrepancy. A calibration error in the second temperature/humidity sensor might explain the discrepancy. However, the offset from the fit line is not constant in time. That is, during the dark hours, the fit line overestimates the humidity, and during the hours of sunlight, it underestimates the humidity. One might expect a calibration error to not vary in time or with the amplitude of the sensor input.

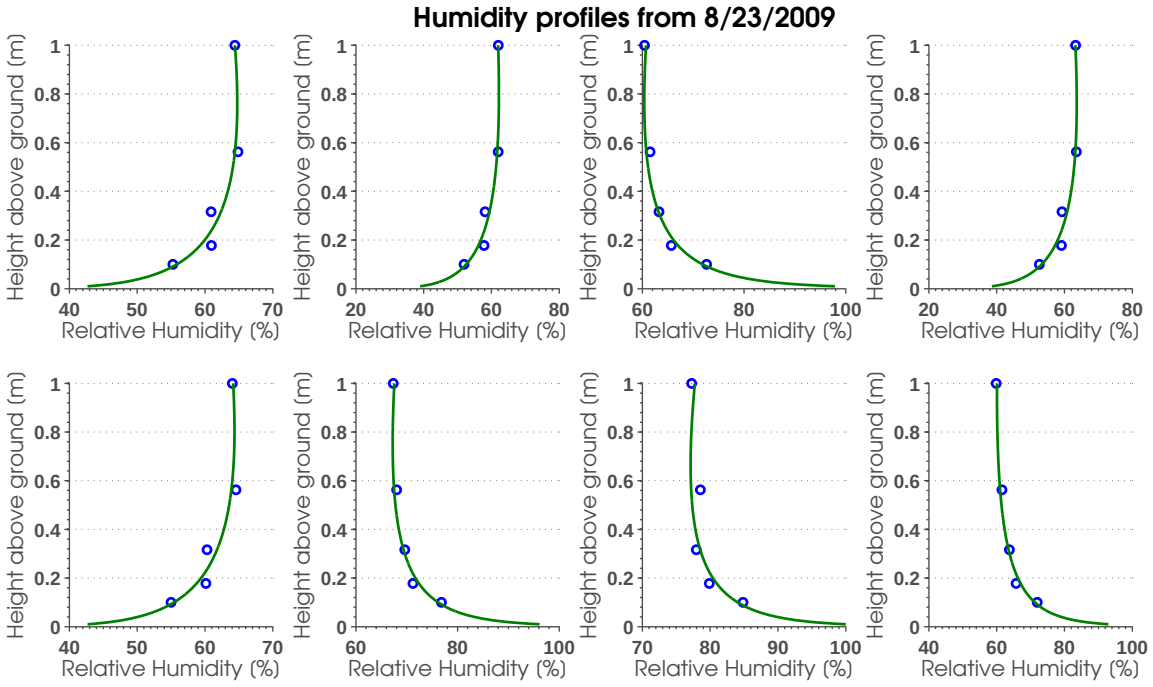

Figure 32: The time-averaged relative humidity vs. height profiles, both measured values (○) and Equation 63 fits (–)

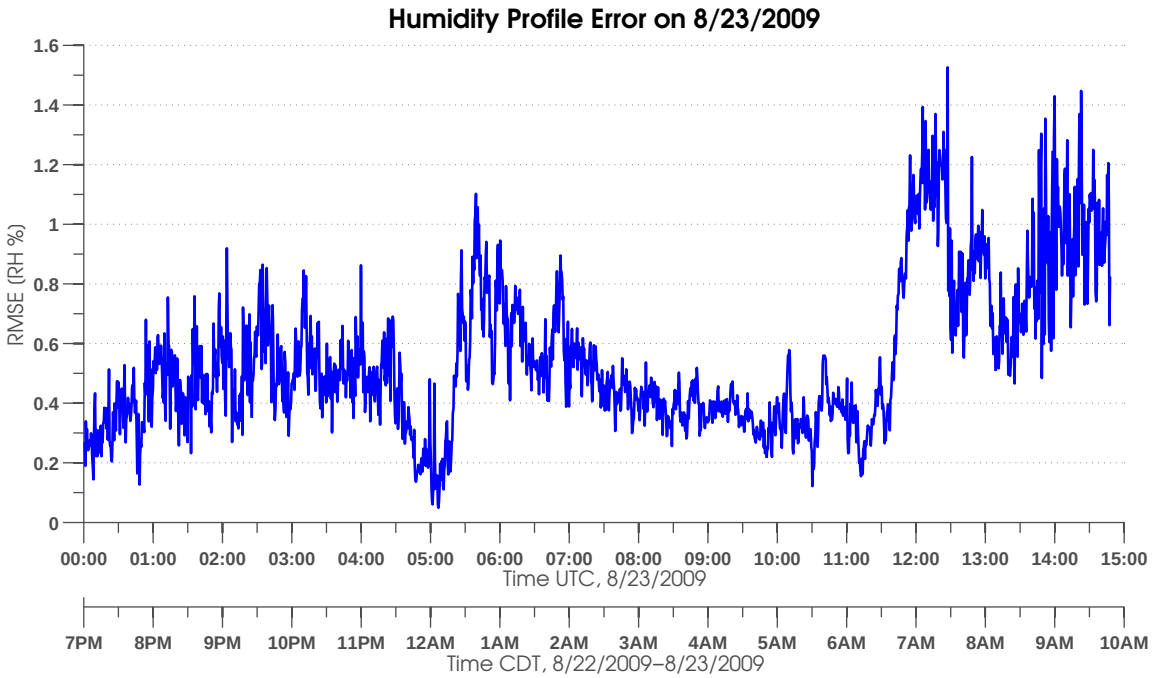

Figure 33: Humidity profile fit errors for 8/23/2009

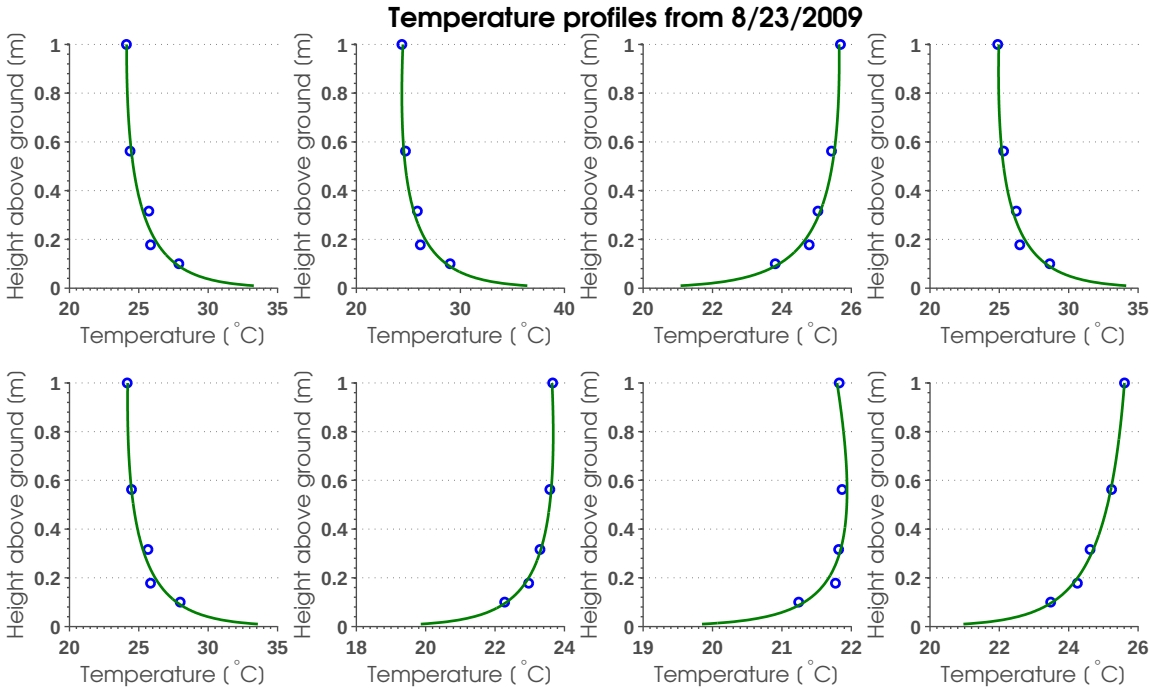

Figure 34: The time-averaged temperature vs. height profiles, both measured values (○) and Equation 63 fits (–)

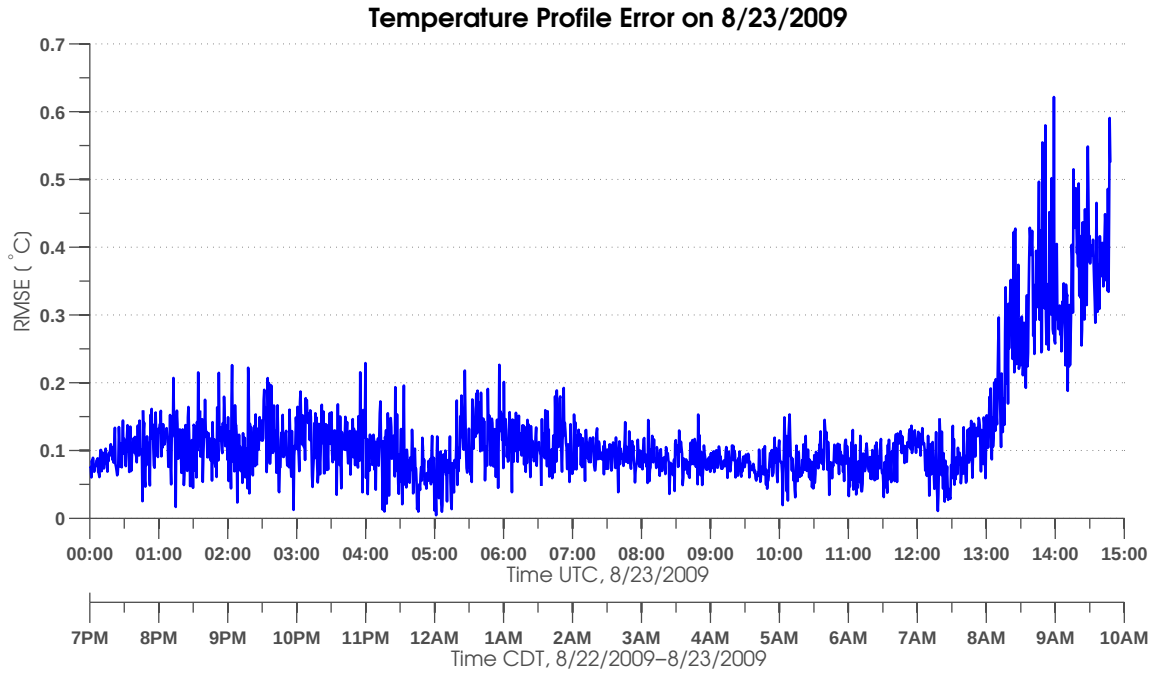

Figure 35: Temperature profile fit errors for 8/23/2009

Certainly, one would not expect the effect of mis-calibration to change from a negative to a positive offset. A calibration error is unlikely to explain the observed offset. Another possibility is that there are some physical effects not captured by the Monin-Obukhov theory used. Given the complex nature of turbulence and the limited developments of atmospheric theory in this chapter, this possibility cannot be ruled out. A third possibility is that the sensor height value of 17.8 cm was incorrectly recorded. Looking at the 18 cm point in Figures 32 and 34, one can imagine that if the point were to retain its temperature or humidity value but be "nudged" upwards in height to 22 cm or perhaps 24 cm, then the fit line and measurements would be closer together in every case. Given that the sensor units themselves are perhaps 10 cm in height, it is possible that the height for this particular unit was recorded in a way inconsistent with the others. For example, perhaps the other units were measured from ground level to the center of the sensor, while sensor 2 was measured from ground level to the bottom of the sensor. In the hectic environment of an experimental campaign, such an error or imprecise recording of a sensor height could certainly be made, and explains the observed deviation quite well.

3.6 RF Simulation Results

Having mapped the collection of time-averaged, 5-point temperature and humidity measurements to continuous curves of the form of Equation 63, these continuous curves were again discretized on 500 heights between 1 cm and 100 cm. Using these smoothed and extrapolated atmospheric profiles, Equation 1 was used to calculate a set of 500-point refractivity profiles, which represent a 500-layer refractive "stackup" of the type depicted previously in Figure 10. Measurements of the ground conditions of the Panama City experimental site, including soil conductivity and dielectric constant, were not collected. A typical value of the ground dielectric constant from [25], of $\varepsilon_r = n^2 = 15 + 0.09j$, was used for the dielectric value of the bottom layer of the dielectric structure. Dielectric constants in this range have also been reported at UHF frequencies for wet soils across a broad range of

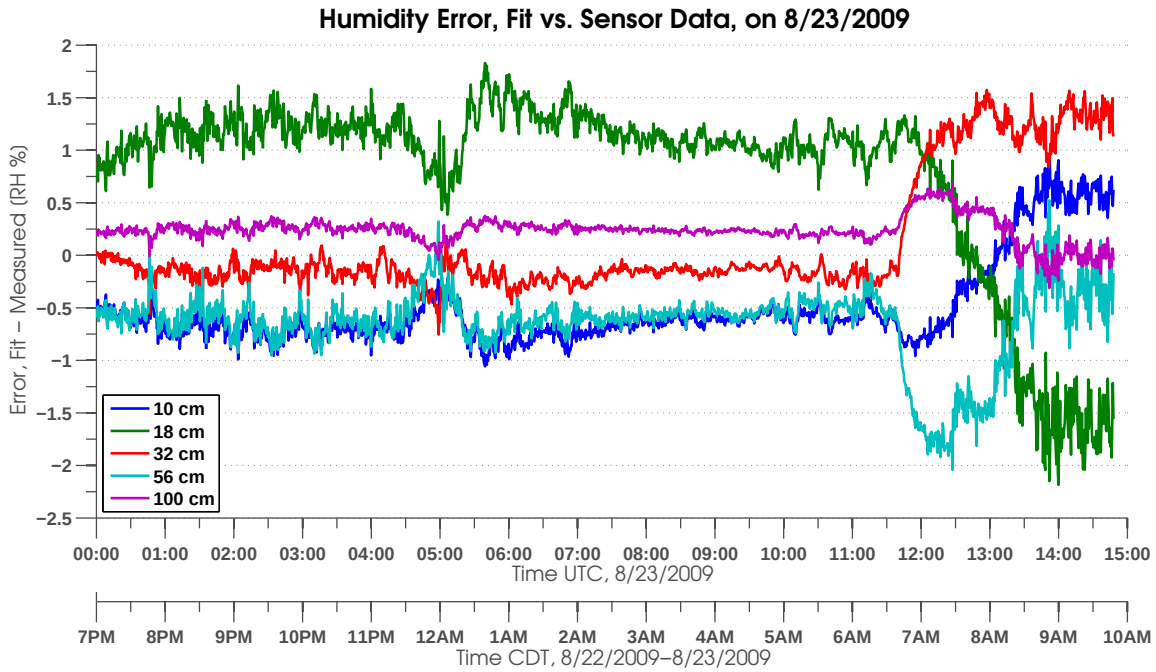

Figure 36: Error between humidity measurements and fit values over time. Note that the 18cm sensor exhibits larger and more systematic errors than the other sensors.

textures [122]. The assumption of a wet soil is also consistent with the rain events observed in Panama City on 8/18/2009, 8/20/2009, and 8/21/2009, which were the days leading up to the measurements. This dielectric soil is combined with a total of 1776 refractive profiles that were then serially simulated using the EM solver developed in Chapter 2. A short dipole was placed in the simulation at a height of 90 cm above a flat surface, corresponding to the height of the transmit antenna from the experimental setup. The simulation frequency was set to 1.78 GHz as well, which is the same as the transmit frequency used during the experimental campaign. The EM fields for a 1 W transmitter were calculated on a grid of points from the source out to 70 m of range, and heights ranging from 0.83 m below the surface to 1.82 m above the surface. These values correspond to 5 wavelengths into the ground and 5 wavelengths past the 1 m point. An example of power contours in space resulting from the simulation is presented in Figure 37.

The contour plots that resulted from each of the 1776 simulated profiles is omitted for space considerations. What is of primary interest is power level fluctuations at a single

receiver position located 70 m from the transmitter ($\approx 415\lambda_0$) and at 90 cm of height ($\approx 5.3\lambda_0$), corresponding to the receiver position in the experiments. A plot of the simulated power level at this position over time is presented in Figure 38.

Figure 38 demonstrates that the received power does indeed fluctuate as the atmospheric conditions vary in the simulation. Of note however is the scale of plot amplitude, which varies by only several hundredths of a dB. The minimum and maximum simulated power levels over the course of the 15 hour period are within 0.025 dB of each other. The level of fluctuation is of course also within the margin of error of the SI technique of Chapter 2, which was demonstrated to be accurate to approximately 0.4 dB in the worst case. Nonetheless, the measurement results of Figure 26 fluctuate by several dB over the same period. If the measured fluctuations of several dB were due to refractive effects in the channel, then the SI technique of Chapter 2 would have resolved several dB of fluctuation, within a 0.4 dB margin of error.

3.7 Interpretation of Results and Discussion

The results of a combined atmospheric and electromagnetic model have been compared to measured data. After accounting for the antenna gains of the various receive antennas, the model predictions are within 1 dB of the average of the measurements. Given that the soil conditions were approximated by a typical representative value the dielectric constant for soil, this is an acceptable level of precision. However, the measured RF data include periods of several dB of received signal fluctuations, and this behavior is not predicted by the model. In other words, if the implementation of the electromagnetic model of Chapter 2 and the atmospheric Monin-Obukhov theory is correct, then the fluctuations in the received signal strength cannot be attributed to refractive effects in the channel in this experiment. Given that both the EM and atmospheric models are based on sound physical principles, we can say with some certainty that near-earth refractive effects were not a factor in the propagation environment in this experiment.

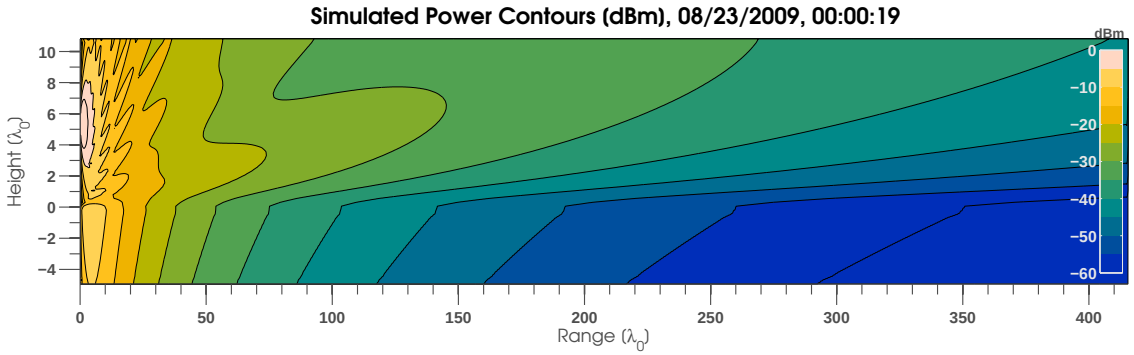

Figure 37: An example of simulated RF power on 8/23/2009. Power on a grid of range-height points was calculated, and then processed into contours in 5 dB increments.

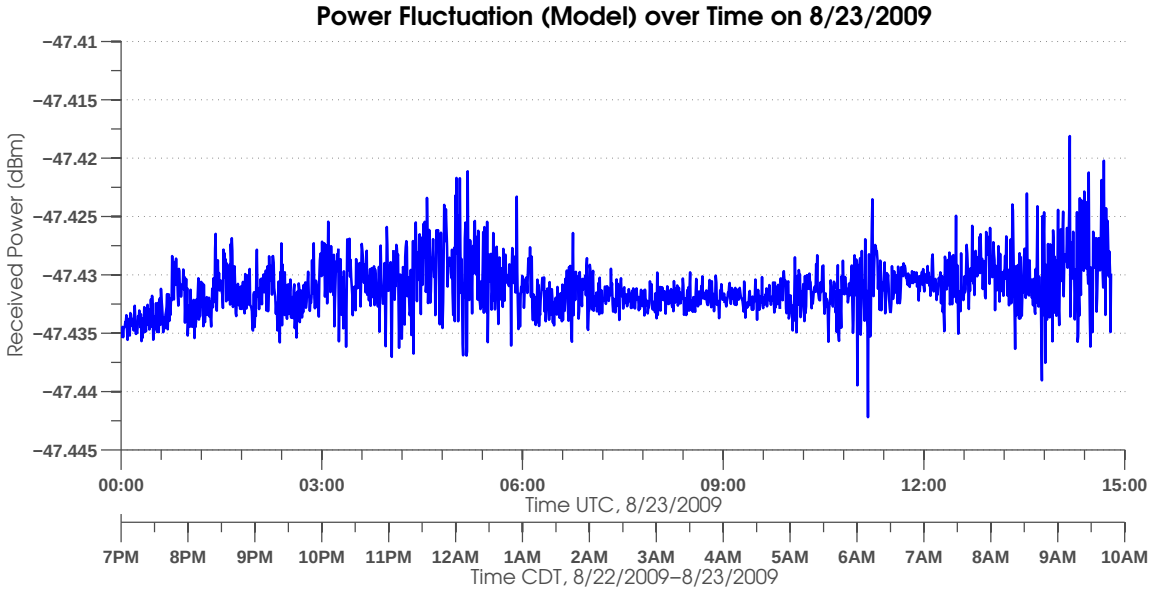

Figure 38: Simulated RF power at 70 m on 8/23/2009.

Understanding what *did* cause several dB of signal strength fluctuations in the experiment is difficult. This is because there is a lack of other information about the area surrounding the experiment while it was being conducted. It is possible that other unconsidered environmental factors caused the periods of fluctuation. For example, a large metal scatterer such as a vehicle driving in the vicinity of the experiments could plausibly cause several dB of signal fluctuation due to multipath effects in the narrowband channel. Animals such as deer or birds could have entered into the measurement area, touching the equipment or otherwise affecting the results. The site was not instrumented with sensors to detect this kind of activity. Another possibility is that some other RF system was operating in the band of the measurement. In narrowband measurements of the type used in this experiment, it is impossible to differentiate between in-band transmissions from the intended source, and those from other transmitters in the vicinity of the experiment. In short, the possibilities for what caused the fluctuations are endless, but one thing can be said with some certainty: the observed near-earth refractive conditions are simply not strong enough to cause signal variations of several dB, over distances of 70 m, for systems operating at 1.78 GHz near the earth-surface.

CHAPTER 4

REFRACTIVE CONDITIONS AND EFFECTS ON LONG RANGE PROPAGATION

Chapter Summary: The concept of refractive gain is introduced, which is an effective gain attributable to refractive effects in a channel. This gain is examined for a measured refractive profile from the previous chapter, where it is found to take a relatively small value. Refractive profiles with a stronger gradient are examined in detail, using a mathematical gradient-amplification technique, followed by an analysis linking gradient-amplification to physical conditions. The effects of ground conductivity and frequency are also explored. Larger levels of gradient-amplification, higher ground conductivity, and higher frequencies are all found to increase the magnitude of refractive effects in the near-ground channel.

4.1 Introduction

The previous chapter demonstrated that refractive effects are likely not the cause of several dB of power fluctuations near the ground in a location in Panama City, FL on 8/23/09. However, in general cases at other locations and other times, the propagation effects must be accurately known for the design of near-ground radio links. The model of Chapter 2 provides a way to study these effects through simulation. This chapter investigates the kinds of refractive and ground conditions that do cause significant power propagation effects. The baseline for comparisons when determining significance of refractive effects is the *gradient-free* case. This is a simple propagation environment consisting of a half-space of homogeneous air above a lossy dielectric half-space of ground. The corresponding refractive gradient case is an environment that has multiple layers of dielectric representing the air, and the same lossy dielectric half-space representing the ground. To compare the refractive gradient and gradient-free cases, a quantity called the *refractive gain* is defined

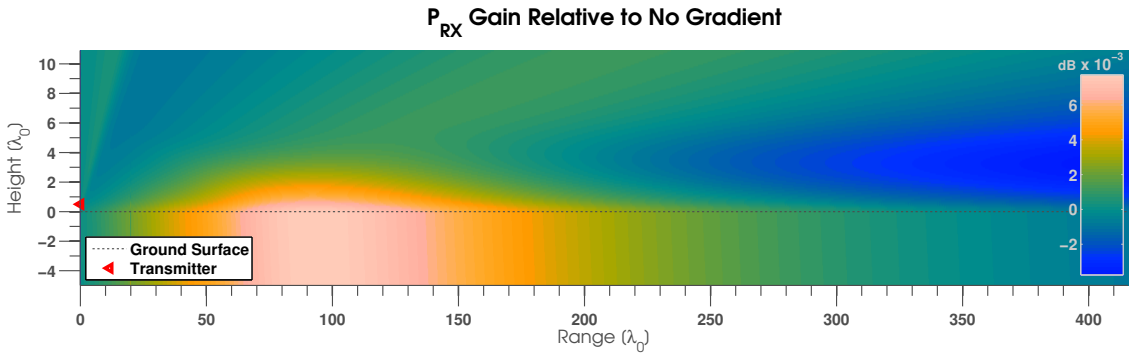

Figure 39: The ratio of the received power between refractive and non-refractive cases is visualized in decibels, as a function of range from the transmitter and height above ground level.

as a ratio of the powers in the two cases. The ratio can be expressed as

$$G_{\text{refract}} = \frac{P_{RX}|_{\text{refractive-atmosphere}}}{P_{RX}|_{\text{no-refractive-atmosphere}}}, \tag{64}$$

where P_{RX} is the power received by an isotropic antenna, the numerator is calculated in the presence of an atmospheric-gradient refractivity profile, the denominator is calculated in the presence of a free-space atmosphere, and both quantities are with respect to a transmitter at the same height and identical ground conditions. In this chapter, the refractive gain will typically appear in decibel units of $10\log_{10}(G_{\text{refract}})$. Decibel refractive-gain can be interpreted as the power gain that is attributable to refractive effects in a channel.

4.2 Refractive-Gain in Measured Conditions

The refractive-gain for a time-averaged atmospheric profile of humidity and temperature measured on 8/23/09 in Panama City, FL during the data collection described in Chapter 3 is presented in Figure 39. Physically motivated functions for the temperature and humidity (derived from the Monin-Obukhov theory) were fit to the measured five-point temperature and humidity profiles, using the same methodology as in Chapter 3. Smooth atmospheric refractivity profiles were calculated from the fitted curves.

In the region close to the ground and around range $100\lambda_0$, there is clearly more power in the presence of the simulated refractive structure when compared to the available power

in the presence of no atmospheric refractive gradient. There is also correspondingly *less* power available at ranges farther to the right of the plot. The additional gain near ground level and closer to the transmitter is of the same order and opposite sign as the additional loss in received power farther away from the transmitter. Thus the effect of the refractive structure is to shift or focus power away from some regions and into others. However, the range of colors in this plot represents deviations of less than 0.01dB. For practical engineering purposes, this deviation in received power is negligible compared to other uncertainties caused by the effects of noise, environmental uncertainty, etc. This reiterates the primary result of the previous chapter, which is that certain natural refractive atmospheric effects near the surface induce very small deviations in the signal strength.

It has been demonstrated that some natural atmospheric refractive gradients outdoors do not cause considerable effects in the available power in the fields of a short dipole radiator. For practical purposes of power-budget analysis of a communications system or link design, one might wonder if near-earth atmospheric effects play any role at all, under any conditions. To begin to answer these questions, consider a hypothetical *amplification* of the refractive gradient near the surface of the earth. The refractive values at the various heights are scaled and shifted such that the refractive gradient is larger at every height, but the qualitative shape of the profile is preserved. If the minimal value of the refractive profile is 1, then the transformation

$$n(z) \rightarrow (n(z) - 1)\alpha + 1 \tag{65}$$

will amplify the refractive gradient, $\frac{\partial n}{\partial z}$, equally at every height by a multiplicative factor of α while preserving the the minimal, free-space value of the profile. The effects on EM propagation of such hypothetical, "stronger" refractive gradients can be simulated using the multilayer spectral domain method presented in Chapter 2. The results of such an analysis follow.

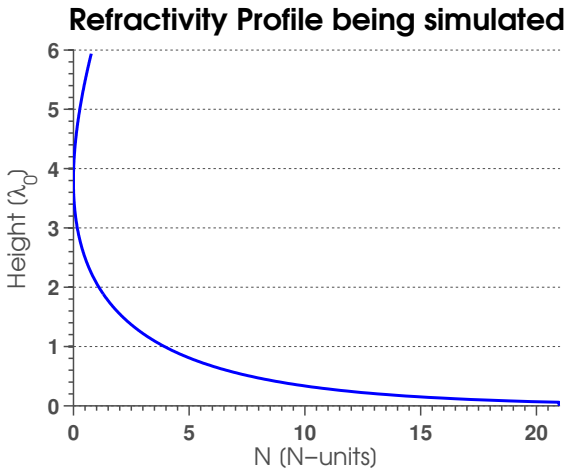

Figure 40: A Monin-Obukhov interpolated refractive profile, measured on 8/23/2009

4.3 Shape-preserving Atmospheric Gradient Amplification

Consider the refractive profile in Figure 40. Amplified refractive profiles derive from this base profile via the transformation in Equation 65 for various values of the amplification, α. Each amplified profile has the same shape as that of Figure 40, but is scaled such that $\left|\frac{\partial n}{\partial z}\right|$ is α times larger at all heights. The amplification parameters used in this study were $\alpha = 1, 5, 10, 50, 100, 500, 1000$. These values correspond to refractive gradients ranges that are the same as the naturally occurring measured profile, to ones that are up to 1000 times stronger. The refractive gain in the presence of increasingly amplified refractive gradients is presented in the series of Figures 41-46.

Figures 41, 42, 43, 44, 45, and 46 are visually, qualitatively identical to each other and to Figure 39. However, the color scale is different in each figure, indicating that the strength of the effect changes between figures while the shape of the refractive gain effect is similar between figures. All the figures exhibit a region of focused power near the surface of the ground and around $100\lambda_0$ of range. The difference among the figures is that the amount of power concentration is different, which is evident in the color scales in the plots. To demonstrate that the power concentration varies across the plots, the refractive gain at ground level is plotted for various values of the gradient strength in Figure 47.

Figure 47 demonstrates that the refractive gain along ground level, as a function of

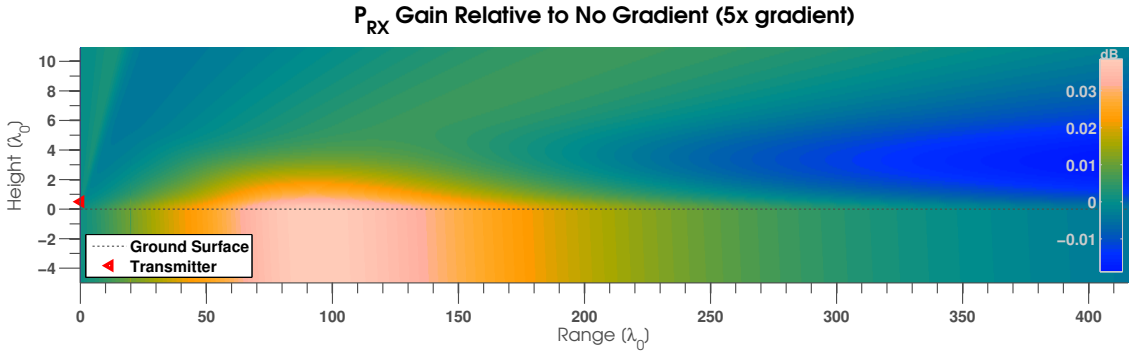

Figure 41: The ratio of the received power between refractive and non-refractive cases is visualized in deicbels, as a function of range from the transmitter and height above ground level.

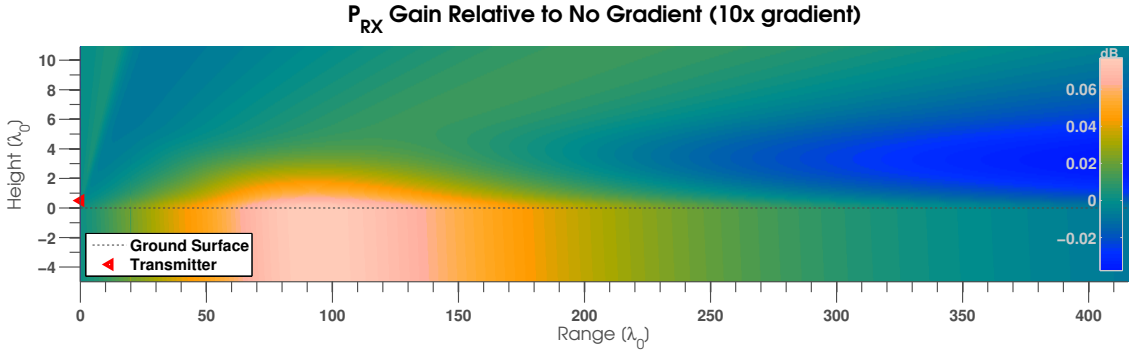

Figure 42: The ratio of the received power between refractive and non-refractive cases is visualized in deicbels, as a function of range from the transmitter and height above ground level.

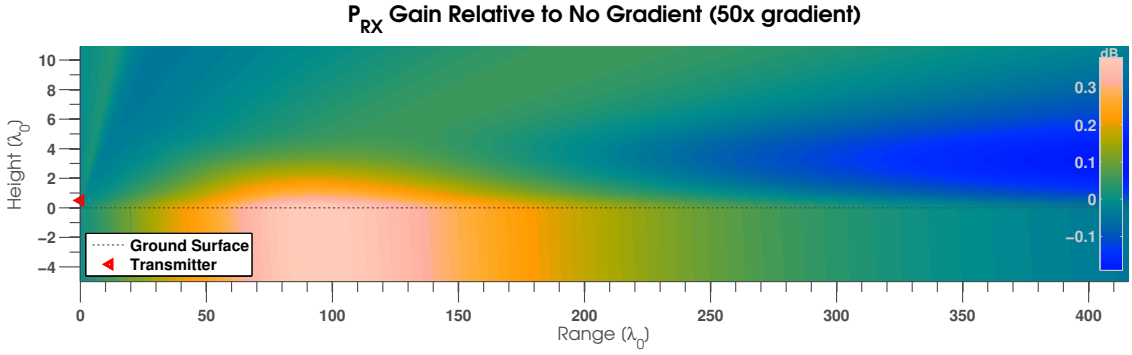

Figure 43: The ratio of the received power between refractive and non-refractive cases is visualized in deicbels, as a function of range from the transmitter and height above ground level.

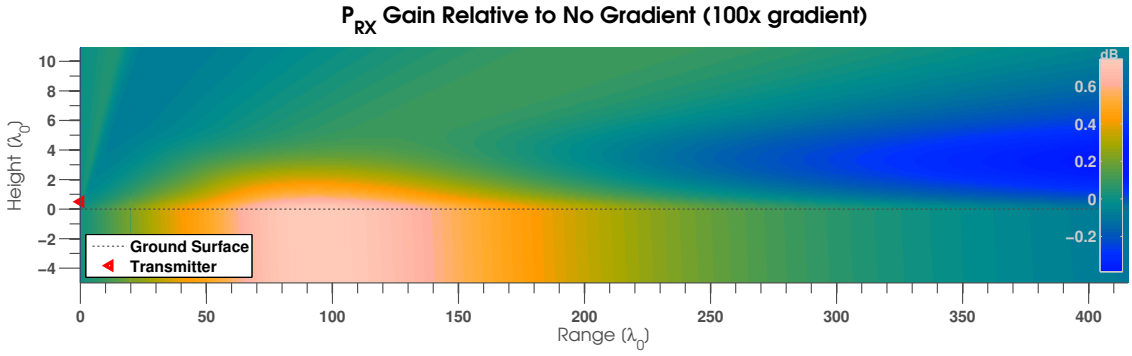

Figure 44: The ratio of the received power between refractive and non-refractive cases is visualized in deicbels, as a function of range from the transmitter and height above ground level.

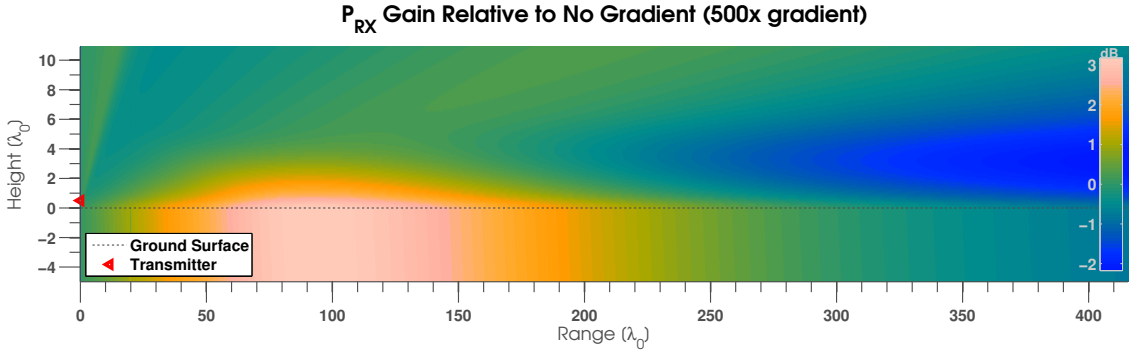

Figure 45: The ratio of the received power between refractive and non-refractive cases is visualized in deicbels, as a function of range from the transmitter and height above ground level.

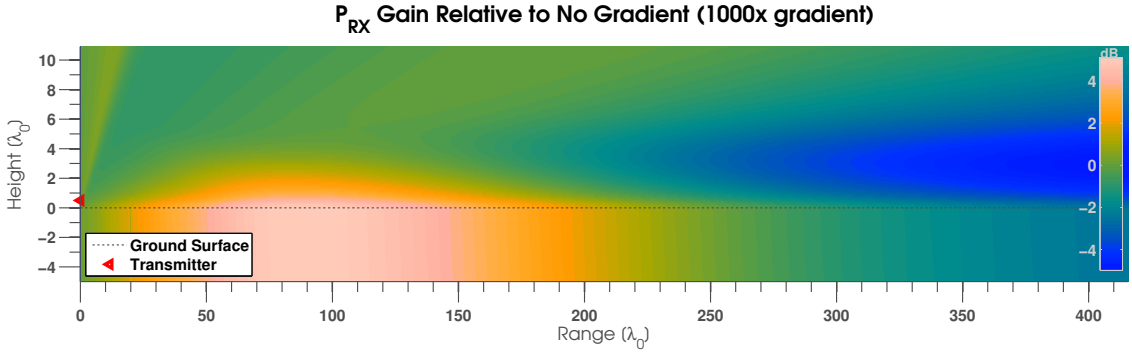

Figure 46: The ratio of the received power between refractive and non-refractive cases is visualized in deicbels, as a function of range from the transmitter and height above ground level.

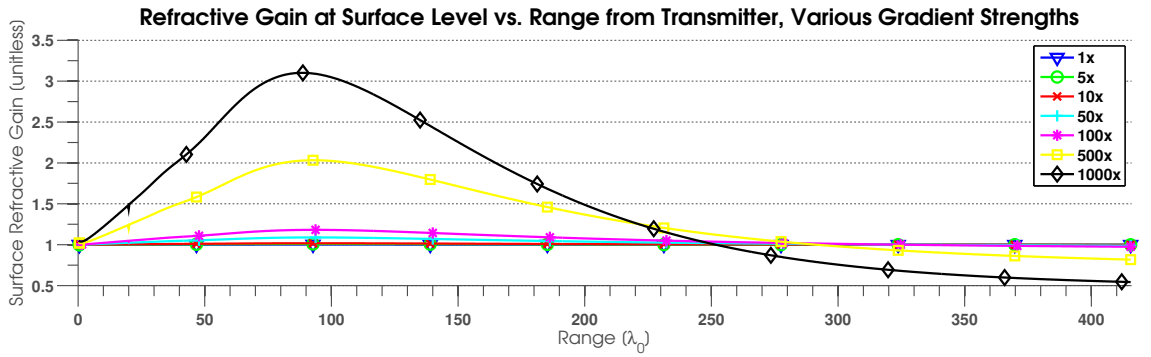

Figure 47: The linear refractive gain at ground level is plotted for the various values of the refractive gradient strength. As the gradient strength gets larger, the peak gain becomes larger.

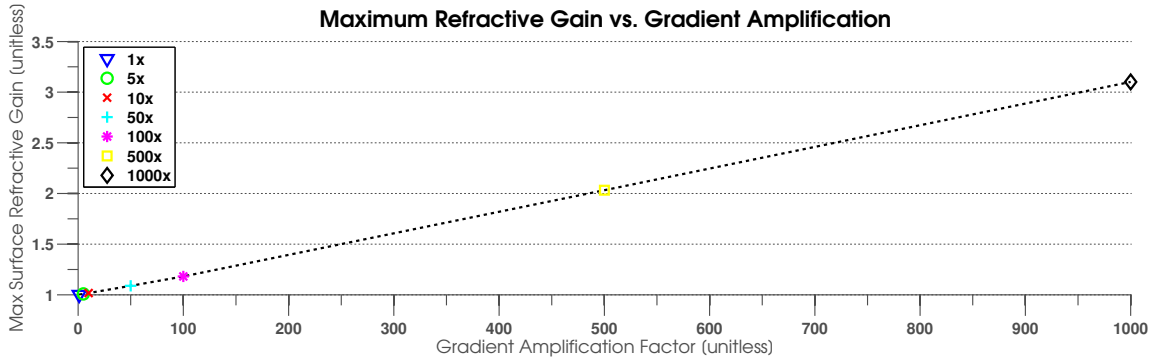

Figure 48: The maximum of the refractive gain at ground surface level is plotted for the various values of the refractive gradient strength. As the gradient strength gets larger, the peak gain becomes larger.

range, takes approximately the same shape irrespective of the gradient strength. The gain in the enhanced region increases with increasing gradient strength. The maximal refractive (linear) gain (as opposed to the decibel gain) near the surface of the earth increases approximately linearly with increasing gradient strength, as seen in Figure 48 . This linear relationship motivated the use of linear units in Figures 47 and 48.

Curves such as the one presented in Figure 48 can be useful in determining the refractive conditions under which "significant" power fluctuations or deviations occur, where the level that is considered significant is variable. If a near-earth communications system operates best when the received power uncertainty is less than 3dB, then a system designer does not need to consider refractive effects for gradients that are less than 500 times stronger than

a typical gradient observed in the Panama City, FL measurements. On the other hand, if a radio system can only tolerate deviations of 25% around a nominal expected power, then refractive effects should be considered in cases that correspond to only a 50x amplification of a typical measured refractive condition.

Another application of combined refractive/EM modeling would be to solve the inverse problem of sensing the environment from RF measurements. The SI method is a forward model that makes predictions of the RF signal given the atmospheric and ground conditions. An optimization method could be used to minimize the difference between the forward model and measurements, by iterating over physically reasonable atmospheric and ground conditions. The result of this optimization would the atmosphere and ground parameters that were likely to produce the measured results. Figure 48 could be used in this way directly: if several measurements of the RF signal were available along the ground level and the ground was known to have $\varepsilon_r = 15 + j0.09$, then the measured data could be compared to Figure 48 to determine which of the curves most closely approximates the measurements. Each curve maps to a level of gradient-amplification, so the corresponding refractive profile is effectively extracted from the RF data.

4.4 From Gradient Amplification to Physical Conditions

The method of Section 4.3 provides insight into the refractive conditions that lead to significant propagation effects. However, it does not provide insight into the *physical* atmospheric conditions that cause such refractive conditions. Amplifying a measured refractive gradient mathematically using Equation 65 does not directly determine atmospheric humidity and temperature profiles that cause such refractive conditions. For practical radio link design and planning, the physical conditions corresponding to specified refractive conditions must be known. Calculation of an inverse mapping from refractive conditions to atmospheric conditions is possible through a direct numerical search or optimization. It was previously demonstrated that the Monin-Obukhov theory leads to three-parameter models for both the

near-surface temperature and humidity profiles. The atmospheric refractivity profile depends directly on the temperature and humidity profiles; therefore, the refractivity profile depends on six parameters, $\boldsymbol{\theta} = (A_q, B_q, C_q, A_T, B_t, C_T)$, in addition to the height above ground, z. These parameters are the same ones that appeared in Equation 63, with q and T subscripts denoting the parameters for humidity and temperature, respectively. To find the six parameters that give a best fit to a given profile, a normalized error metric between the given refractive profile and the desired parametric fit function is defined as

$$E(\boldsymbol{\theta}) = \frac{\sum_i |N_{\text{fit}}(z_i|\boldsymbol{\theta}) - N(z_i)|^2}{\sum_i |N(z_i)|^2}, \tag{66}$$

where E is a normalized measure of the average squared-deviation across a discrete sequence of values z_i between the given refractive profile, N, and the fitting function, N_{fit}. If the error can be minimized over the six parameters, then an approximate physical situation that corresponds to a given refractive condition will be found. The problem of minimizing the error over the parameters can be concisely expressed as an optimization problem, which is to find the best-fit parameters $\hat{\boldsymbol{\theta}}$ such that

$$\hat{\boldsymbol{\theta}} = \underset{\boldsymbol{\theta}}{\operatorname{argmin}}\, E(\boldsymbol{\theta}). \tag{67}$$

The fit-function N_{fit} is a complicated non-linear function of the parameters, which can be seen by examining Equations 63 and 1. An additional non-linearity arises from the fact that the partial pressure of water vapor (e in Equation 1) is related to the absolute humidity (q in Equation 63) through a nonlinear function that also includes the temperature. Nonetheless, the forward model that gives N_{fit} for arbitrary parameters $\boldsymbol{\theta}$ and heights of interest z_i can be calculated. Thus, the error $E(\boldsymbol{\theta})$ can be calculated for any set of parameters $\boldsymbol{\theta}$ and target profile N. An iterative numerical procedure can then be used to minimize the error and solve the optimization problem of Equation 67. Such a numerical optimization was performed in the case of a refractive gradient 100x stronger than the one presented

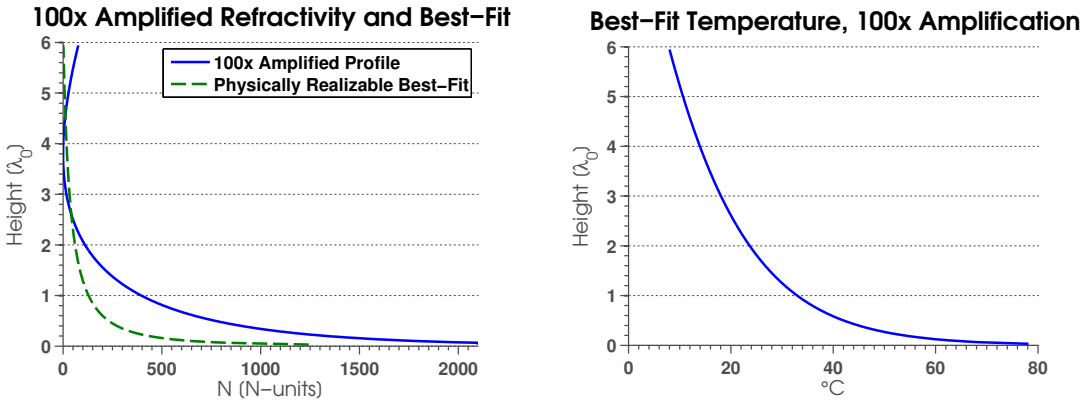

(a) 100x Amplified vs. Best-Fit N-Profiles.

(b) The corresponding temperature that gives the best-fit N profile appearing to the left.

Figure 49: A measured and interpolated refractive profile was mathematically amplified to 100x strength (left panel, [–]); the closest physically realizable profile shape was found using the Monin-Obukhov theory and curve fitting using Levenberg-Marquardt optimization (left panel, [- -]). The optimizer found a solution with 100% relative humidity at all heights, and a temperature profile given in the right panel. The best-fit N profile roughly captures the gradient and shape of the amplified profile, but the curves are not qualitatively very close to each other. This indicates that the amplified profile is unphysical.

in Figure 40. The method used was a MATLAB optimization routine implementing the Levenberg-Marquardt algorithm. The 100x gradient amplification level was chosen because it corresponds to a refractive gain of approximately 1dB according to Figure 48, which is an uncertainty level that is significant for practical applications. It should be noted that optimizers for non-linear problems can only find a local minimum in the error measure. Small perturbations of the parameters away from the found solution are guaranteed to not decrease the error; however, there may be other local minima in the error measure that have smaller error values. In the case that multiple minima exist in the error, the one that is found strongly depends on the details of the optimization algorithm and the initial guess to the iterative method. A single local minimum in the error was found by iteration from an initial guess of the parameters that corresponds to the originally measured temperature and humidity for the N profile in Figure 40. The refractive profile and temperature corresponding to the solution returned by the optimizer and the target 100x profile are plotted in Figure 49.

The physical atmospheric conditions that result in an N profile similar to the artificially amplified one are 1) that the temperature has the height dependence depicted in Figure 49b, and 2) that the relative humidity is a constant 100% for all heights. The temperature in Figure 49b ranges from 78.15 °C near the surface to 8.02 °C at the top measurement height of 1 m (recalling that $\lambda_0 \approx 16.84$ cm). In other words, in order to see atmospheric gradient strengths similar to ones that have a 1 dB effect on UHF propagation, the surface temperature should be approximately the hottest surface temperatures on earth over the years 2003-2009 [123], and the air temperature at 1 m needs to be that of a brisk fall day in the southeastern US. Those conditions should all occur in 100% relative humidity. Temperature differences of up to 50 °C between the land surface and 1.5 m air temperature measurements are possible in the summer months, and such conditions are known to occur in desert conditions with dry soils [123]. On the other hand, hot weather with 100% relative humidity typically occurs in swamplands, coastal regions, and rain forests across the tropical and mid latitudes [124]. Precisely determining if such desert/rain forest hybrid conditions can exist on earth is outside of the scope of this work, but the above apparent paradox makes it unlikely.

4.5 Propagation in Extremal Refractivity

Although the atmospheric conditions of Figure 49 likely do not occur on Earth naturally, it is of interest to compare the propagation effects between the artificially amplified refractivity and the closest physical one. The physically justifiable refractive profile is of a qualitatively different shape than the amplified profile from which it derives; whether this shape has markedly different effects on the UHF propagation is investigated in this section.

The physically realizable best-fit refractivity of Figure 49a (left panel [--]) was input into the model developed in Chapter 2. The other model inputs (frequency, ground conditions, and transmitter geometry) are identical to the previous calculations of this chapter: a dipole operating at 1.78 GHz radiates at a height of $\lambda_0/2$ over a half-space with relative

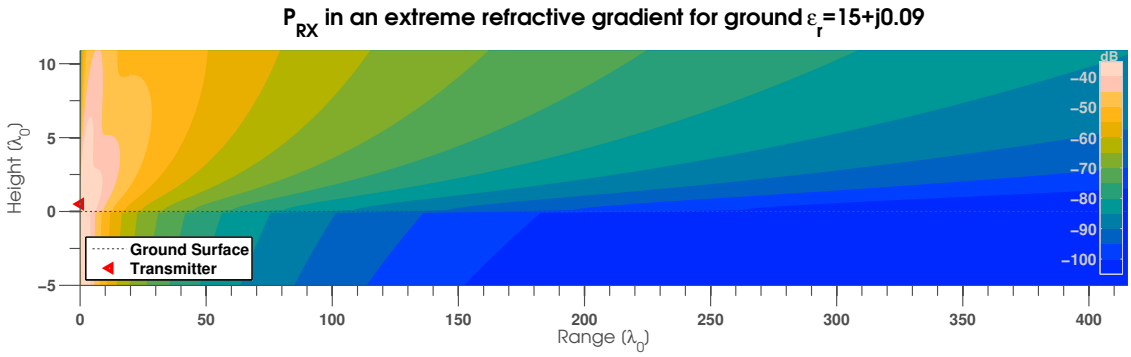

Figure 50: A short dipole operating at 1.78 GHz radiates at height $\lambda_0/2$ above a ground half-space with $\varepsilon_r = 15 + 0.09j$ in the presence of an extreme, but physically realizable refractivity gradient from Figure 49a. The temperature at the surface is approximately 78 °C, and the temperature at height $6\lambda_0$ (1 m) is approximately 8 °C. The total temperature variation is 70 °C per meter for the first meter above the ground. Contours of the power received by an isotropic receiver at various heights and ranges from the dipole are presented.

permittivity $\varepsilon_r = 15 + 0.09j$, where $\lambda_0 \approx 16.84$ cm is the wavelength of the electromagnetic fields in free-space. Plots of the refractive gain and the received power appear in Figures 50 and 51. The refractive gain in this case is qualitatively similar to the "100x gradient amplification" case from which it derives. Just as in the 100x amplification case, there is a region of enhanced power near the ground surface that is attributable to refractive effects, of the order of decibels. The differences are that the location of the maximal refractive gain has shifted outwards relative to the 100x amplification case, and the refractive gain is approximately half a decibel less than in the 100x amplification case.

4.6 Effect of Ground Conductivity

The analysis of Section 4.3 was conducted for a fixed ground dielectric constant of $\varepsilon_r = n^2 = 15 + 0.09j$, corresponding to a conductivity of $\sigma \approx 8.9$ mS/m at the simulation frequency of 1.78 GHz, and a "generally accepted" value for the real part of the dielectric constant [25]. This is the same value of the ground dielectric constant that was used in the experimental investigations for Panama City; the validity of that choice was discussed

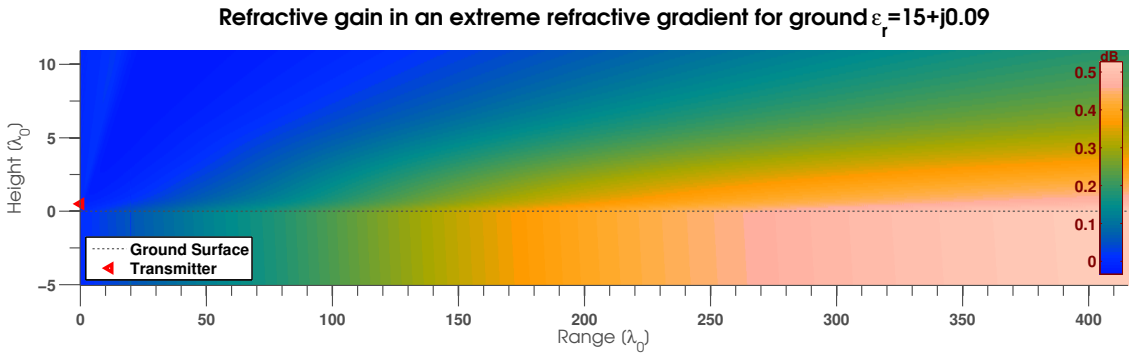

Figure 51: The refractive gain for the extreme but physically realizable refractive conditions is presented. The refractive structure focuses power in a region in the ground and near the ground surface. The maximal gain in this figure is approximately 0.53 dB.

previously in Section 3.6. The selected dielectric constant value is consistent with published measurements of wet sandy soils at UHF frequencies [122]. However, the dielectric properties of soil are highly dependent on a large number of parameters including excitation frequency, soil composition, soil particle size distribution, porosity, moisture content, density, temperature, and salinity. A variety of measurements and models for dielectric properties of soil have been presented in the literature [125, 126, 127, 128, 129], with varying degrees of complexity and fidelity. Accurately characterizing and modeling soil dielectric properties as a function of the aforementioned list of parameters is outside the scope of this work. However, refractive effects and effects due to soil dielectric properties are intimately linked together. This can be seen by noting that in Figures 41, 42, 43, 44, 45, and 46, power is concentrated to a large degree *in* the ground near the power-enhancement region. If the ground were to become more lossy and approach a good conductor, then no power concentration would be expected in the ground at all, since the fields would be essentially zero within a few skin-depths of the ground surface irrespective of the atmospheric conditions above the surface. This could mean that power would be concentrated in additional regions above the ground. It is possible that as the ground becomes more conductive, a proper "duct"-like environment could be set up, in which the refractive gradient and the lossy reflective surface form a waveguide.

A simulation study was carried out using the model of Chapter 2 in which the ground loss was varied over multiple runs of the model code, while the real dielectric constant, transmitter height, refractivity profile, and frequency remained constant. The refractivity profile was selected to be the one previously presented in Figure 40. The transmitter height, frequency, and real dielectric constant also remained the same as in the previous examples of Section 4.3. The full dielectric constant was $\varepsilon_r = 15 + j\varepsilon_r''$, where ε_r'' was varied over the values $\{0.01, 0.05, 0.1, 0.5, 1, 5, 10, 50, 100, 500, 1000\}$. The largest of these values is unlikely to be observed in real soils, since the primary contributing factor in natural soil conductivity is soil moisture content, and the imaginary part of the dielectric constant at these frequencies of pure sea water is $\varepsilon_r'' \approx 40$. However, to approach the good conductor limit, larger values of the imaginary part of the dielectric constant are considered. Figures 52-62 present the power contours in space as the ground conductivity is increased.

The received power contours change with increasing conductivity in the following ways. Less power is available inside the ground as the ground becomes more conductive. As less power penetrates the ground, more power is available in the air. The received power along the ground and near the right side of the above figures increases by approximately 30 dB across the figures as conductivity is increased, which can be seen by examining the color scale across the figures. Finally, the shape of the received power contours qualitatively changes across the figures. In particular, a deep angular null in the power pattern develops as conductivity increases. This is caused by the destructive interference between the waves incident from the dipole and those reflected from the ground. As the ground becomes more conductive, it becomes a more efficient reflector and the reflected waves retain more of their original amplitude. This leads to almost totally destructive interference in some regions, when compared to the less-conductive conditions in which the reflected fields lose much of their amplitude to transmission into the ground.

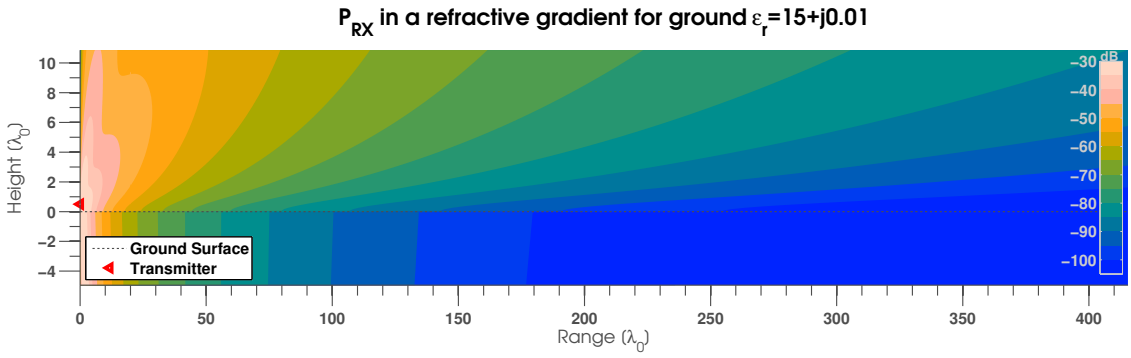

Figure 52: Received power contours for a transmitter at $z' = \lambda_0/2$ over ground with relative permittivity $\varepsilon_r = 15 + j0.01$. The refractivity above ground appears in Figure 40.

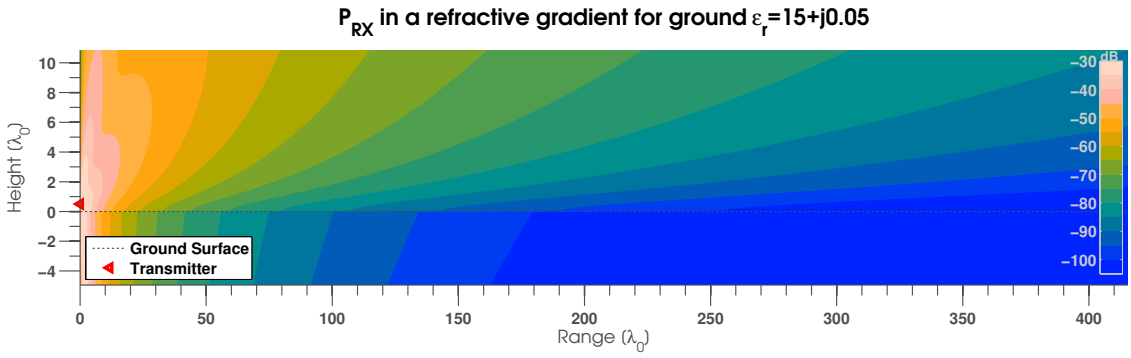

Figure 53: Received power contours in the scenario of Figure 52, with ground relative permittivity $\varepsilon_r = 15 + j0.05$.

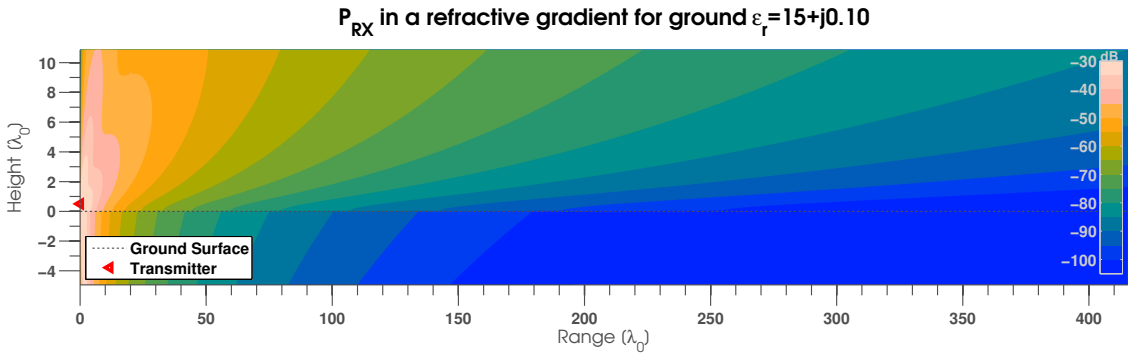

Figure 54: Received power contours in the scenario of Figure 52, with ground relative permittivity $\varepsilon_r = 15 + j0.1$.

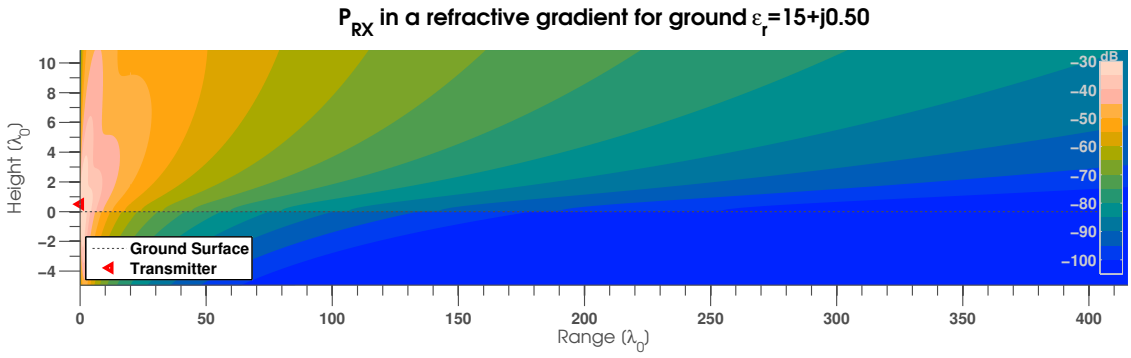

Figure 55: Received power contours in the scenario of Figure 52, with ground relative permittivity $\varepsilon_r = 15 + j0.5$.

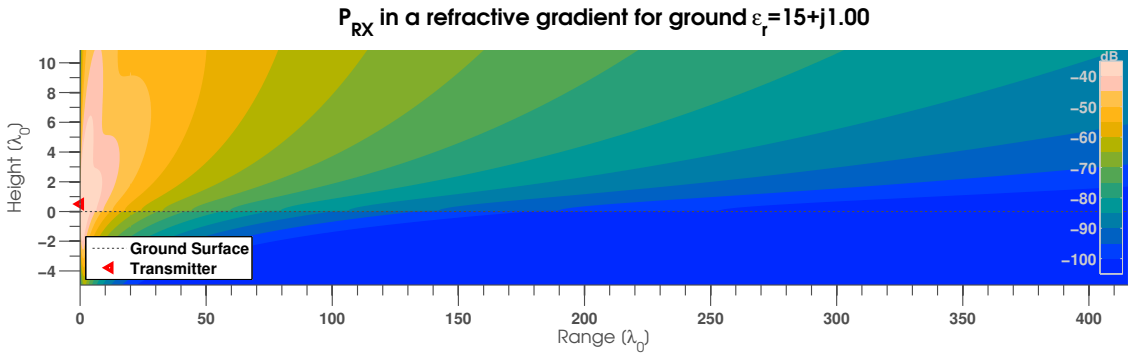

Figure 56: Received power contours in the scenario of Figure 52, with ground relative permittivity $\varepsilon_r = 15 + j1$.

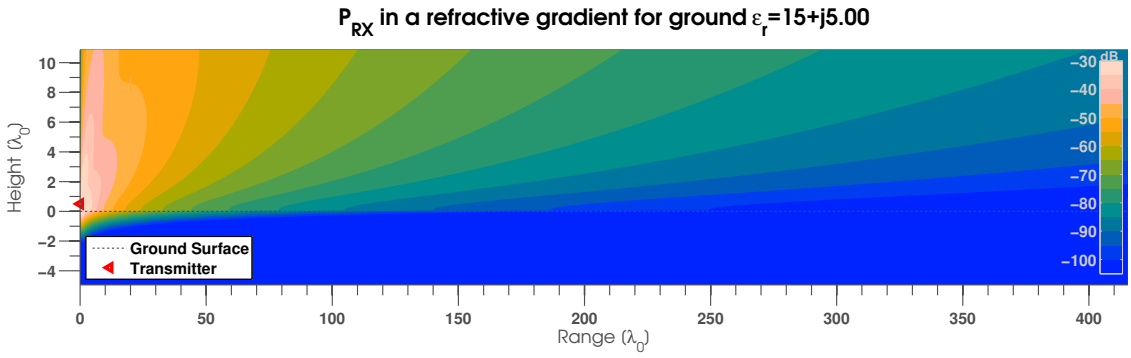

Figure 57: Received power contours in the scenario of Figure 52, with ground relative permittivity $\varepsilon_r = 15 + j5$.

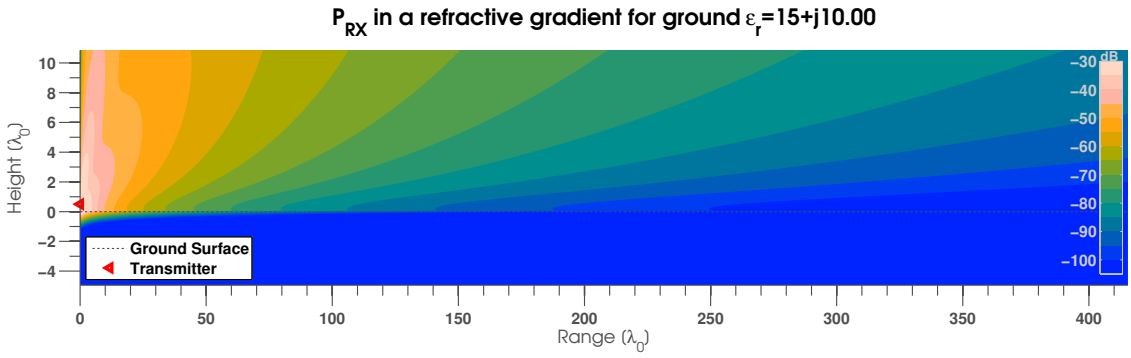

Figure 58: Received power contours in the scenario of Figure 52, with ground relative permittivity $\varepsilon_r = 15 + j10$.

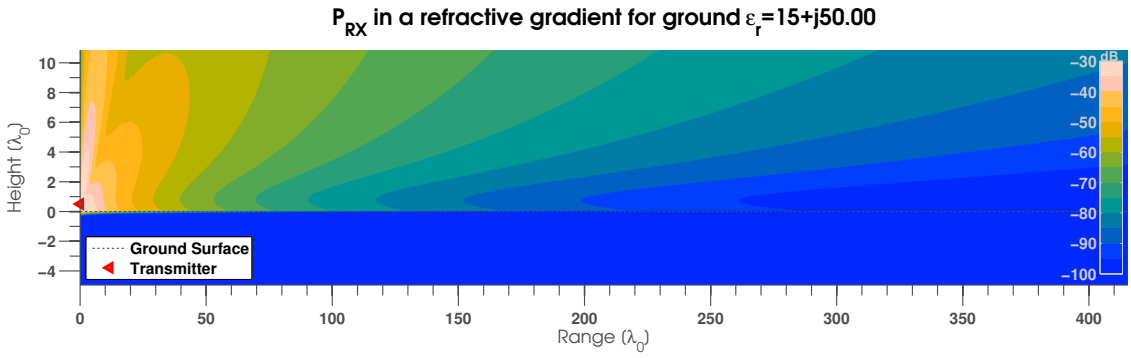

Figure 59: Received power contours in the scenario of Figure 52, with ground relative permittivity $\varepsilon_r = 15 + j50$.

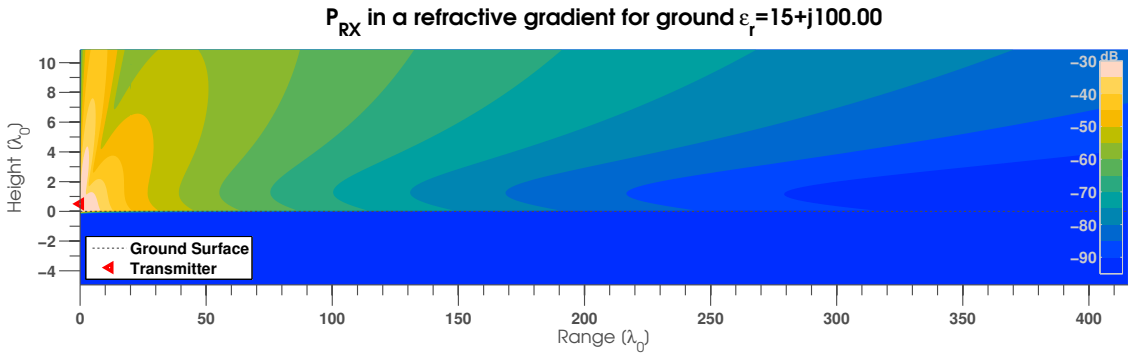

Figure 60: Received power contours in the scenario of Figure 52, with ground relative permittivity $\varepsilon_r = 15 + j100$.

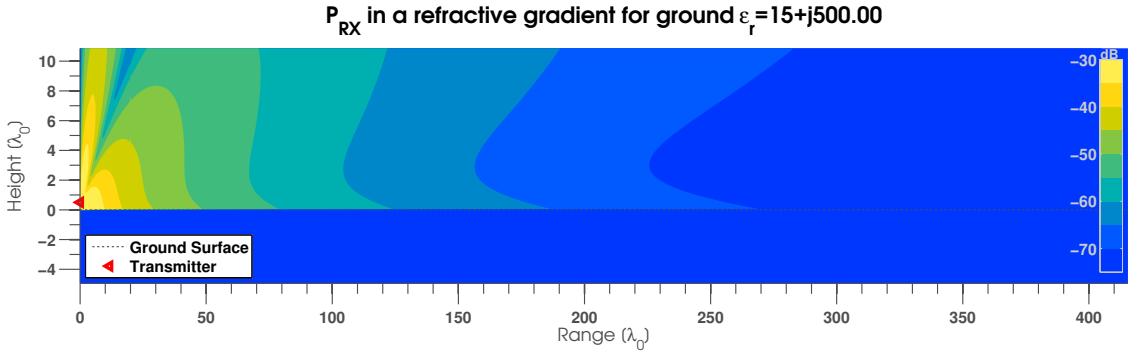

Figure 61: Received power contours in the scenario of Figure 52, with ground relative permittivity $\varepsilon_r = 15 + j500$.

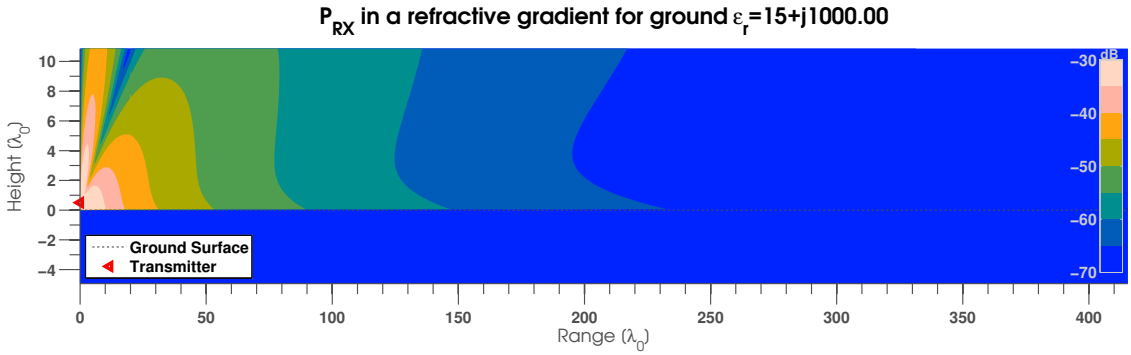

Figure 62: Received power contours in the scenario of Figure 52, with ground relative permittivity $\varepsilon_r = 15 + j1000$.

The interplay of the conductive effects with the refractive gradient above the ground is complex. The refractive gain corresponding to Figures 52-62 appears in Figures 63-73. In the near-ground region, these figures exhibit the following qualitative pattern. As the conductivity is increased to $\varepsilon_r'' \approx 70$, the maximal refractive gain near the surface decreases slightly. Beyond $\varepsilon_r'' \approx 70$, the value of the refractive gain at the surface increases. A plot illustrating this relationship appears in Figure 74.

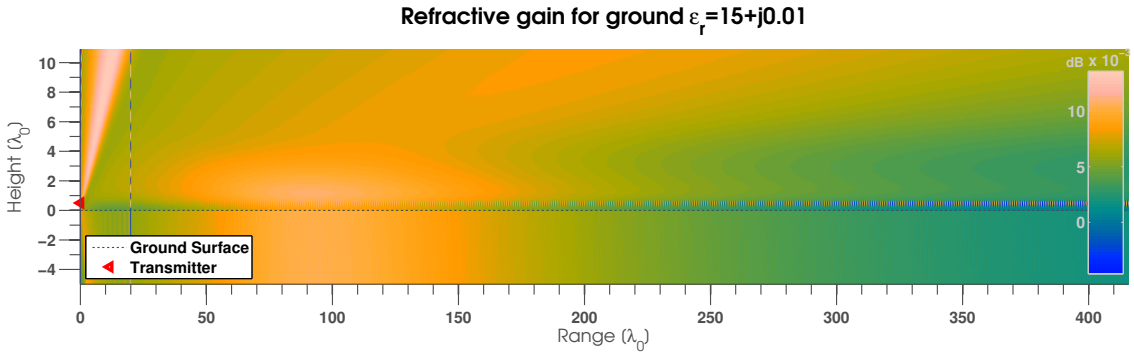

Figure 63: Refractive gain contours for a transmitter at $z' = \lambda_0/2$ over ground with relative permittivity $\varepsilon_r = 15 + j0.01$. The refractivity above ground appears in Figure 40.

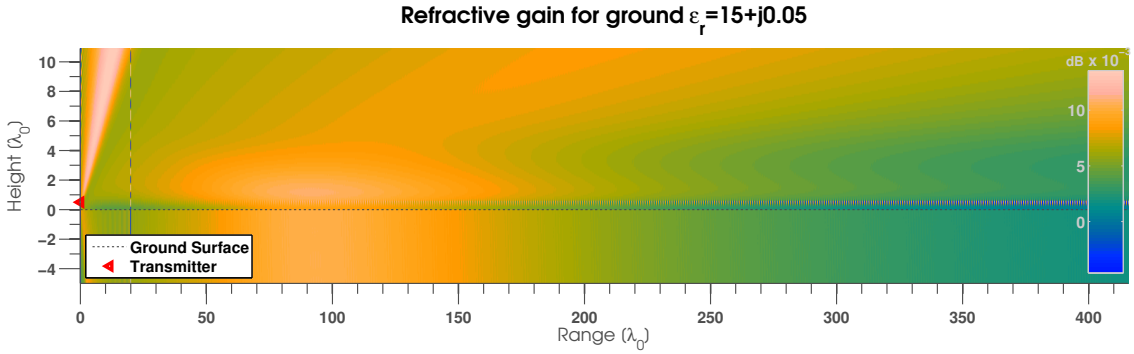

Figure 64: Refractive gain contours in the scenario of Figure 63, with $\varepsilon_r = 15 + j0.05$.

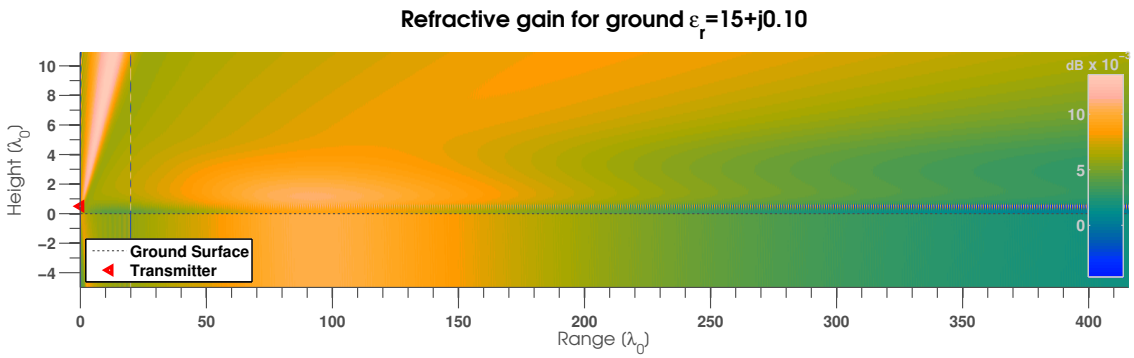

Figure 65: Refractive gain contours in the scenario of Figure 63, with $\varepsilon_r = 15 + j0.1$.

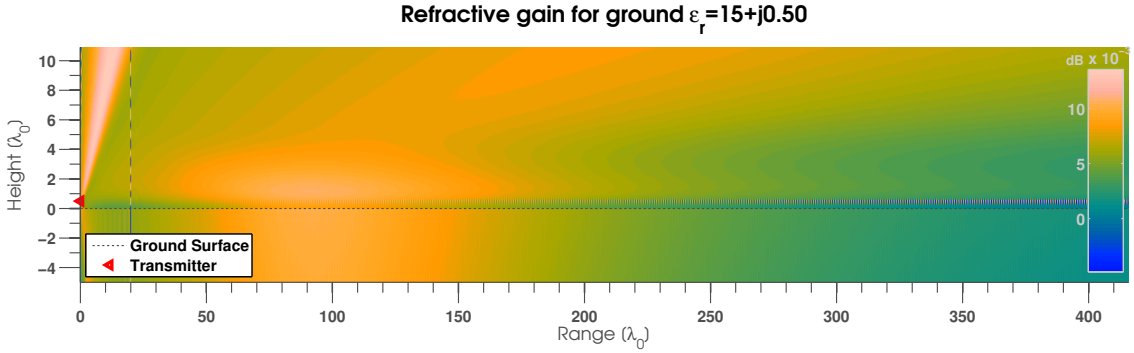

Figure 66: Refractive gain contours in the scenario of Figure 63, with $\varepsilon_r = 15 + j0.5$.

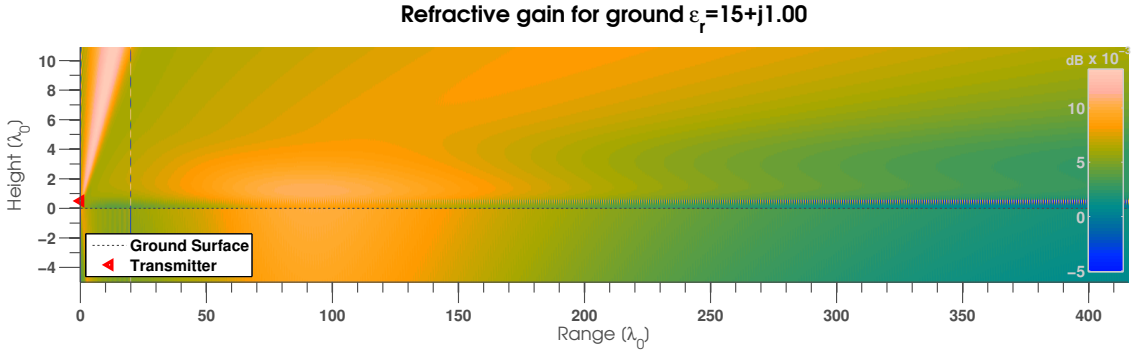

Figure 67: Refractive gain contours in the scenario of Figure 63, with $\varepsilon_r = 15 + j1$.

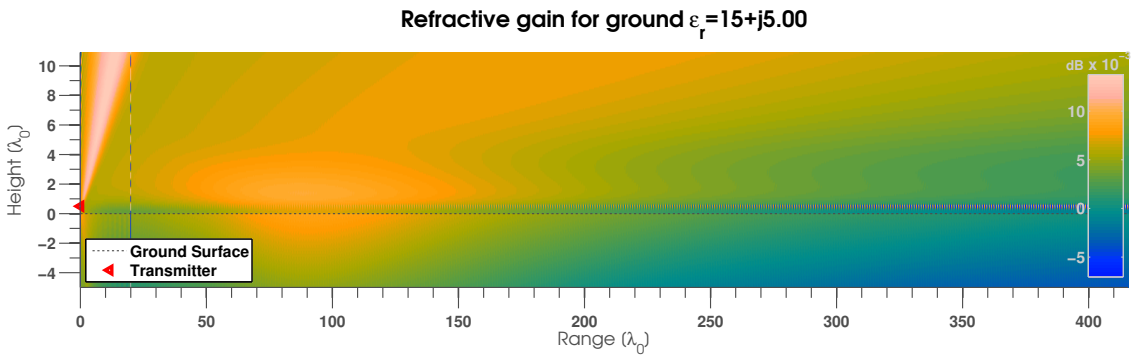

Figure 68: Refractive gain contours in the scenario of Figure 63, with $\varepsilon_r = 15 + j5$.

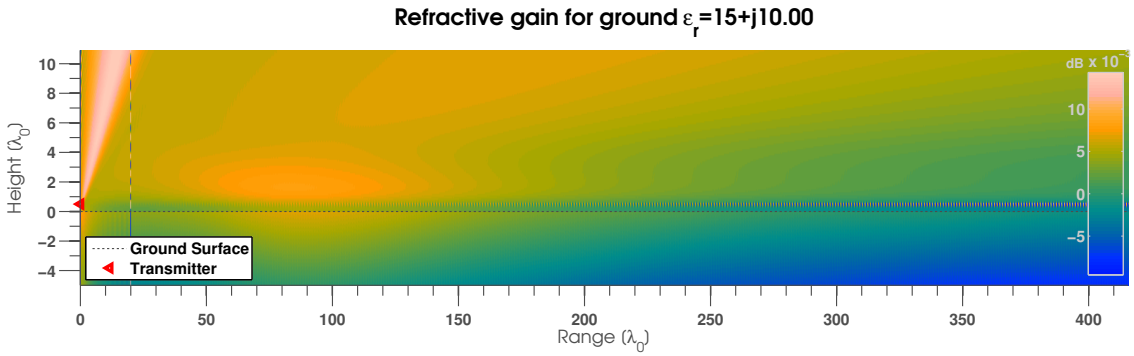

Figure 69: Refractive gain contours in the scenario of Figure 63, with $\varepsilon_r = 15 + j10$.

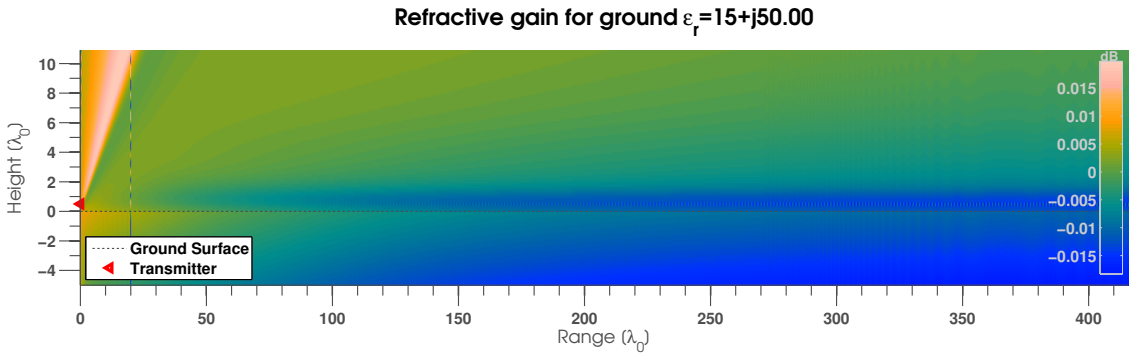

Figure 70: Refractive gain contours in the scenario of Figure 63, with $\varepsilon_r = 15 + j50$.

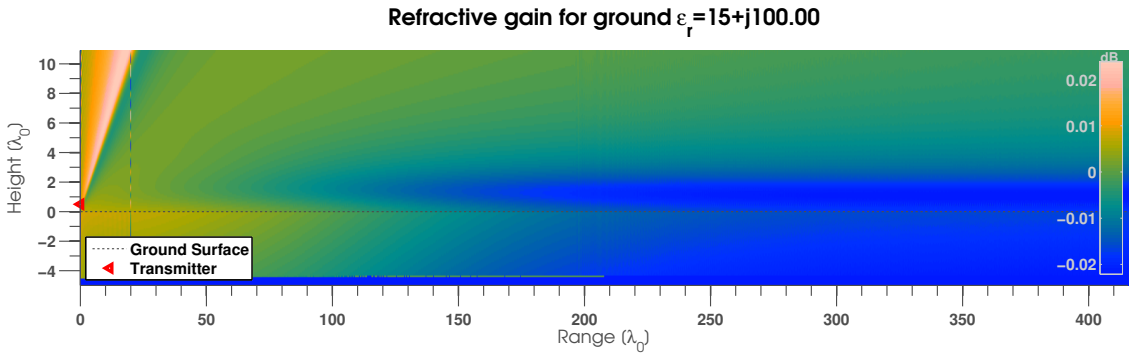

Figure 71: Refractive gain contours in the scenario of Figure 63, with $\varepsilon_r = 15 + j100$.

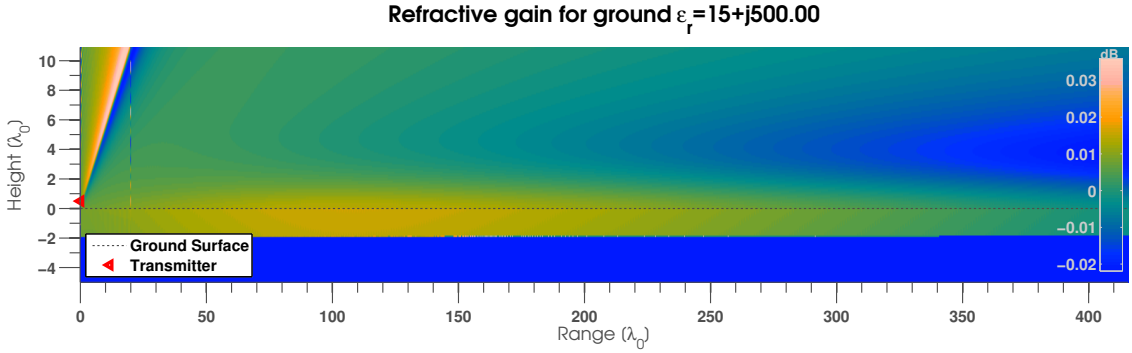

Figure 72: Refractive gain contours in the scenario of Figure 63, with $\varepsilon_r = 15 + j500$.

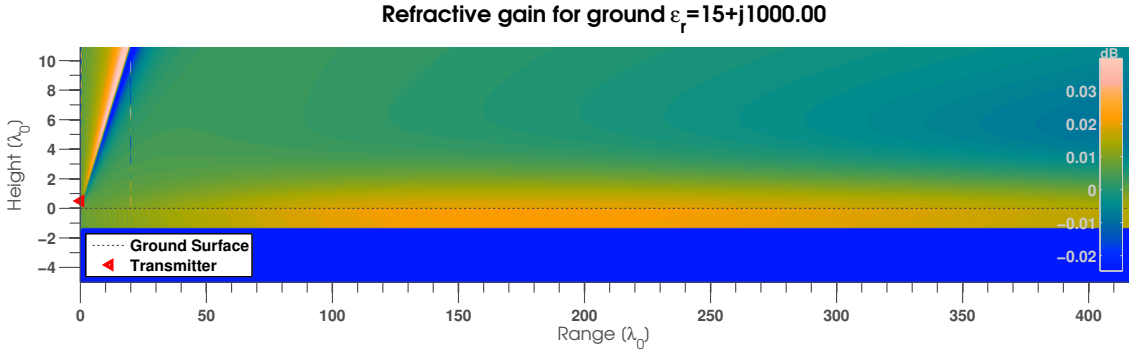

Figure 73: Refractive gain contours in the scenario of Figure 63, with $\varepsilon_r = 15 + j1000$.

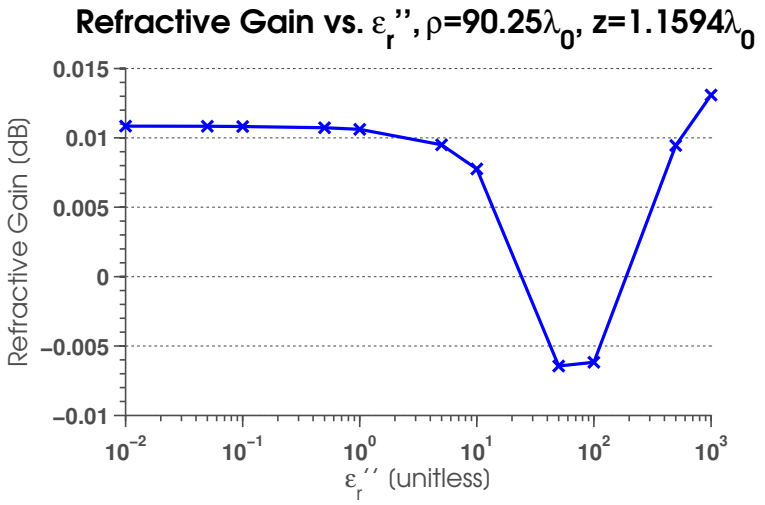

Figure 74: Refractive gain for a receiver at $\rho \approx 90.25$, $z = 1.1594\lambda_0$ is plotted for various values of ε_r''. The plot exhibits what can be described as a resonance near $\varepsilon_r'' \approx 70$.

Calculations of the refractive-gain in increasingly conductive ground conditions underscores some of the numerical limitations of the SI technique of Chapter 2. Various artifacts in the power ratio calculations can be seen in the above contour plots, including a discontinuity at $\rho = 20\lambda_0$, numerical lack-of-convergence of the quadrature routine near the source height $z' \approx \lambda_0/2$, and a problem related to finite machine precision and resolving very small values of the fields inside a good conductor. These limitations introduce significant errors only along isolated lines in the 2D plots. For the purposes of estimating the fields, power, and gains, the problematic lines can be simply excluded from the results, or smoothed by interpolation from nearby values.

4.7 Effect of Frequency Scaling

UHF propagation in various natural and extreme refractive and ground conditions has been demonstrated in the previous sections of this chapter. In all previously presented propagation scenarios, the ground-atmosphere system appears to focus transmitted UHF power in one localized region near the ground, while attenuating the power available to a receiver at other locations. However, it can be expected in general that a refractivity gradient and

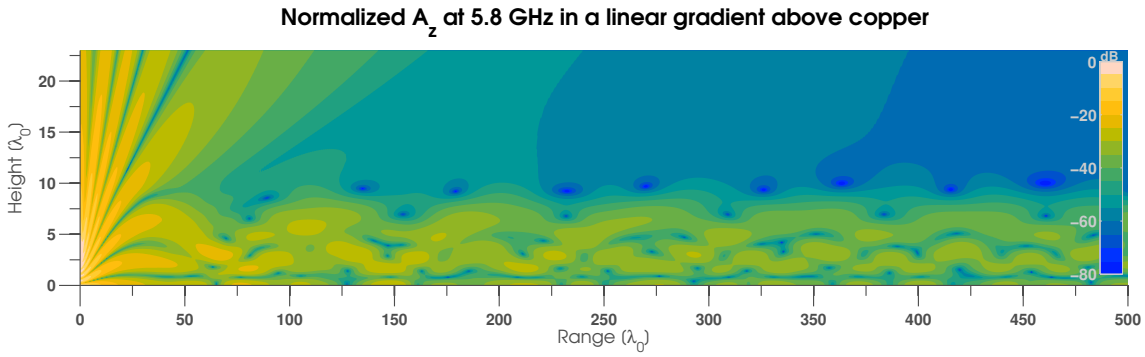

Figure 75: A short dipole operating at 5.8 GHz radiates at range $\rho = 0$ and height $z' = 3.1123\lambda_0$ above a copper substrate that is coated with a graded-index multilayer material. The refractive index of the material is 1.1 at the copper surface at height zero, and linearly decreases to the free-space refractive index ($n = 1$) at $10\lambda_0$ above the substrate. Air with refractive index $n = 1$ is above the multilayer material.

ground can behave as a waveguide, where the fields are repeatedly refracted downwards towards the ground and reflected upwards from the ground surface. In a previously presented conference paper [89], code implementing the model of Chapter 2 was demonstrated to predict waveguide behavior under strong refractive gradients above a highly conductive ground . The primary result of the previous analysis is recapitulated in Figure 75.

Near the dipole source in Figure 75, the fields are well approximated by those of a dipole in a single homogeneous medium above a ground plane. The primary propagation mechanisms are direct and reflected waves that constructively and destructively interfere, leading to visible interference minima and maxima in the plot. However, for ranges beyond $\rho \approx 20\lambda_0$, the field behavior changes drastically from what might be expected in a homogeneous medium above a ground plane. Around $\rho \approx 20\lambda_0$, the beams caused by the interference pattern visibly bend downwards from the expected straight paths of a homogeneous medium. The field distribution at further ranges and height $z < 10\lambda_0$ has a complicated structure, but downward and upward undulations in this structure are apparent. This undulation is evidence of repeated downward refraction by the multilayer followed by upward reflection from the substrate surface, which is indicative of a waveguide. The fields are "trapped" by total internal reflection near the top of the structure and reflection from

the conductive ground plane at the bottom of the structure. Since the fields are not free to spread out in height inside the waveguide, the expected spherical spreading of power in 3D space ($1/r^2$) is reduced instead to a cylindrical spreading ($1/r$), leading to much more power propagating in the waveguide than would propagate in free-space conditions.

The waveguide behavior of Figure 75 contrasts greatly with the previously presented lens-like behavior of natural and amplified refractive structures above the earth. The two scenarios both involve a downward-bending refractive medium and a nominally reflective ground-plane, yet waveguiding behavior has not been predicted by the presented EM model for any atmospheric scenarios, realistic or otherwise. One major difference between the scenario of Figure 75 and the atmospheric scenarios is the length-scale of the refractive structure. In Figure 75, the refractive structure is 10 wavelengths large, while in the atmospheric scenarios presented in the previous sections of this chapter, the refractive structure is approximately 6 wavelengths large. The scale of the refractive structure in wavelengths may be a very important parameter in the waveguiding behavior of atmospheric refractive structures. This statement can be motivated by the observation that waveguides only effectively guide waves with wavelength of the order of (or larger than) the waveguide transverse dimensions. Thus, as frequency increases and wavelength decreases for a fixed atmospheric and ground condition, by analogy to other waveguides, it can be expected that a cutoff frequency is reached, beyond which atmospheric waveguiding occurs near the ground. The remainder of this section investigates the wavelength dependence of propagation in refractive structures near the earth surface.

Results using the model of Chapter 2 were calculated across various transmit frequencies. The transmitter height is fixed at a physical height of $z' \approx 8.42$ cm above the surface of the ground, corresponding to $\lambda_0/2$ at the original frequency of the measurements, 1.78 GHz. Across all frequencies, the plot range and height window remained constant, i.e, $(\rho, z) \in [0, 10000] \times [0, 1.828]$, where both units are in meters. The frequencies simulated were 100 logarithmically spaced frequency points between 3.0 GHz and 30.0 GHz. This

is the super high frequency (SHF) band of frequencies. Although the primary topic of this document is propagation at UHF frequencies, higher frequencies are studied in this section to attempt understand the effects of frequency in near-earth refractive conditions. In order to isolate the effect of frequency scaling in refractive conditions, atmospheric absorption effects, which can contribute additional losses of approximately 0.2 dB/km in this band [130], are also neglected. In other words, the air is assumed to be lossless at all frequencies. Finally, the ground dielectric properties are assumed to be frequency independent in this set of simulations. Realistic ground and soils have complicated loss behavior vs. frequency, due to the frequency dependence of the conduction of electrons (conductivity) and molecular dipolar resonances (dielectric losses). To isolate the effect of the length scale of the refractive index gradient in wavelengths, the ground dielectric is held at a constant $\varepsilon_r = 15 + j100$ across all frequencies. Plots of the received power in space for a selection of five simulated frequencies appears in Figures 76-80.

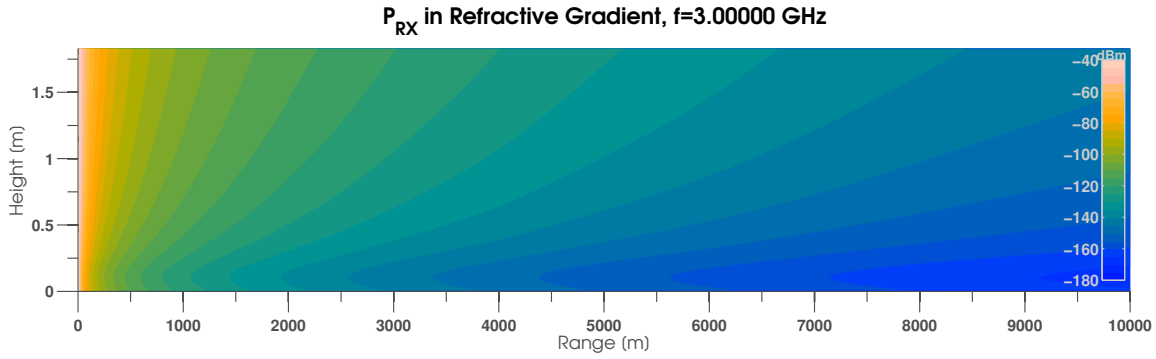

Figure 76: A short dipole operating at 3.00000 GHz radiates at range $\rho = 0$ and height $z' \approx 8.42$ cm above ground with $\varepsilon_r = 15 + j100$. The air contains a refractivity gradient that is given in Figure 40.

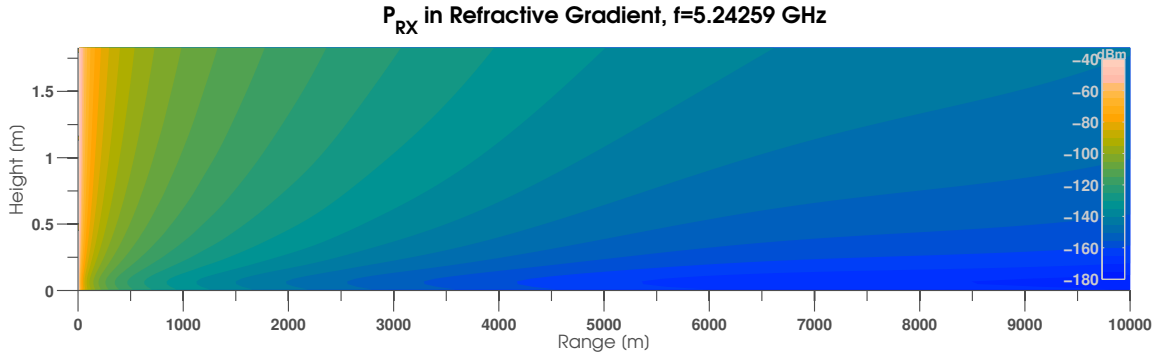

Figure 77: A short dipole operating at 5.24259 GHz radiates at range $\rho = 0$ and height $z' \approx 8.42$ cm above ground with $\varepsilon_r = 15 + j100$. The air contains a refractivity gradient that is given in Figure 40.

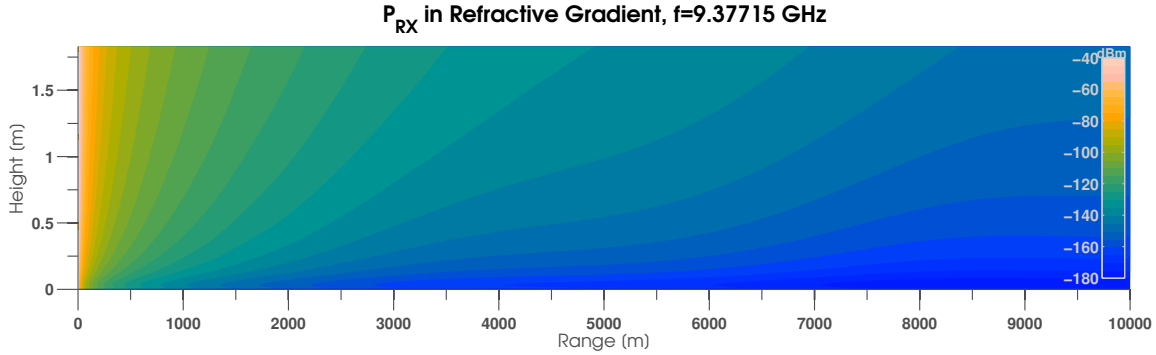

Figure 78: A short dipole operating at 9.37715 GHz radiates at range $\rho = 0$ and height $z' \approx 8.42$ cm above ground with $\varepsilon_r = 15 + j100$. The air contains a refractivity gradient that is given in Figure 40.

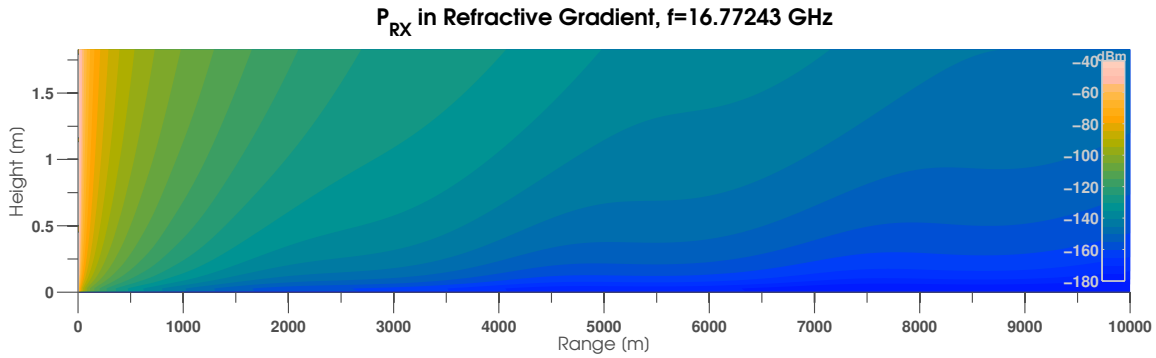

Figure 79: A short dipole operating at 16.77243 GHz radiates at range $\rho = 0$ and height $z' \approx 8.42$ cm above ground with $\varepsilon_r = 15 + j100$. The air contains a refractivity gradient that is given in Figure 40.

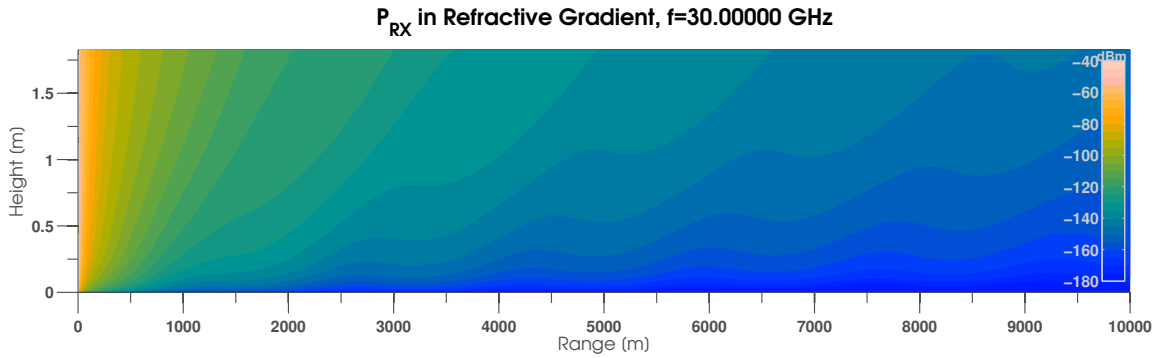

Figure 80: A short dipole operating at 30.00000 GHz radiates at range $\rho = 0$ and height $z' \approx 8.42$ cm above ground with $\varepsilon_r = 15 + j100$. The air contains a refractivity gradient that is given in Figure 40.

As the frequency increases in the series of plots in Figures 76-80, the received power does not drastically, qualitatively change. The biggest change that can be discerned is that the constant-power contours oscillate up and down with range, and that this oscillation has a shorter length-scale for higher frequencies. As in previous sections, it is more instructive to look at the refractive gain. A series of plots of the refractive gain across a selection of five frequencies is presented in Figures 81-85.

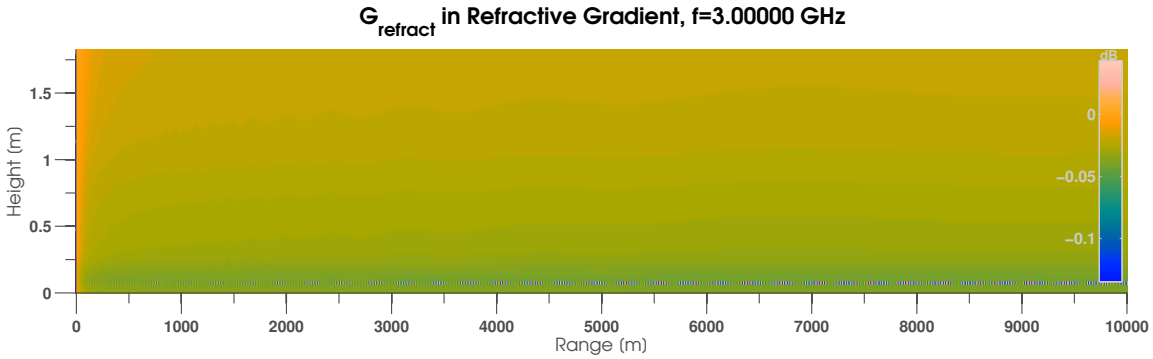

Figure 81: The refractive gain corresponding to Figure 76 is presented.

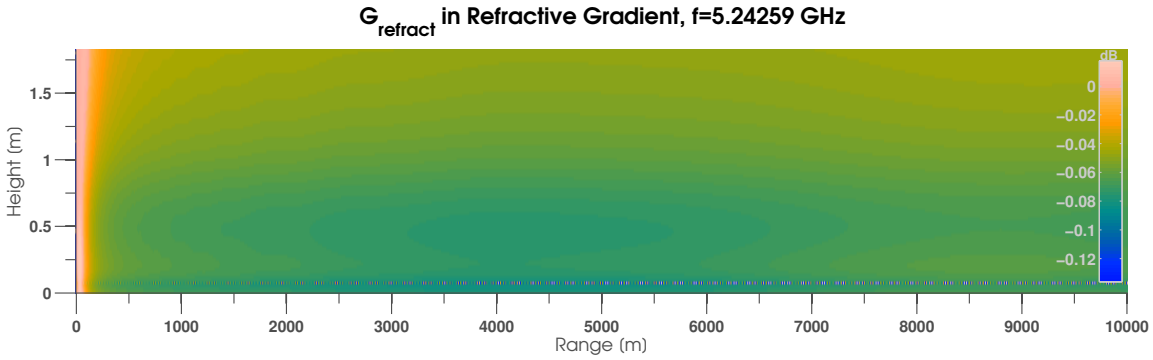

Figure 82: The refractive gain corresponding to Figure 77 is presented.

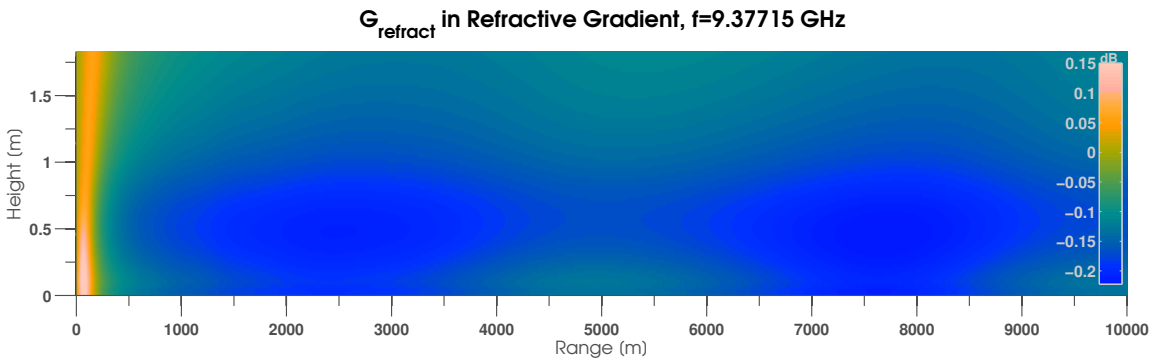

Figure 83: The refractive gain corresponding to Figure 78 is presented..

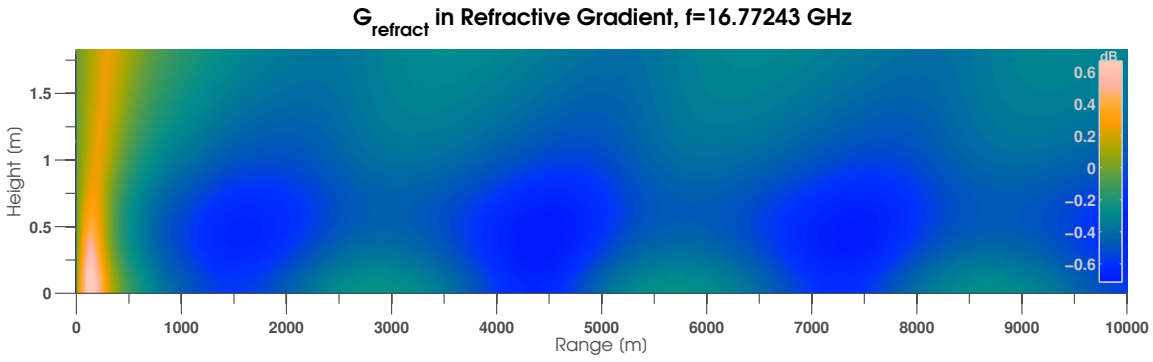

Figure 84: The refractive gain corresponding to Figure 79 is presented.

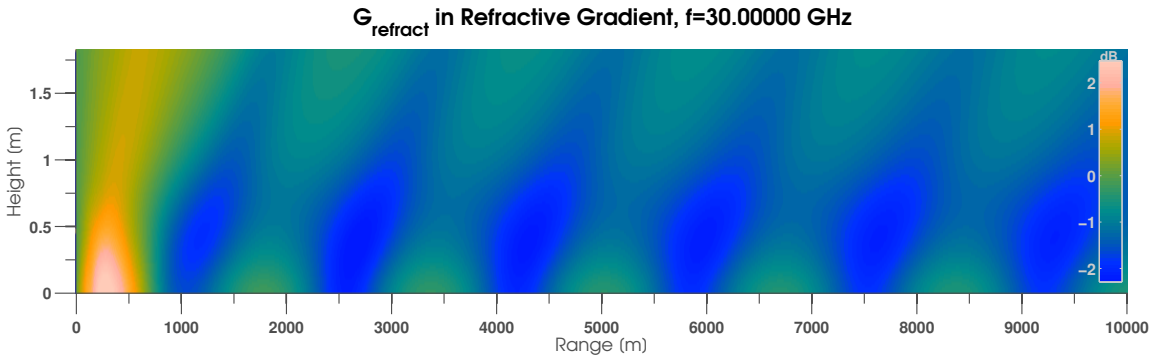

Figure 85: The refractive gain corresponding to Figure 80 is presented.

The effects of frequency scaling on propagation through near-ground refractive structures now becomes more apparent. As previously discussed, the refractive gradient studied tends to draw more radiated power into a region near the transmitter, while drawing power away from other regions. As frequency increases in the series of plots in Figures 81-85, two things occur in the region of increased power. Firstly, the region becomes larger in dimension. Secondly, the power concentration in the region goes up as well, which can be seen by examining the color scale across the plots. The regions in which the power is attenuated appear to be periodic with range, and also change in two ways as the frequency increases across the plots. Firstly, the spacing between adjacent regions becomes smaller as the frequency increases, and a larger number of such regions appear in the range of the plots. Secondly, the amount of attenuation in the regions increases with increasing frequency, which can be seen from examining the color scale across the plots.

As a summary visualization of the results, the refractive gain along the ground level for all simulated frequencies is presented in Figure 86. This figure clearly shows the enlarging of the enhancement region with frequency, and the corresponding behavior of the attenuated regions. At first glance, this may appear to be a waveguide cutoff phenomenon, whereby higher frequencies are confined in the refractive structure, while lower frequencies are cutoff. However, examining the plots of the power in the channel (Figures 76-80) tells a different story. The power in Figures 76-80 propagates outward with subtle undulations in the contours. This contrasts with what could be expected of a true waveguide past the cutoff frequency, e.g., Figure 75. If a waveguiding cutoff frequency were present in the sequence of Figures 76-80, then the plots for frequencies past cutoff would qualitatively look like a waveguide like Figure 75, with a concentration of power near the ground and visible upward and downward undulations. The apparent cutoff-type behavior in Figure 86 is due to the dynamic range of the color scale of that plot. At lower frequencies near the bottom of the plot, the enhancement and attenuation region are present, as is demonstrated

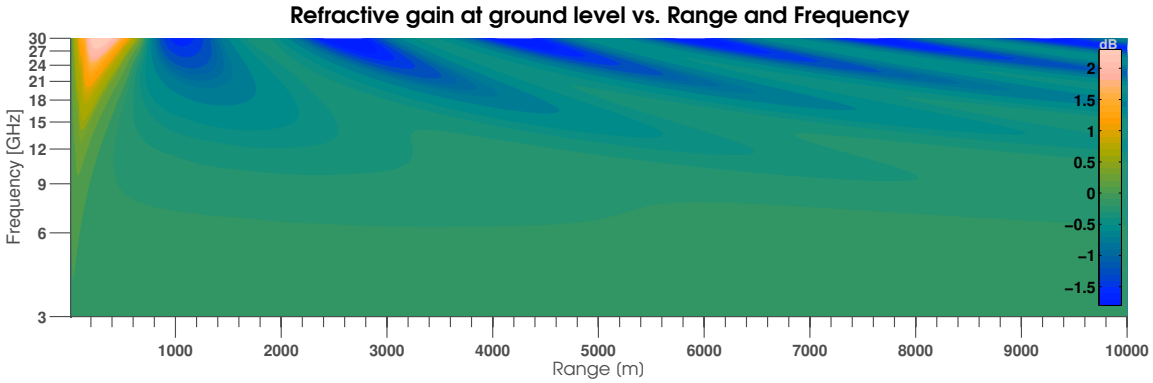

Figure 86: The refractive gain at the ground level is plotted as a function of range along the ground and simulation frequency.

by Figures 81-85. The enhancement region does not disappear at lower frequencies; it is always present. However, the magnitude of the enhancement and attenuation decreases with decreasing frequency. The fractions of a decibel of enhancement and attenuation that are present at 3 GHz are much smaller than the several decibels of variation that are present at 30 GHz. Therefore, the small variations at lower frequencies are drowned out by the larger variations at higher frequencies.

CHAPTER 5

CONCLUSIONS AND FUTURE DIRECTIONS

This document has presented the results of simulations, modeling, measurements, and analysis of UHF propagation in atmospheric refractive structures near the surface of the earth. The main contributions to the scientific and engineering communities include the following.

- A general mathematical and computational model of EM propagation in multilayered media excited by time-harmonic vertical dipole sources.
- A simple measurements-based modeling and curve-fitting methodology for determining continuous atmospheric profiles for temperature, humidity, and refractivity near the surface of the earth.
- A measurements-based case-study of UHF propagation in a near-ground refractive environment.
- A study of the parameters that affect general RF propagation in near-ground atmospheric refractivity.

The primary practical result is a body of evidence that suggests that UHF propagation over hundreds of meters near the surface of the earth is not significantly affected by near-earth atmospheric refractivity, at least for vertical wire antennas, or any antenna that emits radiation of the same polarization as a vertical wire antenna. However, the methods developed do show that atmospheric refractivity is more of a factor at higher frequencies approaching millimeter waves. The developed techniques might find future use in studies involving the 24 GHz or 61 GHz bands, which have both been identified as available industrial, scientific, and medical radio bands by the International Telecommunication Union[131].

The model of Chapter 2 makes unique contributions to the body of knowledge and practice of spectral domain methods and Sommerfeld integrals in the following ways.

- While previous work has used techniques such as the steepest-descent-path (SDP) for quadrature in the far-field, this is the first work (to the knowledge of the author) to use asymptotic quadrature routines to calculate far-fields in a general class of non-magnetic multilayers. This is a significant improvement over the previous method, because it allows the integrals to be calculated on a grid of receive points from a fixed set of spectral domain samples. The SDP approach, on the other hand, requires sampling on a unique curve in the spectral domain for every point in the receive grid. Because the fields can be calculated at many positions essentially in parallel from the same set of spectral domain data, the multitude of potential/field/power contour plots presented in this work were possible. This contrasts greatly with the majority of work on SI quadrature in which the final presented results are line plots of calculated field values along a linear trajectory away from the sources.

- Whereas previous works have used adaptive quadrature, in which integrals are approximated by quadrature until a convergence criterion is met, this work uses an *adaptive sampling of the integrands*. The difference again is one of speed and efficiency: once the integrands are sampled on a fixed set of points, all quadrature can proceed essentially in parallel for any range and height away from the source. An adaptive quadrature, on the other hand, would go through a separate procedure to approximate the integrals for each range and height of interest.

- The developed SI model has already found use by other members of the Propagation Group at the School of Electrical and Computer Engineering of the Georgia Institute of Technology. It is also freely available on the internet in a revision-controlled collaborative repository,

  `https://bitbucket.org/rajb245/multilayergreens_evalfixes`

It is hoped that a user and developer community can form around the project to extend the method to more general sources. The public release of computational EM code is an often-overlooked contribution to the broader community.

The entirety of Chapter 3 is also a unique contribution to measurement-based modeling. It is the first work, to the knowledge of the author, to present the results of atmospheric measurements alongside RF measurements, and attempt to analyze the relationship between the two at UHF frequencies near the surface of the earth.

This work is not, however, without limitations. The SI method of Chapter 2 has been validated by a few simple cases in which analytical solutions are available, or in which physical arguments can be made for expected solutions. More extensive validation and verification is desirable. The error between the provided solutions and the true solutions is often unknown, but in the validation examples where analytical reference solutions were available, the error results were highly variable. In some cases, the SI model was found to be in close agreement with the analytical solutions (hundredths of a decibel in error), but was frequently in error by several tenths of a decibel, and very rarely in error by tens of decibels in isolated regions. More carefully studying the sources of these errors, and devising algorithms to reduce them, is a future direction that will be pursued.

Spectral domain methods for propagation in multilayered media for modeling long-range radio propagation is a research area that contains a variety of other future research directions. The method can be extended to more general sources, including vertical magnetic dipoles, horizontal magnetic dipoles, and horizontal electric dipoles. This work has only focused on refractive and ground effects for fields emitted by vertical electric dipoles, but it is possible that waves emitted by other sources interact differently with refractive gradients and ground. Such extensions would also enable the study of propagation of waves from arbitrary antennas, such as helices, dishes, horns, or patches through a surface scattering calculation in the multilayered medium. Similarly, the ability to model aribitrary sources would enable calculations involving scatterers in a multilayered medium such as

vehicles, buildings, terrain, or plants and foliage using a surface or volume scattering formulation as well.

Another direction of exploration is the myriad of other SI quadrature methods from the literature [132, 109, 90, 100, 99, 98, 105, 106, 96, 97]. A systematic implementation of all the available methods, and evaluation of these implementations for speed, efficiency, and accuracy would be a valuable study in selecting an optimal method.

Finally, the value of novel RF measurement campaigns cannot be understated. The height, range, atmospheric, and frequency regimes explored in this dissertation remain largely unstudied by experimental methods. The measurements presented in this work are first-of-a-kind in presenting a comprehensive treatment of coupled atmospheric and EM measurements and modeling for UHF communications links operating near the surface of the earth. More measurements and more data will be required to fully validate the methods used, and to get a complete picture of RF propagation in the near-ground environment.

5.1 Supporting Publications

Two papers have been published in support of this work. The first is a letter that appeared in IEEE Transactions on Wireless Communications. Although not discussed in this document, it supported the the proposal of the present work by taking a stochastic channel modeling approach to a measured near-ground RF data set that had been captured by a sliding correlator channel sounder. It describes a technique to estimate Rician statistics from channel measurements collected by a sliding-correlator channel sounder:

> Bhattacharjea, R.; Durgin, G.D.; Anderson, C.R., "Estimation of Rician K-Factors from Block-Averaged Channel Measurements," Wireless Communications, IEEE Transactions on , vol.11, no.12, pp.4231-4236, December 2012

The second forms the basis of Chapter 2, and is a conference paper that appears in the Proceedings of the Progress in Electromagnetics Research Symposium, 2013:

> Bhattacharjea, R.; Anderson, C.R.; Durgin, G.D., "A Direct Spectral Domain Method for Near-ground Microwave Radiation by a Vertical Dipole above Earth in the Presence of Atmospheric Refractivity," Proceedings, PIERS , August 2013

An accompanying presentation was given to an audience of conference attendees in Stockholm, Sweden, in August 2013. It is archived on the web at:

> `http://www.prism.gatech.edu/~gtg037s/Bhattacharjea_Presentation_PIERS2013_Stockholm.pdf`

Finally, a third publication is in preparation. The presented validation example that couples a coordinate transformation with the SDGF/SI method for long range propagation above the curved earth surface is entirely novel and has applications in the radar community. A draft expanding on that example was prepared for IEEE RADAR2014, but ultimately was not submitted due to time constraints. Future plans include finding a venue in which to publish this draft.

APPENDIX A

MAXWELL'S EQUATIONS AND MATHEMATICAL CONVENTIONS

Maxwell's equations in an isotropic, linear, nonmagnetic, homogeneous, time-invariant medium with relative permittivity $\varepsilon_{r\ell}$ are

$$\begin{aligned} \nabla\times\boldsymbol{\mathcal{E}} &= -\mu_0\frac{\partial\boldsymbol{\mathcal{H}}}{\partial t}, \qquad \nabla\times\boldsymbol{\mathcal{H}} = \varepsilon_{r\ell}\varepsilon_0\frac{\partial\boldsymbol{\mathcal{E}}}{\partial t} + \boldsymbol{\mathcal{J}}, \\ \nabla\cdot\boldsymbol{\mathcal{H}} &= 0, \qquad\qquad \nabla\cdot\boldsymbol{\mathcal{E}} = \frac{\rho}{\varepsilon_{r\ell}\varepsilon_0}. \end{aligned} \tag{68}$$

If all fields have a $\exp(-j\omega t)$ time dependence, then $\frac{\partial}{\partial t} \rightarrow -j\omega$. This is the convention for all time-dependence assumed throughout this work. The time harmonic equations are then

$$\begin{aligned} \nabla\times\mathbf{E} &= j\omega\mu_0\mathbf{H}, \qquad \nabla\times\mathbf{H} = -j\omega\varepsilon_{r\ell}\varepsilon_0\mathbf{E} + \mathbf{J}, \\ \nabla\cdot\mathbf{H} &= 0, \qquad\qquad \nabla\cdot\mathbf{E} = \frac{\rho}{\varepsilon_{r\ell}\varepsilon_0}, \end{aligned} \tag{69}$$

where the charge density ρ must be reinterpreted as the magnitude of a time-harmonic charge density. The time-harmonic expressions used for the magnetic vector potential, $\mathbf{A}$, the scalar electric potential, φ, and the Lorenz gauge choice are given by

$$\mathbf{H} = \frac{1}{\mu_0}\nabla\times\mathbf{A}, \qquad \mathbf{E} = -\nabla\varphi + j\omega\mathbf{A}, \quad \nabla\cdot\mathbf{A} = j\omega\mu_0\varepsilon_{r\ell}\varepsilon_0\varphi. \tag{70}$$

With these definitions of potential functions and gauge choice, Maxwell's equations become uncoupled scalar Helmholtz equations

$$\nabla^2\mathbf{A} + \omega^2\mu_0\varepsilon_{r\ell}\varepsilon_0\mathbf{A} = -\mu_0\mathbf{J}, \qquad \nabla^2\varphi + \omega^2\mu_0\varepsilon_{r\ell}\varepsilon_0\varphi = -\frac{\rho}{\varepsilon_{r\ell}\varepsilon_0}. \tag{71}$$

The quantity $\omega^2\mu_0\varepsilon_{r\ell}\varepsilon_0$ will be the square of the wavenumber of propagating wave solutions to those equations, and is shortened as k_ℓ^2 throughout this work. The use of the ℓ subscripts have been in anticipation of using ℓ as an index into a list of materials with differing values

of dielectric constant and refractivity, as in Figure 10. Solving the Helmholtz equation for the magnetic vector potential in multilayered media is the primary approach of Chapter 2.

APPENDIX B

FOURIER TRANSFORM OF CYLINDRICALLY SYMMETRIC FUNCTIONS: HANKEL TRANSFORM

The following Fourier transform integral was presented in Equation 2

$$A_z(x,y,z,z') = \int_{-\infty}^{\infty}\int_{-\infty}^{\infty} \tilde{A}_z\left(k_x,k_y,z,z'\right) e^{j(k_x x+k_y y)}\, dk_x\, dk_y\ .$$

A change of variables in the double integral above can simplify it into a single integral. First define

$$\mathbf{k}_\rho = (k_x,k_y), \quad ||\mathbf{k}_\rho|| = \sqrt{k_x^2+k_y^2} = k_\rho,$$

$$\boldsymbol{\rho} = (x,y), \quad ||\boldsymbol{\rho}|| = \sqrt{x^2+y^2} = \rho.$$

Then the part of the argument of the exponential in parentheses becomes

$$k_x x + k_y y = \mathbf{k}_\rho \cdot \rho = ||\mathbf{k}_\rho||\,||\rho|| \cos(\theta) = k_\rho \rho \cos(\theta),$$

where θ is the angle between the vectors $\mathbf{k}_\rho$ and $\boldsymbol{\rho}$. Under the change of variables $(k_x,k_y) \rightarrow (k_\rho,\theta)$, the differential $dk_x\, dk_y$ transforms as

$$dk_x\ dk_y \quad \rightarrow \quad k_\rho d\theta\ dk_\rho,$$

and the integration interval transforms as

$$(k_x,k_y) \in \mathbb{R}\times\mathbb{R} \quad \rightarrow \quad (k_\rho,\theta) \in [0,\infty)\times[0,2\pi)$$

Finally, if $\tilde{A}_z\left(k_x,k_y,z,z'\right)$ only depends on k_x and k_y through the radial wavenumber $k_\rho = \sqrt{k_x^2+k_y^2}$ and the spatial domain field $A_z(x,y,z,z')$ only depends on x and y through the range ρ, then the above can all be substituted into the original integral expression, resulting in

$$A_z(\rho,z,z') = \int_0^{\infty} \tilde{A}_z\left(k_\rho,z,z'\right) \int_0^{2\pi} e^{jk_\rho \rho\cos(\theta)}\, d\theta\ k_\rho dk_\rho.$$

The inner integral over θ is a well known variation of Bessel's integral and results in a multiple of the Bessel function of the first kind and order zero,

$$\int_0^{2\pi} e^{jk_\rho \rho \cos(\theta)}\, d\theta = 2\pi J_0(k_\rho \rho).$$

Inserting Bessel's integral identity into the previous integral results in

$$A_z(\rho, z, z') = 2\pi \int_0^{\infty} \tilde{A}_z\left(k_\rho, z, z'\right) J_0(k_\rho \rho) k_\rho \, dk_\rho.$$

This final expression is a multiple of a Hankel transform of order zero, and is commonly known as a Sommerfeld integral in the field of electromagnetics.

APPENDIX C

ATMOSPHERIC BOUNDARY LAYER DEFINITIONS

This appendix serves to demonstrate the notation for and definitions of quantities in the atmospheric boundary layer, which may be unfamiliar to the reader. The goal is not to give a comprehensive treatement of the material, but rather to give an introduction to the physical quantities considered in atmospheric boundary layer modeling. The developments mostly follow the textbook of Garratt, which should be considered the definitive reference for the material [119].

The dynamics of the atmospheric boundary layer (ABL) are governed by a series of conservation laws for momentum, mass, thermal energy, and water vapor in the atmosphere, along with an equation of state that relates together the temperature, pressure, and volume of a given mass of air. The unknown quantities in this system of equations are

- (u_x, u_y, u_z) - Wind velocity vector-field. This is a 3D cartesian vector, with (u_x, u_y) transverse to the earth surface, and u_z measured radially outward from the center of the earth. The vector-field has units of m/s.
- T - Absolute temperature. This quantity has units of K.
- ρ - Air density. This quantity has units of kg/m^3.
- q - Specific humidity. This is a unitless mass-fraction of water vapor in the atmosphere. It is the quotient of the mass of water vapor in some volume and the total mass of all gases in the same volume.
- P - Air pressure. This is the force per unit area exerted by a mass of air on a surface. It has units of Pa (or N/m^2).

A secondary quantity that is often used for convenience is the potential temperature, noted

as

$$\theta = T\left(\frac{P_0}{P}\right)^{R/C_p}.$$

This is the absolute temperature in K that would result from bringing the air adiabatically to a reference pressure P_0. Above, R is the specific gas constant of dry air, and C_p is the specific heat capacity of air at constant pressure. This allows for temperature/heat comparisons that are corrected for pressure effects.

Another secondary quantity of interest is the virtual temperature,

$$T_v = T(1 + 0.61q).$$

T_v also has units of absolute temperature in K. It derives from treating air that contains water vapor as as dry air with a higher temperature, only for the purposes of the gas law. The virtual temperature can be pressure-corrected as well, giving the virtual potential temperature,

$$\theta_v = T_v\left(\frac{P_0}{P}\right)^{R_d/C_p},$$

where R_d is the specific gas constant for dry air given previously.

C.1 The Reynolds Decomposition and Expectations

All quantities in the ABL are written in the Reynolds decomposition [120] as

$$a_{\text{tot}} = a + a',$$

where a represents any of the ABL quantities. Each ABL quantity is a stochastic process, and the first term in the decomposition represents the part of the full time and space dependent quantity that is the expected value with respect to a hypothetical ensemble of outcomes, i.e.,

$$\mathbb{E}[a_{\text{tot}}] = a.$$

The second term with the prime marking is a perturbation to the expectation, and has zero expectation by definition.

$$\mathbb{E}[a'] = 0.$$

Note that the expectation is denoted in this work by the typical usage from statistics, $\mathbb{E}[a]$, as opposed to other notations including overbars ($\bar{a}$) or surrounding angle-brackets ($< a >$) that may be seen in other sources.

C.2 Variances and Covariances

The standard definition of variance of a stochastic process is

$$\mathrm{Var}[a_{\mathrm{tot}}] = \mathbb{E}\left[(a_{\mathrm{tot}} - \mathbb{E}[a_{\mathrm{tot}}])^2\right].$$

Directly expanding and simplifying this expression results in

$$\mathrm{Var}[a_{\mathrm{tot}}] = \mathbb{E}\left[(a')^2\right].$$

This is also the variance of a' itself,

$$\mathrm{Var}[a'] = \mathbb{E}\left[(a' - \mathbb{E}[a'])^2\right] = \mathbb{E}\left[(a')^2\right],$$

which gives the interpretation of the term a' as embodying the variance of the stochastic process. Combined together, we have that

$$\mathrm{Var}[a_{\mathrm{tot}}] = \mathrm{Var}[a'].$$

ABL quantities can appear in the dynamical equations as products; for example $u_{z\mathrm{tot}}q_{\mathrm{tot}}$ has the units of velocity, but can be be rearranged and thought of as a mass flux of water vapor (kg/s) per unit density along a line (kg/m); in other words it is a normalized mass flux of water vapor along the z direction of the velocity field. Such a quantity will be encountered in the dynamical equation that deals with the conservation of water vapor. In the Reynolds decomposition, one would take the expectation of such an equation to derive the expected behavior of the stochastic quantities. For example

$$\mathbb{E}[u_{z\mathrm{tot}}q_{\mathrm{tot}}] = \mathbb{E}\left[(u_z + u_z')(q + q')\right] = \mathbb{E}[u_z q] + \mathbb{E}[u_z q'] + \mathbb{E}\left[u_z' q\right] + \mathbb{E}\left[u_z' q'\right]$$

The mean quantities are scalars with respect to the ensemble and come out of the expectations,

$$\mathbb{E}[u_{z\mathrm{tot}}q_{\mathrm{tot}}] = u_z q + u_z \mathbb{E}[q'] + q\mathbb{E}\left[u_z'\right] + \mathbb{E}\left[u_z' q'\right],$$

and the perturbations have zero mean, resulting in

$$\mathbb{E}\left[u_{z\text{tot}}q_{\text{tot}}\right] = u_z q + \mathbb{E}\left[u_z' q'\right].$$

Note that the term on the right is also the definition of the covariance between two total quantities in the ABL:

$$\text{Cov}[u_{z\text{tot}}, q_{\text{tot}}] = \mathbb{E}\left[(u_{z\text{tot}} - u)(q_{\text{tot}} - q)\right] = \mathbb{E}\left[u_z' q'\right].$$

Therefore, the expected dynamical equations will depend on covariances between ABL terms. Up to second order statistics then, the dynamical equations will depend on expectations of single ABL quantities, variances of single ABL quantities, and on covariances between ABL quantities.

The covariance quantities that naturally arise in the dynamical equations include the following. Velocity covariances that arise are often written in terms of stress as

$$\tau_x = -\rho\mathbb{E}\left[u_x' u_z'\right],$$

$$\tau_y = -\rho\mathbb{E}\left[u_y' u_z'\right],$$

which have the expected units of pressure (stress), Pa. The wind-wind covariances usually are taken in a coordinate system so that u_x is in the direction of the mean wind vector and $u_y = 0$. Then the quantity

$$u_*^2 = -\mathbb{E}\left[u_x' u_z'\right]$$

is the square of the "friction velocity". The quantity u_* has units of velocity. On the other hand, u_*^2 has units of velocity-squared, or m^2/s^2. If multiplied by a mass in kg, this would have units of energy; another interpretation is then that u_*^2 has the units of an energy density in J/kg, and represents the energy per unit mass that is contained in the velocity perturbations.

Other covariances that arise in the equations are those between the upward wind velocity and potential temperature or humidity. They appear in the equations as

$$\theta_* = -\frac{\mathbb{E}\left[u_z'\theta'\right]}{u_*},$$

$$q_* = -\frac{\mathbb{E}\left[u_z' q'\right]}{u_*},$$

and

$$\theta_{v*} = -\frac{\mathbb{E}\left[u_z' \theta_v'\right]}{u_*}.$$

C.3 The Obukhov Length and Monin-Obukhov Parameters

With the previous definitions, we can now define the Obukhov length, which appears in the profiles of temperature and humidity near the surface of the earth. The Obukhov length is denoted L and is given by

$$L = \frac{u_{*0}^2 \mathbb{E}\left[\theta_v\right]}{kg\theta_{v*0}},$$

where the zeros now indicate that the relevant quantities are to be calculated at the surface $z = 0$.

Finally, a few other dimensionless quantities enter into the Monin-Obukhov theory, all from physically motivated, but heuristic models, that are fit to empirical observations. Firstly, the von Karman constant is denoted k, and always taken as $k = 0.4$. The universal stability functions measured by Garratt and others depend on two dimensionless constants, noted as β_1 and γ_2 in this work. They are taken to be the values given by Garratt, $\beta_1 = 5$ and $\gamma_2 = 16$.

APPENDIX D

TROPOSPHERIC PRESSURE PROFILE

Following Chapter 2.4 of [133], a mass of air in the troposphere under hydrostatic equilibrium obeys the differential equation $P'(z) + \frac{g}{RT(z)}P(z) = 0$ where $P(z)$ represents the pressure at height z, g is the gravitational acceleration constant near the Earth surface, R is the specific gas constant of air (the ratio of the universal gas constant to the average molar mass of air), and $T(z)$ is the temperature at height z. This expresses that if there are no net forces acting on the air (the definition of hydrostatic equilibrium), that the downward force of gravity on the mass of air must be equal to any net upward pressure-differential force on it. If the temperature in the troposphere linearly decreases in height with lapse rate L, then $T(z) = T_0 - Lz$ and the equation is separable and integrable:

$$\int_0^z \frac{P'(\xi)}{P(\xi)}d\xi = -\frac{g}{R}\int_0^z \frac{1}{T_0 - L\xi}d\xi \qquad \Rightarrow \qquad \ln\left(\frac{P(z)}{P(0)}\right) = \frac{g}{RL}\ln\left(1 - \frac{Lz}{T_0}\right)$$

$$P(z) = P_0\left(1 - \frac{Lz}{T_0}\right)^{g/(RL)} \tag{72}$$

Which is an exponential-like function in height, depending on the parameters. In particular, it can be seen for a small lapse rate, $\lim_{L\to 0} P(z) = P_0 e^{-gz/(RT_0)}$.

REFERENCES

[1] Harvey Lehpamer, *Microwave transmission networks: planning, design, and deployment*. McGraw-Hill Professional, first ed., 2004.

[2] J. Burrell, T. Brooke, and R. Beckwith, "Vineyard computing: sensor networks in agricultural production," *IEEE Pervasive Computing*, vol. 3, no. 1, pp. 38–45, 2004.

[3] L. Bencini, F. Chiti, G. Collodi, D. Di Palma, R. Fantacci, A. Manes, and G. Manes, "Agricultural monitoring based on wireless sensor network technology: Real long life deployments for physiology and pathogens control," in *Proc. Third Int. Conf. Sensor Technologies and Applications SENSORCOMM '09*, pp. 372–377, 2009.

[4] P. Marino, F. P. Fontan, M. A. Dominguez, and S. Otero, "Deployment and implementation of an agricultural sensor network," in *Proc. Second Int. Conf. Sensor Technologies and Applications SENSORCOMM '08*, pp. 264–269, 2008.

[5] M. Maskery and V. Krishnamurthy, "Decentralized activation in a zigbee-enabled unattended ground sensor network: A correlated equilibrium game theoretic analysis," in *Communications, 2007. ICC '07. IEEE International Conference on*, pp. 3915–3920, June 2007.

[6] V. Krishnamurthy, M. Maskery, and G. Yin, "Decentralized adaptive filtering algorithms for sensor activation in an unattended ground sensor network," *Signal Processing, IEEE Transactions on*, vol. 56, pp. 6086–6101, Dec. 2008.

[7] R. Belmonte, S. Fast, and J. Schuster, "A comparison of near earth propagation over layered media," in *Proc. IEEE Military Communications Conf. MILCOM 2008*, pp. 1–6, 2008.

[8] Gang Liu, J. Hoppe, R. Shahidain, and H. Tsai, "Evaluating the impact of wave polarization on improvised explosive device (IED) jamming," in *Wireless Information Technology and Systems (ICWITS), 2010 IEEE International Conference on*, pp. 1–4, Sept. 2010.

[9] T. K. Hamrita, E. W. Tollner, and R. L. Schafer, "Toward fulfilling the robotic farming vision: advances in sensors and controllers for agricultural applications," *IEEE Transactions on Industry Applications*, vol. 36, no. 4, pp. 1026–1032, 2000.

[10] C. R. Anderson. Private Communication, 2010.

[11] S. P. Mason, "Atmospheric effects on radio frequency (RF) wave propagation in a humid, near-surface environment," Master's thesis, Naval Postgraduate School, Monterey, California, March 2010.

[12] R. Wert. Private Communication, 2010.

[13] D. Hughes, "Professor D.E. Hughes's researches in wireless telegraphy," *The Electrician*, vol. 43, pp. 40–41, May 1899.

[14] H. Hertz, *Electrical Waves: Being Researches on the Propagation of Electric Action with Finite Velocity through Space*. New York: Dover Publications Inc., 1962.

[15] J. Zenneck, "Über die fortpflanzung ebener elektromagnetischer wellen längs einer ebenen leiterfläche und ihre beziehung zur drahtlosen telegraphie," *Annalen der Physik*, vol. 328, no. 10, pp. 846–866, 1907.

[16] A. Sommerfeld, "Über die ausbreitung der wellen in der drahtlosen telegraphie," *Annalen der Physik*, vol. 333, no. 4, pp. 665–736, 1909.

[17] J. A. Stratton and H. Chinn, "The radiation characteristics of a vertical half-wave antenna," *Radio Engineers, Proceedings of the Institute of*, vol. 20, no. 12, pp. 1892–1913, 1932.

[18] K. Norton, "The propagation of radio waves over the surface of the earth and in the upper atmosphere," *Radio Engineers, Proceedings of the Institute of*, vol. 24, no. 10, pp. 1367–1387, 1936.

[19] K. Norton, "The physical reality of space and surface waves in the radiation field of radio antennas," *Proceedings of the Institute of Radio Engineers*, vol. 25, pp. 1192–1202, Sept. 1937.

[20] W. H. Wise, "The physical reality of Zenneck's surface wave," *Bell System Technical Journal*, vol. 16, no. 1, pp. 35–44, 1937.

[21] H. Bremmer, "The surface-wave concept in connection with propagation trajectories associated with Sommerfeld problem," *Antennas and Propagation, IRE Transactions on*, vol. 7, no. 5, pp. 175–182, 1959.

[22] Y. Rahmat-Samii, P. Parhami, and R. Mittra, "Loaded horizontal antenna over an imperfect ground," *Antennas and Propagation, IEEE Transactions on*, vol. 26, no. 6, pp. 789–796, 1978.

[23] K. Michalski, C. Smith, and C. M. Butler, "Analysis of a horizontal two-element antenna array above a dielectric halfspace," *Microwaves, Antennas and Propagation, IEE Proceedings H*, vol. 132, no. 5, pp. 335–338, 1985.

[24] D. A. Hill and J. R. Wait, "Excitation of the Zenneck surface wave by a vertical aperture," *Radio Science*, vol. 13, no. 6, pp. 969–977, 1978.

[25] G. Tyras, *Radiation and Propagation of Electromagnetic Waves*. Electrical Science, New York: Academic Press, 1969.

[26] G. Baumgartner, H. Hitney, and R. Pappert, "Duct propagation modelling for the integrated-refractive-effects prediction system (IREPS)," *Communications, Radar and Signal Processing, IEE Proceedings F*, vol. 130, no. 7, pp. 630–642, 1983.

[27] Michael B. Porter and Yong-Chun Liu, *Theoretical and Computational Ocean Acoustics*, vol. 2, pp. 947–956. World Scientific Publishing Co., 1994.

[28] B. D. Dushaw and J. A. Colosi, "Ray tracing for ocean acoustic tomography," Tech. Memo APL-UW TM 3-98, Applied Physics Laboratory, 1013 NE 40th Street Seattle, Washington, December 1998.

[29] J. Burbank, W. Kasch, and J. Ward, *Modeling and Simulation for RF Propagation*, pp. 20–50. John Wiley & Sons, Inc., 2011.

[30] M. A. Leontovich, "A new method to solve problems of em wave propagation over the earth surface," *USSR Academy of Sciences Transactions*, vol. 8, no. 1, pp. 16–22, 1944.

[31] M. A. Leontovich and V. A. Fock, "Solution of the problem of propagation of electromagnetic waves along the earth's surface by the method of parabolic equation," *Journal of Experimental and Theoretical Physics*, vol. 16, no. 1, pp. 557–573, 1946.

[32] R. H. Hardin and F. D. Tappert, "Applications of the split-step Fourier method to the numerical solution of nonlinear and variable coefficient wave equations," *SIAM Review*, vol. 15, p. 423, April 1973.

[33] F. D. Tappert, "Numerical solutions of a canonical nonlinear dispersive wave equation," *SIAM Review*, vol. 16, p. 140, January 1974.

[34] G. Apaydin, O. Ozgun, M. Kuzuoglu, and L. Sevgi, "A novel two-way finite-element parabolic equation groundwave propagation tool: Tests with canonical structures and calibration," *Geoscience and Remote Sensing, IEEE Transactions on*, vol. 49, pp. 2887–2899, Aug. 2011.

[35] O. Ozgun, "Recursive two-way parabolic equation approach for modeling terrain effects in tropospheric propagation," *Antennas and Propagation, IEEE Transactions on*, vol. 57, pp. 2706–2714, Sept. 2009.

[36] G. Dockery, R. Awadallah, D. Freund, J. Gehman, and M. Newkirk, "An overview of recent advances for the TEMPER Radar propagation model," in *Radar Conference, 2007 IEEE*, pp. 896–905, Apr. 2007.

[37] R. Akbarpour and A. R. Webster, "Ray-tracing and parabolic equation methods in the modeling of a tropospheric microwave link," *Antennas and Propagation, IEEE Transactions on*, vol. 53, no. 11, pp. 3785–3791, 2005.

[38] V. Fabbro, N. Guillet, and P. F. Combes, "Innovative improvements of the parabolic wave equation method for radiowave propagation modeling," in *Proc. Antennas and Propagation Twelfth Int. Conf. (Conf. Publ. No. 491)*, vol. 2, pp. 654–656, 2003.

[39] J. R. Kuttler and R. Janaswamy, "Improved Fourier transform methods for solving the parabolic wave equation," *Radio Science*, vol. 37, Mar. 2002.

[40] D. Donohue and J. Kuttler, "Propagation modeling over terrain using the parabolic wave equation," *Antennas and Propagation, IEEE Transactions on*, vol. 48, pp. 260–277, Feb. 2000.

[41] Mireille Levy, *Parabolic Equation Methods for Electromagnetic Wave Propagation*, vol. 45 of *IEE Electromagnetic Wave Series*. London: The Institution of Electrical Engineers, 2000.

[42] R. Luebbers, J. Schuster, and K. Wu, "Full wave propagation model based on moving window FDTD," in *Military Communications Conference, 2003. MILCOM '03. 2003 IEEE*, vol. 2, pp. 1397–1401Vol.2, 2003.

[43] K. Wu, J. Schuster, R. Ohs, and R. Luebbers, "Application of moving window FDTD to modeling the effects of atmospheric variations and foliage on radio wave propagation over terrain," in *Military Communications Conference, 2004. MILCOM 2004. 2004 IEEE*, vol. 3, pp. 1515–1521Vol. 3, 2004.

[44] K. Wu, J. Schuster, and R. Luebbers, "Full wave modeling of RF propagation between low-to-the-ground antennas," in *Antennas and Propagation Society International Symposium, 2005 IEEE*, vol. 2B, pp. 711–714, 2005.

[45] R. R. Ohs, J. W. Schuster, and T. Y. Fung, "Full wave simulation of radiowave propagation in unattended ground sensor networks," in *Proc. IEEE Radio and Wireless Symp. RWS '09*, pp. 183–186, 2009.

[46] H. Friis, "A note on a simple transmission formula," *Proceedings of the IRE*, vol. 34, no. 5, pp. 254–256, 1946.

[47] T. Rappaport, *Wireless Communications: Principles and Practice*. Upper Saddle River, NJ, USA: Prentice Hall PTR, 2nd ed., 2001.

[48] A. De, T. Sarkar, and M. Salazar Palma, "Characterization of the far-field environment of antennas located over a ground plane and implications for cellular communication systems," *Antennas and Propagation Magazine, IEEE*, vol. 52, pp. 19–40, Dec. 2010.

[49] J. Andrusenko, R. Miller, J. Abrahamson, N. Merheb Emanuelli, R. Pattay, and R. Shuford, "VHF general urban path loss model for short range ground-to-ground communications," *Antennas and Propagation, IEEE Transactions on*, vol. 56, no. 10, pp. 3302–3310, 2008.

[50] F. Comeau, S. Sivakumar, W. J. Phillips, and W. Robertson, "A clustered wireless sensor network model based on log-distance path loss," in *Communication Networks and Services Research Conference, 2008. CNSR 2008. 6th Annual*, pp. 366–372, 2008.

[51] H. Liu, Z. Meng, and Y. Shang, "Sensor nodes placement for farmland environmental monitoring applications," in *Wireless Communications, Networking and Mobile Computing, 2009. WiCom '09. 5th International Conference on*, pp. 1–4, 2009.

[52] Q. Wu, D. Matolak, and R. Apaza, "Airport surface area propagation path loss in the VHF band," in *Integrated Communications, Navigation and Surveilance Conference (ICNS), 2011*, pp. B4–1–B4–6, 2011.

[53] J. Itkonen, B. Tuzson, and J. Lempiainen, "A novel network layout for CDMA cellular networks with optimal base station antenna height and downtilt," in *Vehicular Technology Conference, 2006. VTC 2006-Spring. IEEE 63rd*, vol. 2, pp. 688–692, may 2006.

[54] ITU, "Method for point-to-area predictions for terrestrial services in the frequency range 30 MHz to 3000 MHz," Recommendation P.1546, International Telecommunication Union, 2009.

[55] E. Silva and G. Carrijo, "A vectorial analysis of the two-ray model," in *Communications Systems, 2004. ICCS 2004. The Ninth International Conference on*, pp. 607–611, Sept. 2004.

[56] DaHan Liao and K. Sarabandi, "On the effective low-grazing reflection coefficient of random terrain roughness for modeling near-earth radiowave propagation," *Antennas and Propagation, IEEE Transactions on*, vol. 58, no. 4, pp. 1315–1324, 2010.

[57] D. Liao and K. Sarabandi, "An approximate numerical model for simulation of long-distance near-ground radiowave propagation over random terrain profiles," in *Proc. IEEE Military Communications Conf. MILCOM 2007*, pp. 1–7, 2007.

[58] Wenjie Xu, S. Zekavat, and Hui Tong, "A novel spatially correlated multiuser MIMO channel modeling: Impact of surface roughness," *Antennas and Propagation, IEEE Transactions on*, vol. 57, pp. 2429–2438, Aug. 2009.

[59] A. G. Yarovoy, C. N. Vazouras, J. G. Fikioris, and L. P. Ligthart, "Numerical simulations of the scattered field near a statistically rough air-ground interface," *Antennas and Propagation, IEEE Transactions on*, vol. 52, no. 3, pp. 780–789, 2004.

[60] DaHan Liao and K. Sarabandi, "Terminal-to-terminal hybrid full-wave simulation of low-profile, electrically-small, near-ground antennas," *Antennas and Propagation, IEEE Transactions on*, vol. 56, pp. 806–814, Nov. 2008.

[61] D. Liao and K. Sarabandi, "Optimization of low-profile antennas for applications in unattended ground sensor networks," in *Proc. IEEE Antennas and Propagation Society Int. Symp. 2006*, pp. 783–786, 2006.

[62] B. D. Popovic and D. Z. Djurdjevic, "Entire-domain analysis of thin-wire antennas near or in lossy ground," *IEE Proceedings Microwaves, Antennas and Propagation*, vol. 142, no. 3, pp. 213–219, 1995.

[63] A. Hugine, H. I. Volos, J. Gaeddert, and R. M. Buehrer, "Measurement and characterization of the near-ground indoor ultra wideband channel," in *Proc. IEEE Wireless Communications and Networking Conf. WCNC 2006*, vol. 2, pp. 1062–1067, 2006.

[64] R. A. Foran, T. B. Welch, and M. J. Walker, "Very near ground radio frequency propagation measurements and analysis for military applications," in *Proc. IEEE Military Communications MILCOM 1999*, vol. 1, pp. 336–340, Oct. 31–Nov. 3, 1999.

[65] R. Bhattacharjea, "Proposal: The effects of atmospheric refractivity in near-earth UHF channels," August 2012.

[66] G. Durgin, *Space-Time Wireless Channels*. Upper Saddle River, NJ, USA: Prentice Hall Press, 2002.

[67] L. Greenstein, S. Ghassemzadeh, V. Erceg, and D. Michelson, "Ricean k-factors in narrow-band fixed wireless channels: Theory, experiments, and statistical models," *Vehicular Technology, IEEE Transactions on*, vol. 58, pp. 4000–4012, Oct. 2009.

[68] G. G. Joshi, C. B. Dietrich, C. R. Anderson, W. G. Newhall, W. A. Davis, J. Isaacs, and G. Barnett, "Near-ground channel measurements over line-of-sight and forested paths," *IEE Proceedings Microwaves, Antennas and Propagation*, pp. 589–596, 2005.

[69] M. H. Hashim and S. Stavrou, "Measurements and modelling of wind influence on radiowave propagation through vegetation," *IEEE Transactions on Wireless Communications*, vol. 5, no. 5, pp. 1055–1064, 2006.

[70] E. R. Pelet, J. E. Salt, and G. Wells, "Effect of wind on foliage obstructed line-of-sight channel at 2.5 GHz," *IEEE Transactions on Broadcasting*, vol. 50, no. 3, pp. 224–232, 2004.

[71] E. Smith and S. Weintraub, "The constants in the equation for atmospheric refractive index at radio frequencies," *Proceedings of the IRE*, vol. 41, pp. 1035–1037, Aug. 1953.

[72] B. Bean and R. McGavin, "The turbulent characteristics of the radio refractive index near the ground," in *Proc. Antennas and Propagation Society Int. Symp*, vol. 1, pp. 62–64, 1963.

[73] N. E. Rider, "Eddy diffusion of momentum, water vapour, and heat near the ground," *Philosophical Transactions of the Royal Society of London. Series A, Mathematical and Physical Sciences*, vol. 246, no. 918, pp. 481–501, 1954.

[74] K. Anderson, "Radar measurements at 16.5 GHz in the oceanic evaporation duct," *Antennas and Propagation, IEEE Transactions on*, vol. 37, pp. 100–106, Jan. 1989.

[75] Jiao Lin and Zhang Yong Gang, "The effects of radar detection in heterogeneous evaporation duct conditions," in *Antennas, Propagation and EM Theory, 2008. ISAPE 2008. 8th International Symposium on*, pp. 1402–1405, Nov. 2008.

[76] I. Levadnyi, V. Ivanov, and V. Shalyapin, "Assessment of evaporation duct propagation simulation," in *General Assembly and Scientific Symposium, 2011 XXXth URSI*, pp. 1–4, Aug. 2011.

[77] ISO, "ISO 2533:1975."

[78] G. Gyatt, "The standard atmosphere," Mar. 2011.

[79] B. Bean and E. Dutton, *Radio Meteorology*. New York: Dover, 1968.

[80] H. Hitney, J. Richter, R. Pappert, K. Anderson, and G. Baumgartner, Jr., "Tropospheric radio propagation assessment," *Proceedings of the IEEE*, vol. 73, pp. 265–283, Feb. 1985.

[81] G. Bye and R. Howell, "Average radio refractive index lapse rate of the lower troposphere for locations in NW Europe," in *Antennas and Propagation, 1989. ICAP 89., Sixth International Conference on (Conf. Publ. No.301)*, pp. 229–233vol.2, Apr. 1989.

[82] W. L. Patterson, "Advanced refractive effects prediction system (AREPS) version 1.0 user's manual," Technical Document 3028, SPAWAR Systems Center San Diego, Space and Naval Warfare Systems Center San Diego, CA 92152-5001, April 1998.

[83] F. J. Ryan, "Analysis of electromagnetic propagation over variable terrain using the parabolic wave equation," Tech. Rep. 1453, Naval Ocean Systems Center, San Diego, California, October 1991.

[84] J. B. Keller, "Geometrical theory of diffraction," *Journal of the Optical Society of America*, vol. 52, pp. 116–130, Feb 1962.

[85] R. Kouyoumjian and P. Pathak, "A uniform geometrical theory of diffraction for an edge in a perfectly conducting surface," *Proceedings of the IEEE*, vol. 62, pp. 1448–1461, Nov 1974.

[86] Finn B. Jensen, William A. Kuperman, Michael B. Porter, and Henrik Schmidt, *Computational Ocean Acoustics*. Modern Acoustics Signal Processing, New York: Springer, 2 ed., 2011.

[87] Henrik Schmidt, "SAFARI: Seismo-acoustic fast field algorithm for range independent environments. User's guide.," Report SR 113, SACLANT ASW Research Centre, La Spezia, Italy, 1987.

[88] H. Schmidt, *OASES, Version 3.1: User Guide and Reference Manual*. Department of Ocean Engineering, Massachusetts Institute of Technology, October 2004.

[89] R. Bhattacharjea, G. D. Durgin, and C. R. Anderson, "A direct spectral domain method for near-ground microwave radiation by a vertical dipole above earth in the presence of atmospheric refractivity," in *PIERS Proceedings*, 2013.

[90] K. Michalski, "Extrapolation methods for Sommerfeld integral tails," *Antennas and Propagation, IEEE Transactions on*, vol. 46, no. 10, pp. 1405–1418, 1998.

[91] B. Hu and W. C. Chew, "Fast inhomogeneous plane wave algorithm for electromagnetic solutions in layered medium structures: Two-dimensional case," *Radio Science*, vol. 35, no. 1, pp. 31–43, 2000.

[92] S. Ebihara and W. C. Chew, "Calculation of Sommerfeld integrals for modeling vertical dipole array antenna for borehole radar," *IEICE Transactions On Electronics*, vol. E86-C, no. 10, pp. 2085–2096, 2003.

[93] S. Mahmoud, "Image theory for electric dipoles above a conducting anisotropic earth," *Antennas and Propagation, IEEE Transactions on*, vol. 32, pp. 679–683, Jul 1984.

[94] D. Fang, J. Yang, and G. Delisle, "Discrete image theory for horizontal electric dipoles in a multilayered medium," *Microwaves, Antennas and Propagation, IEE Proceedings H*, vol. 135, pp. 297–303, Oct 1988.

[95] M. Aksun and G. Dural, "Clarification of issues on the closed-form Green's functions in stratified media," *Antennas and Propagation, IEEE Transactions on*, vol. 53, no. 11, pp. 3644–3653, 2005.

[96] M. Yuan and T. Sarkar, "Computation of the Sommerfeld integral tails using the matrix pencil method," *Antennas and Propagation, IEEE Transactions on*, vol. 54, pp. 1358–1362, April 2006.

[97] M. Yuan, T. Sarkar, and M. Salazar-Palma, "A direct discrete complex image method from the closed-form Green's functions in multilayered media," *Microwave Theory and Techniques, IEEE Transactions on*, vol. 54, no. 3, pp. 1025–1032, 2006.

[98] V. Okhmatovski and A. Cangellaris, "A new technique for the derivation of closed-form electromagnetic Green's functions for unbounded planar layered media," *Antennas and Propagation, IEEE Transactions on*, vol. 50, pp. 1005–1016, Jul 2002.

[99] V. Okhmatovski and A. Cangellaris, "Evaluation of layered media Green's functions via rational function fitting," *Microwave and Wireless Components Letters, IEEE*, vol. 14, pp. 22–24, Jan 2004.

[100] J. Mosig, "The weighted averages algorithm revisited," *Antennas and Propagation, IEEE Transactions on*, vol. 60, pp. 2011–2018, April 2012.

[101] K. A. Michalski and D. Zheng, "Modeling antennas and scatterers of arbitrary shape embedded in layered dielectric media," Tech. Rep. ADA214902, Texas A&M University, Nov. 1989.

[102] D. G. Fang, *Antenna Theory and Microstrip Antennas*. Boca Raton: CRC Press, 2010.

[103] A. Sommerfeld, *Partial Differential Equations in Physics*. New York: Academic Press, 1949.

[104] C.-T. Tai, *Dyadic Green Functions in Electromagnetic Theory*. IEEE Series on Electromagnetic Waves, IEEE Press, second ed., 1996.

[105] M. Paulus, P. Gay-Balmaz, and O. J. F. Martin, "Accurate and efficient computation of the Green's tensor for stratified media," *Phys. Rev. E*, vol. 62, pp. 5797–5807, Oct 2000.

[106] M. Paulus and O. J. F. Martin, "Light propagation and scattering in stratified media: a Green's tensor approach," *J. Opt. Soc. Am. A*, vol. 18, pp. 854–861, Apr 2001.

[107] E. Anderson, Z. Bai, C. Bischof, S. Blackford, J. Demmel, J. Dongarra, J. Du Croz, A. Greenbaum, S. Hammarling, A. McKenney, and D. Sorensen, *LAPACK Users' Guide*. Philadelphia, PA: Society for Industrial and Applied Mathematics, third ed., 1999.

[108] H. Schmidt and F. Jensen, "A full wave solution for propagation in multilayered viscoelastic media with application to gaussian beam reflection at fluidsolid interfaces," *Journal of the Acoustical Society of America*, vol. 77, no. 3, pp. 813–825, 1985.

[109] F. Ling and J.-M. Jin, "Discrete complex image method for Green's functions of general multilayer media," *Microwave and Guided Wave Letters, IEEE*, vol. 10, no. 10, pp. 400–402, 2000.

[110] A. Wyatt, "QUADVGK: Vectorised adaptive G7,K15 Gaussian quadrature on vector of integrals," Feb. 2008. `http://www.mathworks.com/matlabcentral/fileexchange/18801-quadvgk/content/quadvgk.m`.

[111] L. F. Shampine, "Vectorized adaptive quadrature in MATLAB," *J. Comput. Appl. Math.*, vol. 211, pp. 131–140, Jan. 2008.

[112] A. Iserles and S. Nørsett, "On quadrature methods for highly oscillatory integrals and their implementation," *BIT Numerical Mathematics*, vol. 44, no. 4, pp. 755–772, 2004.

[113] A. Iserles, S. Nørsett, and S. Olver, "Highly oscillatory quadrature: The story so far," in *Numerical Mathematics and Advanced Applications* (A. B. de Castro, D. Gómez, P. Quintela, and P. Salgado, eds.), pp. 97–118, Springer Berlin Heidelberg, 2006.

[114] V. Domínguez, I. G. Graham, and V. P. Smyshlyaev, "Stability and error estimates for Filon-Clenshaw-Curtis rules for highly oscillatory integrals," *IMA Journal of Numerical Analysis*, vol. 31, no. 4, pp. 1253–1280, 2011.

[115] V. Domínguez, I. Graham, and T. Kim, "Filon-Clenshaw-Curtis rules for highly-oscillatory integrals with algebraic singularities and stationary points," *SIAM Journal of Numerical Analysis*, vol. 51, no. 3, pp. 1542–1566, 2013.

[116] L. N. Trefethen *et al.*, *Chebfun Version 4.2*. The Chebfun Development Team, 2011. `http://www.chebfun.org/`.

[117] Z. H. Firouzeh, G. A. E. Vandenbosch, R. Moini, S. H. H. Sadeghi, and R. Faraji-Dana, "Efficient evaluation of Green's functions for lossy half-space problems," *Progress In Electromagnetics Research*, vol. 109, pp. 139–157, 2010.

[118] U. Leonhardt and T. G. Philbin, "Transformation optics and the geometry of light," in *Progress in Optics* (E. Wolf, ed.), vol. 53 of *Progress in Optics*, ch. 2, pp. 69 – 152, Elsevier, 2009.

[119] J. R. Garratt, *The Atmospheric Boundary Layer*. Cambridge atmospheric and space science series, Cambridge University Press, 1992.

[120] O. Reynolds, "On the dynamical theory of incompressible viscous fluids and the determination of the criterion," *Philosophical Transactions of the Royal Society of London. A*, vol. 186, pp. pp. 123–164, 1895.

[121] T. Yokoi, "Measurements of the air temperature profile near the ground by two laser beams," *Journal of Atmospheric and Oceanic Technology*, vol. 3, pp. 559–563, September 1986.

[122] A. R. Von Hippel, ed., *Dielectric materials and applications*. New York: Technology Press of M.I.T. and Wiley, 1954.

[123] D. J. Mildrexler, M. Zhao, and S. W. Running, "Satellite finds highest land skin temperatures on earth," *Bull. Amer. Meteor. Soc.*, vol. 92, pp. 855–860, Feb. 2011.

[124] M. New, M. Hulme, and P. Jones, "Representing twentieth-century space-time climate variability. Part I: Development of a 1961–90 mean monthly terrestrial climatology," *Journal of Climate*, vol. 12, pp. 829–856, March 1999.

[125] P. Hoekstra and A. Delaney, "Dielectric properties of soils at UHF and microwave frequencies," *Journal of Geophysical Research*, vol. 79, no. 11, pp. 1699–1708, 1974.

[126] J. M. H. Hendrickx, R. L. V. Dam, B. Borchers, J. Curtis, H. A. Lensen, and R. Harmon, "Worldwide distribution of soil dielectric and thermal properties," in *in Detection and Remediation Technologies for Mines and Minelike Targets VIII*, 2003.

[127] O. P. N. Calla, M. C. Borah, P. Vashishtha, R. Mishra, A. Bhattacharya, and S. P. Purohit, "Study of the properties of dry and wet loamy soil at microwave frequencies," *The Indian Journal of Radio & Space Physics*, vol. 28, pp. 109–112, June 1999.

[128] N. Wagner and A. Scheuermann, "On the relationship between matric potential and dielectric properties of organic free soils: a sensitivity study," *Canadian Geotechnical Journal*, vol. 46, no. 10, pp. 1202–1215, 2009.

[129] J. O. Curtis, "Electromagnetic power attenuation in soils," Tech. Rep. ERDC/EL TR-05-5, Engineer Research and Development Center, Aug 2005.

[130] Federal Communications Commission, "Millimeter wave propagation: Spectrum management implications," Bulletin 70, Federal Communications Commission, Office of Engineering and Technology, New Technology Development Division, Mail Stop Code 1300-E Washington, DC 20554, July 1997.

[131] ITU, "Radio regulations," 2012.

[132] T. Kaifas, "Direct rational function fitting method for accurate evaluation of sommerfeld integrals in stratified media," *Antennas and Propagation, IEEE Transactions on*, vol. 60, no. 1, pp. 282–291, 2012.

[133] Daniel J. Jacob, *Introduction to Atmospheric Chemistry*. Princeton University Press, 1999.